Measurement of the Neutron Cross Section on Argon between 100 and 800 MeV

A Dissertation Presented

by

Sergey Martynenko

to

The Graduate School

in Partial Fulfillment of the Requirements

for the Degree of

Doctor of Philosophy

in

Physics

Stony Brook University

January 2021

Stony Brook University

The Graduate School

Sergey Martynenko

We, the dissertation committee for the above candidate for the Doctor of Philosophy degree, hereby recommend acceptance of this dissertation.

Clark McGrew – Dissertation Advisor
Professor, Department of Physics and Astronomy

Dmitri Kharzeev – Chairperson of Defense
Professor, Department of Physics and Astronomy

Eden Figueroa
Professor, Department of Physics and Astronomy

Steven Kettell
Group leader of Brookhaven's Electronic Detector Group
Brookhaven National Lab

This dissertation is accepted by the Graduate School.

Eric Wertheimer
Dean of the Graduate School

Abstract of the Dissertation

Measurement of the Neutron Cross Section on Argon between 100 and 800 MeV

by

Sergey Martynenko

Doctor of Philosophy

in

Physics

Stony Brook University

2021

The CAPTAIN (Cryogenic Apparatus for Precision Tests of Argon Interactions with Neutrinos) experiment's goal is to measure the neutron cross section and define the neutron signature in liquid argon in the 100 MeV to 800 MeV energy range. This measurement can significantly improve uncertainty in neutrino energy reconstruction introduced by neutrons. They take away a portion of energy with low possibility to reconstruct it due to lack of charge. In particular, data provided by the CAPTAIN collaboration will serve the needs of the planned experiment DUNE (Deep Underground Neutrino Experiment), which will be a neutrino oscillation experiment using a Liquid Argon detector.

This thesis presents the first measurement of the neutron cross section on argon in the energy range of 100–800 MeV. The measurement is obtained using the data from a 4.3 h exposure of the Mini-CAPTAIN detector to the WNR/LANSCE beam at LANL. The measured cross section is presented in two forms.

First, the total cross section is measured from the attenuation coefficient of the neutron flux as it traverses the liquid argon volume. The method utilizes only the downstream part of the detector with a set of 2631 candidate interactions divided in bins of the neutron kinetic energy calculated from time-of-flight measurements. The energy averaged cross section is $0.91 \pm 0.10(\text{stat}) \pm 0.09(\text{syst})$ b.

Second, the extended measurement doubles the fiducial volume of the detector and improves the statistics by the factor of 2.4. New measurement is performed using a fit based on attenuation of the neutron flux. The new approach utilizes time-of-flight bins instead of energy bins. The final cross sections are given for flux averaged energies in considered time-of-flight bins: $\sigma_{146} = 0.601^{+0.140}_{-0.143} \pm 0.084(syst)$ b, $\sigma_{236} = 0.722^{+0.103}_{-0.101} \pm 0.036(syst)$ b, $\sigma_{319} = 0.804^{+0.129}_{-0.121} \pm 0.040(syst)$ b, $\sigma_{404} = 0.739^{+0.135}_{-0.091} \pm 0.037(syst)$ b, $\sigma_{543} = 0.741^{+0.088}_{-0.088} \pm 0.037(syst)$ b.

Contents

List of Figures **vii**

List of Tables **xiii**

Acknowledgements **xv**

1 Introduction **1**

2 Neutrino physics **3**
2.1 Standard model 3
2.2 Neutrino oscillations 4
2.2.1 Neutrino Oscillation theory 5
2.2.2 Neutrino Oscillation measurements 8
2.2.3 Neutrino interactions 10
2.2.4 Liquid Argon and Neutrons 11
2.3 Neutron Cross Section Definition 15

3 CAPTAIN experimental setup **17**
3.1 MiniCAPTAIN detector 17
3.1.1 TPC design 17
3.1.2 PDS design 22
3.2 Neutron beam 24
3.3 Detector triggering and Analysis data set 25

4 Reconstruction **28**
4.1 Calibration and "raw" hit finding 28
4.2 TPC Reconstruction 30
4.2.1 Noise cleaning 30
4.2.2 Hit transfer 32
4.2.3 Clustering 33
4.2.4 Path follow 34

4.2.5 Track reconstruction 36
4.3 PDS reconstruction 41
4.3.1 Hit finding 41
4.3.2 Digitizer alignment 44
4.3.3 Coincidence finding 46
4.3.4 Neutron energy measurement 46
4.3.5 PDS-TPC alignment 48

5 Data Study **49**
5.1 Beam Spot Study 49
5.2 Electron Life Time 55
5.3 Wire efficiency and collected charge 55

6 Monte Carlo(MC) simulation **62**
6.1 Simulation description 62
6.2 Collected Charge Study 63
6.3 Wire Efficiency MC/Data 64
6.3.1 Track Length study MC/DATA 67
6.3.2 Track Gap study MC/DATA 68

7 Neutron Cross Section Measurement **72**
7.1 Measurement Method 72
7.2 Selection topology 75
7.3 Neutron cross section 76
7.4 Systematic effects 77

8 Extended Neutron Cross Section Measurement **82**
8.1 Fit data structure 82
8.2 Fitting function and algorithms 84
8.3 Asimov sample studies 90
8.4 Neutron data fit 93

9 Summary **101**

List of Figures

2.1 Fundamental particles of the Standard Model: three generations of quarks and leptons, and force-carrier gauge bosons.[13] 4
2.2 Electron neutrino survival probability($P_{\nu_e \to \nu_e}$) as a function of E_ν. Data points are the results of Borexino , SNO, and SuperKamiokande experiment. Blue and red curves are theoretical prediction for different values of Δm^2_{21}[23]. 7
2.3 Muon neutrino survival probability($P_{\nu_\mu \to \nu_\mu}$) as a function of L/E_ν. Data points are the result of SuperKamiokande experiment. Blue curve - theoretical prediction[26]. 9
2.4 Electron anti-neutrino survival probability($P_{\bar{\nu_e} \to \bar{\nu_e}}$) as a function of L/E_ν. Data points are the results of KamLAND experiment. Blue curve - theoretical prediction[21]. 9
2.5 Neutrino(a) and antineutrino(b) cross sections as a fiction of energy with overlaid data up to 2012. Solid line represents theoretical prediction for total cross section and dashed lines represent quasi-elastic scattering(QE), resonant production(RES), and deep inelastic scattering(DIS) cross sections[42]. 11
2.6 Feynman diagrams for main neutrino CC interaction modes. . . . 12
2.7 The illustration of the future DUNE setup proposed in [1] 12
2.8 Neutrino/Antineutrino beam spectrum, which will be used in DUNE experiment[2]. 13
2.9 The theoretical prediction of the probability of neutrino/antineutrino oscillations with normal mass hierarchy for 1300km flight path[2]. 14
2.10 Neutrino(a) and antineutrino(b) beams simulated using GENIE $v2\_12\_8$[44]. Blue - true neutrino/antineutrino energy spectrum. Red - "reconstructed" neutrino energies excluding neutrons. . . . 15
2.11 The energy carried away by neutrons in neutrino(red) and antineutrino(blue) interactions. The calculation is made by subtracting true neutrino/antineutrino energy and "reconstructed" neutrino energies excluding neutrons in each event. 16

2.12 Existing world data for neutron cross sections in liquid argon. Solid black line is experimental data. Colored lines are theoretical partial cross section calculations made by "ENDF"[6]. 16

3.1 The schematic of the miniCAPTAIN detector(a) and the photo of the detector(b) at its final assembling stage[46]. 18
3.2 The schematic drawing of the TPC part of the miniCAPTAIN detector[46]. 19
3.3 The schematic of the positions of the wires with respect to the beam in the miniCAPTAIN. The hexagonal plane of the TPC lays in the XY plane with zero coordinate in the middle of the cryostat. The Z-axis pierces the detector vertically with zero at the top of the cryostat. 20
3.4 The diagram of readout electronics in miniCAPTAIN TPC[46]. . . 21
3.5 The PMT configuration for the PDS system, and the system's response to a calibration LED mounted on the (a) right or (b) left side of the field cage (looking downward)[46]. 22
3.6 The diagrams of different beamlines provided at Target 4 LANSCE facility. The CAPTAIN experiment was positioned at 4FP15R (red square)[45]. 23
3.7 The neutron energy spectrum provided by LANL for the CAPTAIN experiment[51]. 24
3.8 Two beam setup provided by LANSCE. First, the standard beam structure at 4FP15R(a). Second, the CAPTAIN-specific beam structure(b). 26
3.9 Three argon purification system used in miniCAPTAIN detector: the inline filter(a), the gas recirculation system, and the liquid argon purification system designed by Criotec Impianti[46]. 27

4.1 The example of the signal from the induction wire plane as a function of frequency. The red curve represents the estimated smooth signal for the filter. 29
4.2 The example of the signal from the induction wire plane as a function of time. The dashed blue line represent the signal before the filtering and the black solid line is the final signal after the filtrating. 29
4.3 The example of the clear signal hit(a) and the noise hit(b) from collection wire(X-plane). Sample value on the Y-axis is measured in the number calibrated electrons arrived at given wire at a given time. 30

4.4 The criteria parameter values for all collection wire planes from the analysis data set. The red line show the cut for the parameter.(equation 4.1) 31
4.5 The example of the signal hit(a) and the noise hit(b) from one of induction wires(U-plane). Sample value on the Y-axis is measured in the number calibrated electrons arrived at a given wire at a given time. 32
4.6 Hough (r,θ) space filled with transformed XZ points. 33
4.7 V-plane hits that came out of the HitTransfer algorithm. The X axis represents wire number, the Y axis shows timing information(each sample = 500ns), and the Z axis represents charge for each hit. 35
4.8 Clustered hits for a V-plane event from Fig 4.7. Each cluster shows as different color. The X axis represents wire number, the Y axis shows timing information(each sample = 500ns.) 35
4.9 Found clusters before the Path Following algorithm was applied. Each cluster shows as a different color. The X axis represents wire number, the Y axis shows timing information(each sample = 500ns. 36
4.10 Found clusters after the Path Following algorithm. Each cluster shows as different color. The X axis represents wire number, the Y axis shows timing information(each sample = 500ns. 37
4.11 Clusters that are combined to be a track over all 3 wire planes. Each cluster combinations is shown as a different color. Black dots represent hits.The X axis represents wire number, the Y axis shows timing information(each sample = 500ns. 38
4.12 MC simulation of 600 MeV muon track starting in the middle of the detector(Yellow line). Blue lines represent clusters, reconstructed on each wire plane. Red dots are reconstructed Hits. 39
4.13 MC simulation of 600 MeV muon track starting in the middle of the detector(Yellow line). 3 Triangular Blue lines represent clusters, reconstructed on each wire plane. The 4th blue line in the middle is a 3D track reconstructed from combining 2D clusters. Red dots are reconstructed 3D hits. 40
4.14 The example of PDS event. Red dots represent found peaks, the dark green line is a starting time of the RF pulse, and the light green line is a starting time of the coincidence with the most charge in it. 41
4.15 The example of the difference between sample values of two consecutive samples for one PMT in arbitrary PDS event. 42
4.16 The example of finding hit parameters for two PDS hits close together. 43

4.17 The ratio between two consecutive gaps across three digitizers before alignment . . . 44
4.18 The ratio between two consecutive gaps across three digitizers before alignment(zoomed at aligned region) . . . 45
4.19 The difference between starting time of the RF puls of digitizer i and j, where i,j can be 0,1 or 2. . . . 46
4.20 Time of flight spectrum for all found coincidences in aligned PDS events. The Gaussian fit represents gamma peak. . . . 47

5.1 The starting Z position of all reconstructed tracks. The starting position is defined as one with maximum X coordinate. . . . 50
5.2 The Z position of a track. The red line is the original Z position, while the blue line is the Z position corrected using PDS information. Tracks below -300 mm correspond to neutrons from second and third micropulse that have no proper PDS correction. . . . 51
5.3 Starting XY position of the reconstructed tracks inside the beam time. The beam time is defined between -1000 and 0 on Figure 14. Transparent red line represent linear fit for the beam. . . . 52
5.4 Mean values(a) and sigma values(b) of Gaussian data peaks in Z for all five slices in X. . . . 54
5.5 Mean values(a) and sigma values(b) of Gaussian data peaks in Y for all five slices in X. . . . 54
5.6 The evolution of starting positions (Z coordinate) of reconstructed tracks. . . . 57
5.7 The evolution of starting positions (Y coordinates) of reconstructed tracks. . . . 58
5.8 On the left is the logarithm of the deposited charge vs time for selected long muon tracks(a,c,e). On the right are profiles of the electron lifetime plots(b,d,f). . . . 59
5.9 Inefficiency for each wire for all 3 wire planes based on an average charge of neighboring hits. Yellow color specter represent the most inefficient wires, while blue stands for efficient wires. . . . 60
5.10 Collected charge for each wire for all 3 wire planes. Blank regions represent wires either turned off during construction or eliminated as inefficient. . . . 61

6.1 The comparison between the simulated noise and noise observed in one of the neutron runs. The blue line is noise observed in the experiment, the red line is simulated noise. . . . 63
6.2 The collected charge for each wire for all 3 wire planes. Blank regions represent wires turned off to represent the data. . . . 65

6.3 Track length distribution for reconstructed Data and MC tracks from neutron interactions. 66
6.4 Number of X wires missing in reconstructed track for the Data (a) and MC (b) vs collection plane wire number. 68
6.5 Maximum number of wires missing per reconstructed track for the Data (a) and MC (b) vs collection plane wire number. 69
6.6 Efficiency for each wire for all 3 wire planes in 25mm region around the beam. The black dots represent data, and the Red line is MC efficiency. 70
6.7 On the left is the detector efficiency vs drift time for X, U, and V wire planes(a,c,e). On the right are residual plots comparing Data and MC efficiencies(b,d,f). 71

7.1 The neutron beam attenuation process. 73
7.2 The Reconstructed X coordinate of starting pistons of proton tracks vs its true values (MC simulation). 74
7.3 X-plane hits from the event that obeys all selection criteria in the analysis. The X axis represents wire number, Y axis shows timing information(each sample = 500ns), and Z axis represents charge for each hit. 75
7.4 Neutron cross section measurement as a function of neutron kinetic energy. Black dots are data points, Read and blue are values obtained from simulation. The simulation cross sections are obtained from exponential fits to the distribution of tracks as a function of depth into the detector. The errors bars correspond only to the statistical uncertainty of the fits, for both data and simulation[7]. 77
7.5 The exponential fit for starting position of reconstructed tracks from neutron interaction vs the depth in the detector. 80

8.1 Neutron time of flight measured with PDS for the entire CAPTAIN data set. 83
8.2 Neutron time of flight calculated based on MC simulation vs initial neutron energy. The red lines are chose TOF bins in the extended measurement. The black dashed lines are initial measurement Energy bins 84
8.3 The neutron energy distribution for each TOF bin according to MC simulation using neutron energy spectrum provided by LANSCE[51]. The flux weighted average energy for each bin is given in captions. 85
8.4 The general shape of the given χ^2 function near the minimum for all non-cross section parameters in the fit. 91

8.5 The Momentum change of the initial neutron in interactions considered for the cross section measurement. 93
8.6 The results of the Data/MC fit for all cross section parameters with variation of starting point of the fit. 97
8.7 Post-fit distribution of starting position of reconstructed tracks inside the signal region for each TOF bin. 98
8.8 Post-fit distribution of starting position of reconstructed tracks inside the side region for each TOF bin. 99
8.9 The comparison between the initial neutron cross section measurement and the extended measurement. The red points represent the initial neutron cross section measurement with statistical(lines) and systematic(hats) errors. The black dots represent extended cross section measurements for flux averaged energy in each of five considered time-of-flight bins. The extended measurement presented with with statistical(lines) and systematic(hats) errors. 100

List of Tables

2.1 Current values of oscillation parameters based on the results of the global fit. The data is taken from [41]. 10

5.1 The linear background fit for Z position distribution for five slices in X. The line form is: $y = \alpha \times x + \beta$. 52
5.2 The results of linear fits of mean values and sigmas of Gaussian data peaks in Z for all five slices in X. The line form is: $y = \alpha \times x + \beta$. 53
5.3 The linear background fit for Y position distribution for five slices in X. The line form is: $y = \alpha \times x + \beta$. 53
5.4 The results of linear fits of mean values and sigmas of Gaussian data peaks in Z for all five slices in X. The line form is: $y = \alpha \times x + \beta$. 53
5.5 Electron Life Time fit results 55

6.1 The comparison between mean collected charge and charge spread across the detector for reconstructed cosmic muons in Data and simulated 8GeV muons in MC. Values are given as a log of number of collected electrons. 64
6.2 The optimized values of the charge threshold and sigma for the simulation. The threshold is given in the number of electrons, and sigma is a percentage of the threshold. 66

7.1 Neutron cross section in bins of kinetic energy. The χ^2 per degrees of freedom is presented, as well as the total number of tracks used for the fit in each bin. The exact functional form used for the fits is $f(x) = c_1 e^{-c2x}$[7] 76
7.2 The cross section for single and multi-track events in selection region. The results are obtained from neutron simulation exponential hypothesis. 81
7.3 The cross section for single and multi-track events in selection region. The results are obtained from neutron simulation exponential hypothesis. 81

8.1 The neutron energy range and the flux weighted average energy for each TOF bin according to MC simulation using neutron energy spectrum provided by LANSCE[51] 86
8.2 Number of events in each TOF bin for the CAPTAIN low-intensity neutron data. 86
8.3 Cross section values used as a base values in the fit. Values obtained via thin target measurement for each TOF bin. 88
8.4 The result of the fit to "Asimov" data set with 4 times increased number of "Other" category events. Statistical uncertainties are taken from Hessian matrix. 92
8.5 The result of the fit to "Asimov" data set with the 4 times increase in the number of "Elastic" category events. Statistical uncertainties are taken from Hessian matrix. 94
8.6 The result of the fit to "Asimov" data set with ±5% variation of total number of events to accommodate to the predicted number of multi-track events in the experiment. Statistical uncertainties are taken from Hessian matrix. 94
8.7 The result of the fit to "Asimov" data set with 7% variation of the number of efficient wires in the upstream part of the detector. Statistical uncertainties are taken from the Hessian matrix. 95
8.8 The post-fit cross sections for flux averaged energies inside each neutron time of flight bin. The Statistical error is calculated using MINOS[58] algorithm. 96
8.9 The post-fit "elastic" category parameter values for each neutron time of flight. The Statistical error is calculated using Hessian matrix. 96
8.10 The post-fit "other" category parameter values for each neutron time of flight. The Statistical error is calculated using Hessian matrix. 96

Acknowledgements

I would like to thank Professor Clark McGrew for giving me the opportunity to learn, study, and contribute to the field of particle physics. Throughout the duration of my Ph.D., he always took the time to answer my questions, and discuss ideas. I also would like to thank my committee:

Dr. Dmitri Kharzeev

Dr. Eden Figueroa

Dr. Steven Kettell

for their time and assistance in my academic pursuits.

I would like to thank CAPTAIN collaboration and it's leader Christopher M. Mauger for giving me an opportunity to learn and be a part of all the aspects of the experiment.

Thank you to all members of the NNGroup for the support, fun physics discussions, and advice throughout the duration of our physics careers. I will definitely miss our weekly meetings. Special thanks to Chang Kee Jung, who's great hospitality and invaluable advises helped through all my years at Stony Brook. Thank you to all my friends that I met at Stony Brook. You changed my world view and helped me to finish this work in many ways.

Thank you to my family, especially to my wonderful wife for the constant support and for encouraging me to pursue my passion. If not for her support, my Ph.D. would take at least a couple more years.

Chapter 1

Introduction

Neutrino is an electrically neutral elementary particle with half-integer spin, which interacts with matter only through weak and gravitational interactions. These elusive particles rightfully stay in the spotlight of modern science. Through the past few decades, neutrino physics evolved from the brilliant theoretical guess to a systematic studying of the neutrino properties and using it as a research tool in many areas of physics. Neutrinos immensely extended our knowledge about the Universe, and they keep being one of the top candidates for the search of a new physics beyond the Standard Model.

The Standard Model successfully predicts three neutrino flavors: ν_e , ν_μ , and ν_τ in correspondence with the three charged leptons, which was proven experimentally with high precision. The Standard Model predicts that neutrinos have no mass; however, the discovery of the neutrino oscillations proved overwise. The oscillation hypothesis comes with the fact, that neutrino mass eigenstates are made up of linear combinations of weak interaction eigenstates (flavor eigenstates). The mixing matrix can be described by three Euler angles θ_{12}, θ_{13}, and θ_{23}, as well as by the CP-violating phase δ_{CP} (with two additional CP-violating phases if neutrinos are Majorana particles). The probability of oscillations for each flavor also strongly depends on the length neutrino traveled prior to interaction and it's energy.

Neutrino detection plays a crucial role in studying neutrino oscillations as well as other properties. Being electrically neutral particles with extremely low cross sections, neutrinos are impossible to detect directly. Thus, measurement of the incoming neutrino energy, so needed for neutrino oscillation probability, comes from the kinematics of outgoing particles.

The LArTPC technology, originally proposed for neutrino detectors [1] as an analog to bubble chambers, where the charged particle's tracks could be clearly seen by eye, is now being used in multiple neutrino experiments [2–5]. This detection method has high precision and low energy threshold, which together allows

highly detailed reconstruction of neutrino events. As a charged particle passes through a medium, it creates ionisation. In a Liquid Argon TPC, an electric field causes the produced electrons to drift to wires at the top(bottom) of the detector. The drift time and the position of the hit wire are combined to provide a 3D reconstruction of the event. On the other hand, neutrons are produced as well. Like neutrinos, neutrons have no electric charge and can't be directly detected. However, they carry a considerable amount of energy. This energy escapes detection, thus provide a significant uncertainty to neutrino energy reconstruction and, as a result, neutrino oscillation probability. Models used to estimate missing energy, including neutrons, have large unconstrained uncertainties. In order to improve neutrino energy reconstruction in Liquid Argon detector, precise measurement of neutron cross section in Liquid Argon is needed for a broad range of energies. Prior to this work, Neutron-Argon cross section data was only published up to 50 MeV of kinetic energy[6]. This thesis presets first measurement of thew neutron cross section on Argon between 100 and 800 MeV. The result of the presented work was published in PRL in July 2019[7]. The analysis uses data from mini-CAPTAIN detector, taken at WNR facility at Los Alamos National Lab.

Chapter 2 gives a brief history of neutrino physics in general and discussion of its theoretical and experimental development. The phenomenology of neutrino oscillations in a vacuum and matter is introduced, as well as the most common neutrino interactions based on its energy. The chapter finishes with a brief description of the DUNE experiment and introduces the importance of neutron study for Liquid Argon neutrino experiments.

Chapter 3 focuses on the experimental setup of the CAPTAIN experiment, including the miniCAPTAIN detector and LANCE neutron beam.

Chapter 4 introduces event reconstruction used in the analysis of the neutron data from the miniCAPTAIN detector. It describes the reconstruction algorithms for the Time Projection Chamber(TPC) as well as Photon detection System(PDS).

Chapter 5 describes the analysis of the miniCAPTAIN detector and reconstruction algorithms performances using cosmic data alongside neutron beam data.

Chapter 6 focuses on developing a Monte Carlo simulation of the detector and neutron beam, resembling features observed in the data.

Chapters 7 and 8 are discussing the measurement of neutron cross section in liquid argon. First, chapter 7 presents the initial technique of measuring the neutron cross section derived from the neutron beam attenuation in the detector. Second, chapter 8 introduces the extension of this method, involving developing and performing Data/MC fit. The last chapter gives a summary and a discussion of the prospect of this analysis.

Chapter 2

Neutrino physics

The study of neutron interactions in Liquid Argon carries great importance for neutrino physics. To establish this statement this chapter first discusses a brief history of neutrino physics, followed by the discussion on neutrino interactions and oscillations in a vacuum and matter. The last part of the chapter discusses the DUNE experiment and introduces challenges that neutrons bring in neutrino energy reconstruction in general and in Liquid Argon detectors in particular.

2.1 Standard model

The Standard Model of particle physics (SM) [8–12] is a modern theory that describes the structure and interactions of elementary particles. It most fully reflects the picture of the physical world at the moment. Within the framework of this theory, all matter consists of 12 structureless fermions (and their antiparticles). In particular, there are 6 leptons separated into charged particles e^-, μ^-, and τ^- with negative charge and their neutral counterparts ν_e,ν_μ, and ν_τ, respectively. The other 6 fermions are called quarks and have fractional charge of $+2/3$ (u,c,t) or $-1/3$ (d,s,b). With the electric charge and spin, quarks also carry a "color" charge (red, blue, green). Colorless combinations of quarks can form hadrons. Combinations of three quarks are known as baryons, such as protons (uud) or neutrons (udd), and combinations of a quark and an anti-quark are known as mesons. (Fig. 2.1).

All SM particles are interconnected through three fundamental interactions: strong, electromagnetic, and weak. The carriers of interactions are 8 massless gluons (strong) and 4 spin-1 gauge bosons: photon (electromagnetic), $W^\pm$ and Z^0 (weak). Particles can interact through gravitational force as well but SM does not describe it. Neutrinos, as neutral particles, can only participate in weak interactions (and gravitational). On the other hand, the charged leptons interact

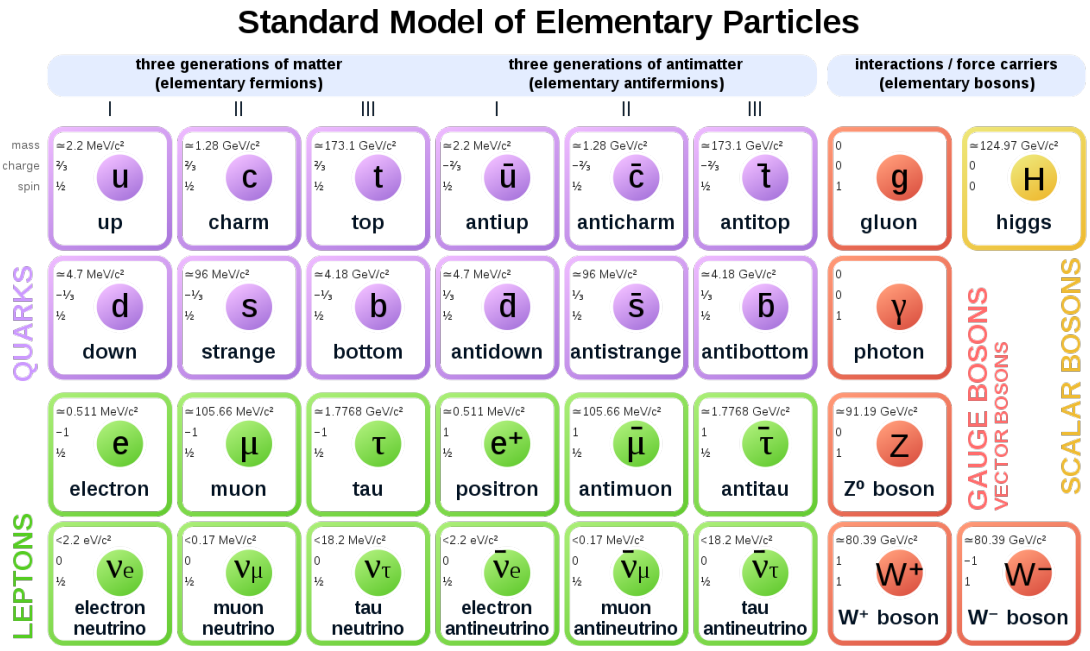

Figure 2.1: Fundamental particles of the Standard Model: three generations of quarks and leptons, and force-carrier gauge bosons.[13]

via the electromagnetic and the weak force. The quarks can interact with all three forces.

2.2 Neutrino oscillations

The discovery of neutrinos came from the study of the β-decay. At the beginning of the twentieth century a problem was discovered - a violation of the laws of conservation of energy, momentum, and angular momentum in β-decay. The Austrian physicist Wolfgang Pauli in 1930 introduced the hypothesis that in β-decay a new particle is born simultaneously with the electron, which carries away the missing part of the energy. According to the hypothesis, this particle should have had a half-integer spin and a very small mass[14]. This mysterious particle turned out to be a neutrino as we know it today.

According to the SM, only left-handed (spin is antiparallel to momentum) neutrinos and right-handed antineutrinos can interact with matter due to V - A nature of weak interactions[15]. Neutrinos have no electric charge and interact through the exchange of $W_{\pm}$ (charged currents) and Z_0 (neutral currents) bosons.

A weak charged current connecting an electron and an electron neutrino has the following form:

$$j^{\mu}_{weak} \propto \bar{e}\gamma^{\mu}(1-\gamma^{5})\nu_{e} \tag{2.1}$$

which selects the left-handed neutrino component, ν_L, and thus excludes the right-handed neutrino component, ν_R, from all weak processes. In the SM, the mass term of the Lagrangian connects the left and right components of the particles:

$$\mathcal{L} = -m\psi\bar{\psi} = -m(\bar{\psi}_L\psi_R + \bar{\psi}_R\psi_L) \tag{2.2}$$

Since SM predicts that right-handed neutrinos do not exist, neutrino mass is not generated in SM. The fact that neutrinos have mass is the only experimentally observed phenomenon not predicted by the Standard Model. Neutrino oscillations were theoretically predicted by Bruno Pontecorvo in 1957. However, at that time, the theory was not reserved well by the scientific community. The first experimental hint for the existence of neutrino oscillations came almost 10 years later in 1960's from the experiment designed by Ray Davis in South Dakota[16]. The experiment measured with high precision, that neutrino flux from the nuclear fusion reactions taking place in the Sun is just 1/3 of its theoretical prediction. Later, the hypothesis of solar neutrino oscillations was confirmed by the Kamiokande experiment in 1980s, GALLEX/GNO [17] and SAGE [18] in 1990. The oscillations of neutrinos were produced by the interaction of cosmic rays with the atmosphere established by the Super-Kamiokande experiment in 1998[19]. The KamLAND experiment in 2003 demonstrated for the first time that the reactor neutrinos oscillate as well [20][21].

2.2.1 Neutrino Oscillation theory

Neutrino oscillations is a process of complete or partial change of the flavor of a neutrino beam moving in a vacuum or matter. Observation of neutrino oscillations is possible if neutrino has mass and the mixing hypothesis is realized. In this case, flavor and mass eigenstates of neutrinos are mixed by:

$$|\nu_{\alpha}\rangle = \sum_{i=1}^{n=3} U^{*}_{\alpha i} |\nu_i\rangle , \quad \alpha = e, \mu, \tau \tag{2.3}$$

The $|\nu_{\alpha}\rangle$ in Eq. 2.3 represents 3 flavor eigenstates of neutrino. Extra neutrino species can exist. However, experiments that measure the decay width of Z boson at LEP and SLC electron-positron colliders provide $N_{\nu} = 2.984 \pm 0.008$[22]. This still opens the possibility of the existence of neutrinos with mass above the half of Z boson mass or light sterile neutrinos that do not interact through SM forces. The $|\nu_i\rangle$ in Eq. 2.3 represents 3 mass eigenstates of neutrino and U is mixing unitary

PMNS matrix. The mixing matrix is named after B. Pontecorvo, Z. Maki, M. Nakagawa, and S. Sakata. As mentioned before, B. Pontecorvo first predicted the existence of the neutrino oscillations, while Z. Maki, M. Nakagawa, and S. Sakata introduced the fist matrix for two generations of neutrino oscillations. The PMNS matrix in case of three-flavor oscillations take a form :

$$U = \begin{pmatrix} 1 & 0 & 0 \\ 0 & c_{23} & s_{23} \\ 0 & -s_{23} & c_{23} \end{pmatrix} \begin{pmatrix} c_{13} & 0 & s_{13}e^{-i\delta_{CP}} \\ 0 & 1 & 0 \\ -s_{13}e^{-i\delta_{CP}} & 0 & c_{13} \end{pmatrix} \begin{pmatrix} c_{12} & s_{12} & 0 \\ -s_{12} & c_{12} & 0 \\ 0 & 0 & 1 \end{pmatrix} \begin{pmatrix} 1 & 0 & 0 \\ 0 & e^{i\alpha_{21}/2} & 0 \\ 0 & 0 & e^{i\alpha_{31}/2} \end{pmatrix} \tag{2.4}$$

where $c_{ij} = cos\theta_{ij}$, $s_{ij} = sin\theta_{ij}$.

The PMNS matrix in the Eq. 2.4 is parameterized with three mixing angles θ_{12}, θ_{13}, θ_{23}, and a CP-violating phase δ_{CP} . The matrix on the second line of the equation is only added if the neutrinos are Majorana particles and excluded if they are Dirac particles.

While only neutrino flavor eigenstates are observed, neutrinos propagate via its mass eigenstates:

$$|\nu_i(t)\rangle = e^{-iE_it} |\nu_i(0)\rangle \tag{2.5}$$

In relativistic limit $p_i \gg m_i$. Since neutrino has very small mass the neutrino momentum is approximately its energy $p \approx E$. Also neutrino travels with almost a speed of light setting $t \approx L$ (c=1). Thus, the energy of the neutrino can be written as:

$$E_i = \sqrt{p^2 + m^2} \approx p_i + \frac{m_i^2}{2p_i} \approx E + \frac{m_i^2}{2E_i} \tag{2.6}$$

The Equation 2.5 in this case takes a form of :

$$|\nu_i(t)\rangle = e^{-im_i^2 \frac{L}{2E_i}} |\nu_i(0)\rangle \tag{2.7}$$

The propagation of the flavor eigenstates can be obtained by plugging the final equation 2.7 into equation 2.3 :

$$|\nu_\alpha(t)\rangle = \sum_{i=1}^{n=3} U_{\alpha i}^* e^{-im_i^2 \frac{L}{2E_i}} |\nu_i(0)\rangle \tag{2.8}$$

The equation 2.3 can be inverted using the unitarity of the PMNS matrix

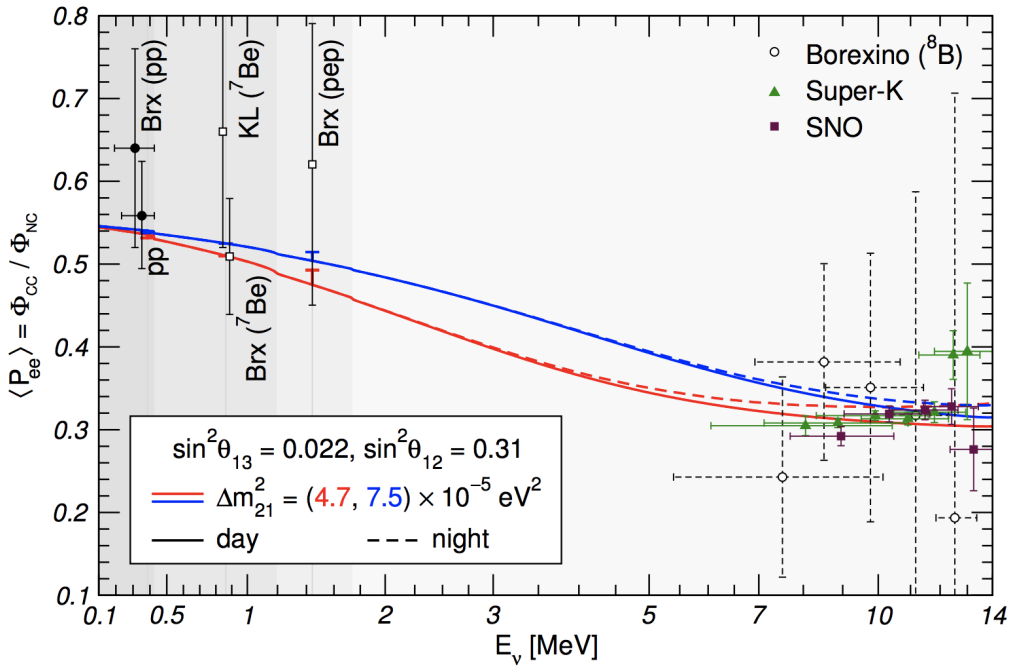

Figure 2.2: Electron neutrino survival probability($P_{\nu_e \to \nu_e}$) as a function of E_ν. Data points are the results of Borexino , SNO, and SuperKamiokande experiment. Blue and red curves are theoretical prediction for different values of Δm^2_{21}[23].

and in combination with the equation 2.8 it provides the probability of neutrino oscillations with time in a vacuum:

$$\begin{aligned} P_{\alpha\to\beta} &= |\langle\nu_\beta|\nu_\alpha(t)\rangle| = \sum_i U^*_{\alpha i}U_{\beta i}U_{\alpha j}U^*_{\beta j}e^{-i\Delta m^2_{ij}\frac{L}{2E_i}} \\ &= \delta_{\alpha\beta} - 4\sum_{i>j}\mathcal{R}e(U^*_{\alpha i}U_{\beta i}U_{\alpha j}U^*_{\beta j})sin^2(\frac{\Delta m^2_{ij}L}{4E}) \\ &+ 2\sum_{i>j}\mathcal{I}m(U^*_{\alpha i}U_{\beta i}U_{\alpha j}U^*_{\beta j})sin(\frac{\Delta m^2_{ij}L}{2E}) \end{aligned} \tag{2.9}$$

According to the equation 2.9, neutrino oscillations can be described with 6 parameters: three mixing angles ($\theta_{12}, \theta_{23}, \theta_{13} \in [0, \frac{\pi}{2}]$), two square masses($\Delta m^2_{12}$ and Δm^2_{23}), and CP-violation phase δ_{CP}. So far only oscillations in vacuum were considered. If neutrinos pass through matter while traveling, an asymmetry arises between the propagation of electron neutrinos and neutrinos of other flavors. It occurs due to the fact that ν_e can interact with electrons of the

medium via W^+(charged current) and Z^0(neutral current) exchange, while ν_μ and ν_τ can interact with electrons only through Z^0 exchange. This difference in the neutrino interactions leads to changes in neutrino oscillation probabilities and so-called the MSW effect(matter effect) named after Mikheyev, Smirnov, and Wolfenstein[24][25]. In order to account for this effect, new potential can be added to the vacuum Hamiltonian:

$$V_{CC} = \pm\sqrt{2}G_F N_e \tag{2.10}$$

where "+" stands for the ν_e and "-" for $\bar{\nu_e}$ interactions, G_F is Fermi constant, and N_e is the number of electrons in the medium (assuming constant density). This potential describes only charged current interactions, while neutral current interactions are much weaker and can be neglected.

The path of obtaining the probability of interactions in a matter is quite convoluted in the case of three-flavor oscillation . However, the result for just two flavor oscillations (ν_e,ν_μ) follows quite easily from the time-dependant Schrodinger's equation with extra potential 2.10. The final probability is written as:

$$P_{\nu_e \to \nu_\mu} = sin^2 2\theta_M sin^2(\frac{\Delta m^2_M L}{4E}) \tag{2.11}$$

where m_M and θ_M are effective parameters, defined by:

$$\begin{aligned} sin2\theta_M &= \frac{sin2\theta}{\sqrt{sin^2 2\theta + (cos2\theta - A)^2}} \\ \Delta m^2_M &= \Delta m^2 \sqrt{sin^2 2\theta + (cos2\theta - A)^2} \end{aligned} \tag{2.12}$$

where $A = \frac{2\sqrt{2}G_F N_e E}{\Delta m^2}$.

For the later discussion, it is important to point out that, aside from described mixing parameters, the probability of neutrino oscillations in both vacuum and matter depends on the ratio between the neutrino's travel distance prior to interaction and its energy ($\propto \frac{L}{E}$). The importance of this comment will be fully introduced in subsection 2.2.4

2.2.2 Neutrino Oscillation measurements

The theoretical formalism, which was described previously, was successfully proven in many experiments. Neutrino oscillation parameters were measured using neutrino coming from the Sun (solar experiments) [18, 27–31], cosmic rays (atmospheric experiments) [19, 32–35], nuclear reactor (reactor experiments) [20, 36–38], and particle accelerators(accelerator experiments)[4, 39, 40]. According to the

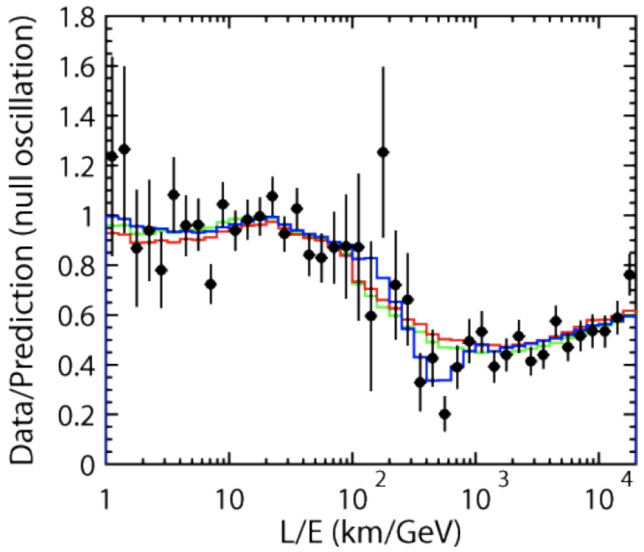

Figure 2.3: Muon neutrino survival probability($P_{\nu_\mu \to \nu_\mu}$) as a function of L/E_ν. Data points are the result of SuperKamiokande experiment. Blue curve - theoretical prediction[26].

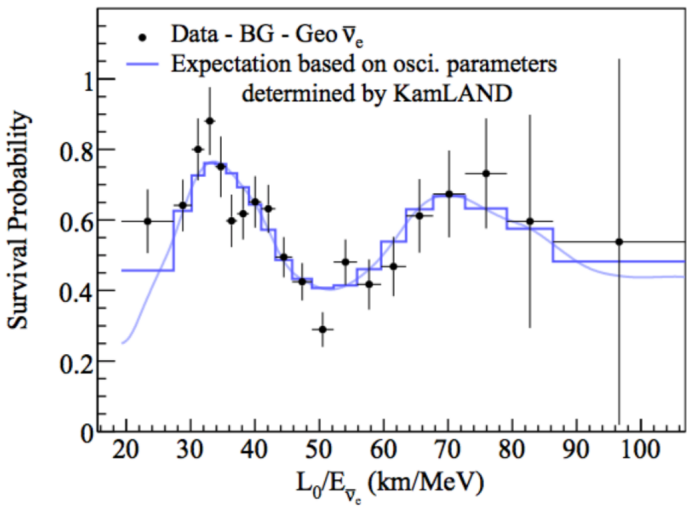

Figure 2.4: Electron anti-neutrino survival probability($P_{\bar{\nu_e} \to \bar{\nu_e}}$) as a function of L/E_ν. Data points are the results of KamLAND experiment. Blue curve - theoretical prediction[21].

Particle Data Group (PDG) [41], current values of neutrino oscillation parameters are the following:

Parameter	Best Fit Value	3σ Range
$\Delta m^2_{21}[10^{-5}eV^2]$	7.37	6.93 - 7.96
$\Delta m^2_{31(23)}[10^{-5}eV^2]$	2.56(2.54)	2.45 - 2.69 (2.42 - 2.66)
$sin^2\theta_{12}$	0.297	0.250 - 0.354
$sin^2\theta_{23}$ (NH)	0.425	0.281 - 0.615
$sin^2\theta_{23}$ (IH)	0.589	0.384 - 0.636
$sin^2\theta_{13}$ (NH)	0.0215	0.0190 - 0.0240
$sin^2\theta_{13}$ (IH)	0.0216	0.0190 - 0.0242
$sin^2\theta_{13}$ (NH)	0.0215	0.0190 - 0.0240
δ/π	1.38(1.31)	2σ: (1.0-1.9) (2σ: (0.92-1.88))

Table 2.1: Current values of oscillation parameters based on the results of the global fit. The data is taken from [41].

The sign of Δm^2_{32} is still unknown. Thus, Table 2.1 provides values for both, Normal mass hierarchy ($m_3 < m_1 < m_2$) and Inverse mass hierarchy ($m_1 < m_2 < m_3$). Figures 2.2,2.3, and 2.4 represent neutrino survival probabilities as a function of the ratio L/E_ν measured in solar, atmospheric, and reactor experiments, respectively.

2.2.3 Neutrino interactions

The SM model, described in section 2.1 established the possibility for the neutrino to interact only via the weak force, which separated into charged current interactions ($W^\pm$ boson exchange) and neutral current (Z^0 boson exchange). Like neutrino oscillation probability, the neutrino interaction cross section as well as it's primary interaction mode greatly depends on incoming neutrino energy. The measured total cross section for neutrino and antineutrino is shown on fig. 2.5. The antineutrino cross section is about three times lower than the neutrino cross section due to the opposite chirality.

As represented on fig 2.5 neutrino (antineutrino) has three main interaction modes called quasi-elastic scattering(QE), resonant production(RES), and deep inelastic scattering(DIS). In order to perform the oscillation analysis, all neutrino reactions should be understood.

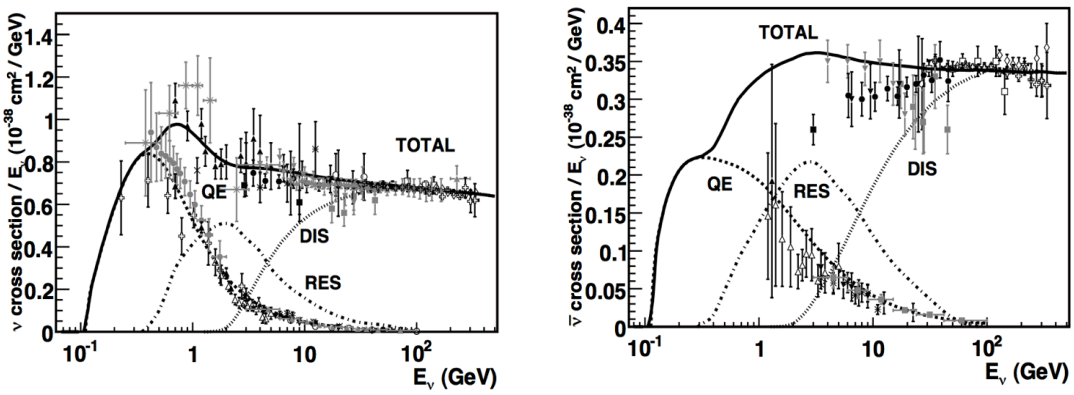

(a) neutrino cross section

(b) antineutrino cross section

Figure 2.5: Neutrino(a) and antineutrino(b) cross sections as a fiction of energy with overlaid data up to 2012. Solid line represents theoretical prediction for total cross section and dashed lines represent quasi-elastic scattering(QE), resonant production(RES), and deep inelastic scattering(DIS) cross sections[42].

The dominant process for sub-GeV neutrino interactions (0.1-1.5 GeV) is the quasi-elastic mode (QE) (Fig 2.6(a)). In this mode, neutrino interacts with nucleon as a whole through the exchange of $W^{\pm}$ boson(CCQE) or Z^0 boson(NCQE).

As the neutrino energy increases above ∼1GeV, the target nucleon can be exited into producing baryonic resonance, which rapidly decays into a nucleon and a pion. However, the neutrino still interacts with the nucleon as a whole. This reaction type is called resonant production(RES) (Fig 2.6(b)). Both CC and NC channels are possible for this mode. In rare cases, a neutrino can interact coherently with the entire nucleus producing a single pion in a final state, leaving the nucleus intact. It is called coherent scattering (COH) (Fig 2.6(c)).

At high energies, neutrino starts to interact with quarks inside the target nucleus directly. It results in the production of hydroponic showers. Such processes are called Deep inelastic scattering(DIS)(Fig 2.6(d)). They start to occur at about 2.5GeV, but starting to be the dominant interaction at or above 5GeV.

2.2.4 Liquid Argon and Neutrons

The discussion of neutrino physics in previous sections established two important ideas. First, neutrino oscillation analysis is extremely dependent on the precise measurement of neutrino energy. Second, neutrino interactions above 1GeV start to produce neutrons in a final state. These neutrons pose a significant challenge for neutrino energy reconstructions since they can not be directly detected. In this section, the DUNE experiment is introduced and used as an example to show

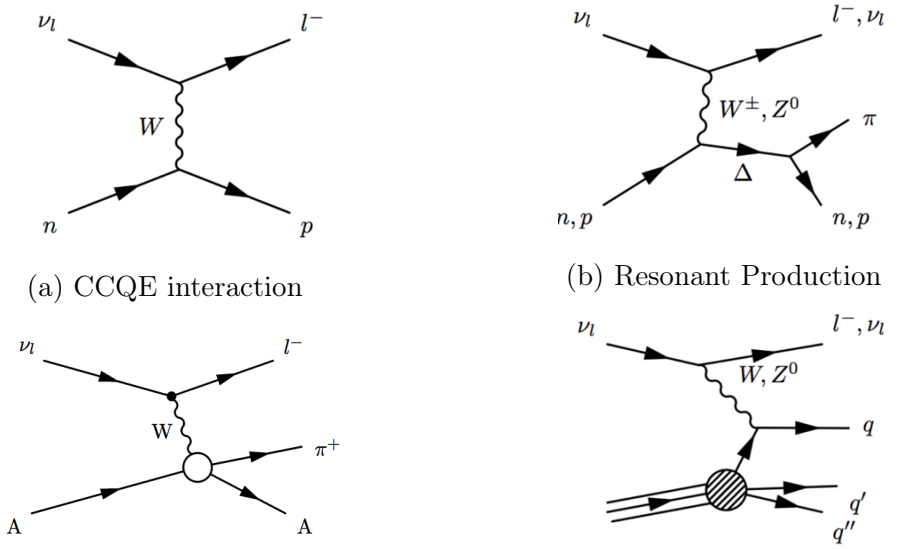

(a) CCQE interaction

(b) Resonant Production

(c) Coherent Scattering

(d) Dip Inelastic Scattering

Figure 2.6: Feynman diagrams for main neutrino CC interaction modes.

the significance of neutron study in Liquid Argon. DUNE experiment is chosen since CAPTAIN sets the primary goal to make measurement relevant for this experiment. However, I believe that the results of this work will be useful for other Liquid Argon neutrino experiments as well.

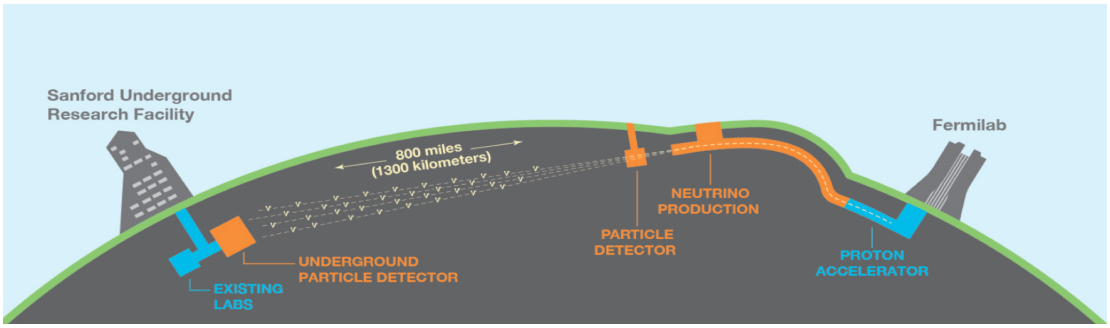

Figure 2.7: The illustration of the future DUNE setup proposed in [1]

DUNE experiment

DUNE is a future long-baseline neutrino experiment [2, 43]. The main goals of the experiments are the measurement of neutrino oscillation parameters and search

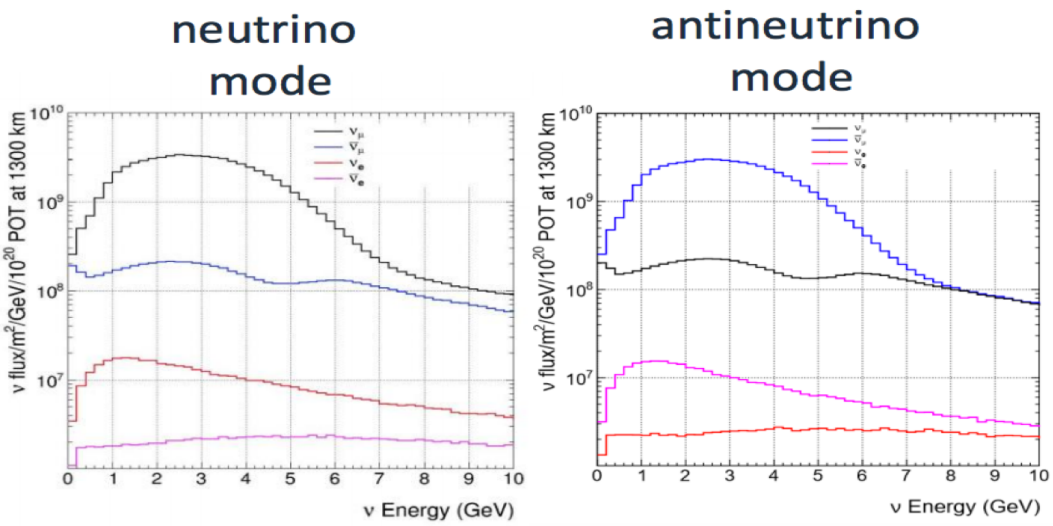

Figure 2.8: Neutrino/Antineutrino beam spectrum, which will be used in DUNE experiment[2].

of the CP-violation phase. Moreover, the experiment will be sensitive to the neutrino mass Hierarchy measure. In addition to neutrino oscillations, the DUNE collaboration proposed the study of supernova physics (most of the energy from supernova is carried away by neutrinos) and proton decay search. For the neutrino oscillation measurement, the experiment will be using neutrino/antineutrino beam, produced at Fermi National Accelerator Laboratory in Batavia, Illinois. The neutrino energy beam, provided by Fermilab, will cover the energy range starting at 500MeV(Fig. 2.8).

The proposed design of the experiment consists of two detectors. The small near detector will record particle interactions near the source of the beam. The design of the near detector is still under development. The much larger far detector will be placed 1.5 kilometers under the surface at the Sanford Underground Research Laboratory in Lead, South Dakota. The distance, that neutrinos will be travailing through the Earth between the target and far detector will be 1300km (Fig. 2.7). The far detector is planned to consist of four separate modules to be installed in two long caverns. The detector modules will hold a combined total of 68,000 tons of liquid argon (LAr), which is the target material for neutrino interactions in DUNE.

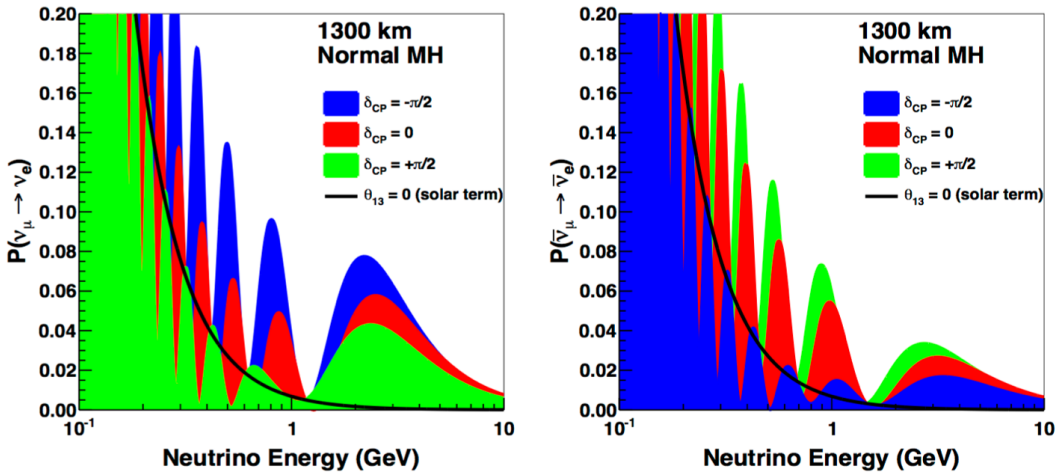

Figure 2.9: The theoretical prediction of the probability of neutrino/antineutrino oscillations with normal mass hierarchy for 1300km flight path[2].

Neutron study for DUNE experiment

Using theoretical formalism, described in section 2.2.1, the probability of neutrino/antineutrino oscillations with normal mass hierarchy for 1300km (DUNE baseline) can be obtained. The result is taken from [2] and shown in Fig 2.9, where the red, blue, and green colors represent different values of the CP-violation phase and solid black lines give oscillation probability with $\theta_{13} = 0$.

From Fig. 2.9, it is clear that the small shift in neutrino energy can result in big change in neutrino oscillation probability. Since incoming neutrino energy can't be measured directly, it must be carefully reconstructed. Neutrino energy is reconstructed based on kinematics of outgoing particles (including neutrons). As neutrinos, neutron's energy can't be measured directly. Neutrons carry considerable energy that can escape detection, thus provide a significant uncertainty to neutrino energy reconstruction.

Neutrons will play a major role in DUNE. The proposed neutrino energy window (Fig. 2.8) covers all types of neutrino interactions described in section 2.2.3. The resonance production(RES) mode and especially deep inelastic scattering(DIS) produce a significant number of neutrons in a final state. The effect of neutrons can be estimated using neutrino simulation with GENIE [44] . Figures 2.10(a) and 2.10(b) shows the initial neutrino/antineutrino energy spectrum in blue and "reconstructed" energy spectrum without neutrons in red. The reconstructed spectrum in this case means the sum of energies of all outgoing particles except neutrons.

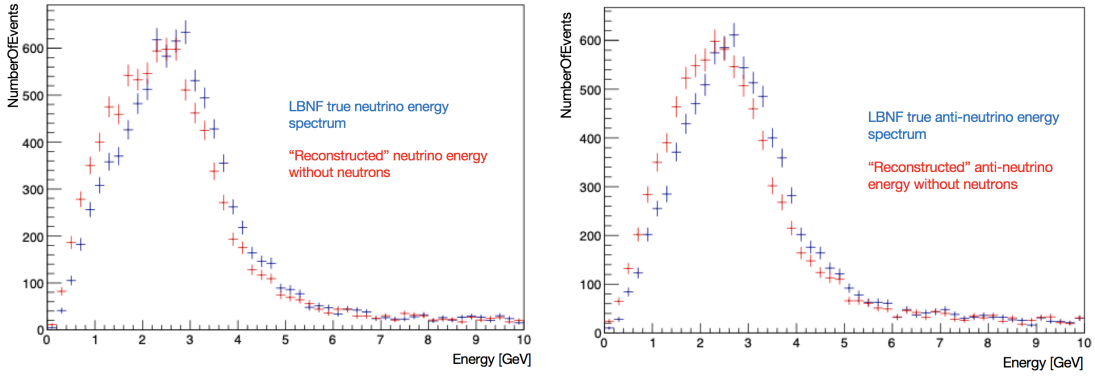

(a) Neutrino simulation

(b) Antineutrino simulation

Figure 2.10: Neutrino(a) and antineutrino(b) beams simulated using GENIE $v2\_12\_8$[44]. Blue - true neutrino/antineutrino energy spectrum. Red - "reconstructed" neutrino energies excluding neutrons.

Fig 2.11 shows the energy that will be carried away by neutrons in the DUNE experiment. The energy range varies from several MeV to 2GeV. In order to model neutron energy, the cross section measurement for this energy should exist. However, prior to the work of CAPTAIN collaboration, the Neutron-Argon cross section data was only published for only up to 50 MeV of kinetic energy [6](Fig 2.12).

2.3 Neutron Cross Section Definition

The goal of this work and CAPTAIN collaboration is to measure the Neutron-Argon cross section in energy range relevant for DUNE (between 100MeV and 800 MeV). Throughout this work, the measured cross section will be called total neutron cross section in liquid argon. However, due to chosen measurement methods and specifics of the experimental setup, the measured cross section should be perceived as a beam depletion cross section. In other words, it is a cross section to remove the neutron from the certain area around the beam (25mm radius and 50mm radius).

The CAPTAIN experimental setup, as well as cross section measurement results, will be described in the next chapters.

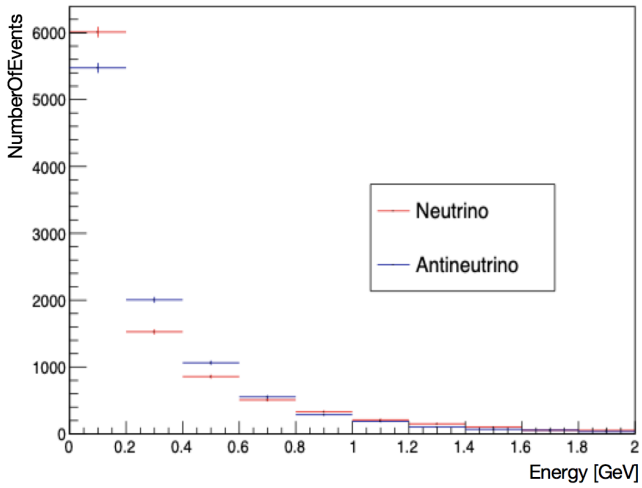

Figure 2.11: The energy carried away by neutrons in neutrino(red) and antineutrino(blue) interactions. The calculation is made by subtracting true neutrino/antineutrino energy and "reconstructed" neutrino energies excluding neutrons in each event.

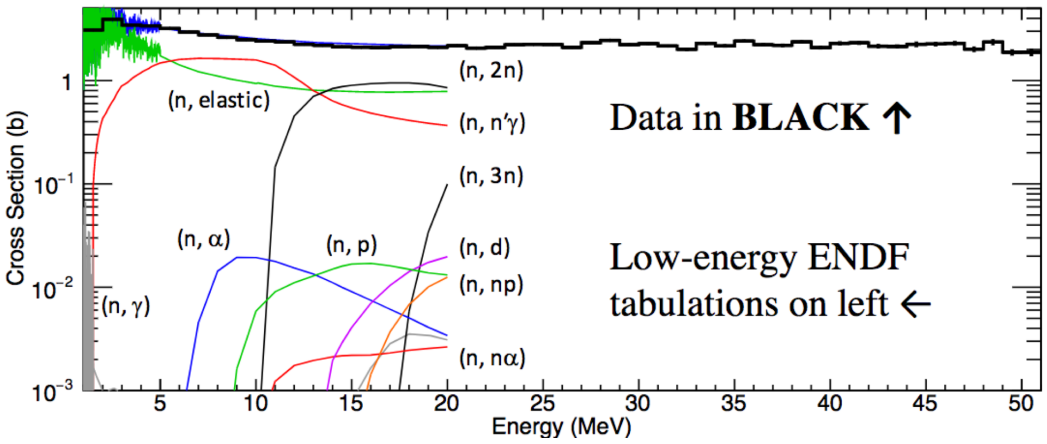

Figure 2.12: Existing world data for neutron cross sections in liquid argon. Solid black line is experimental data. Colored lines are theoretical partial cross section calculations made by “ENDF”[6].

Chapter 3

CAPTAIN experimental setup

The CAPTAIN (The Cryogenic Apparatus for Precision Tests of Argon Interactions with Neutrinos) experimental setup includes descriptions of the miniCAPTAIN detector, the WNR facility at Los Alamos National Laboratory, and the neutron beam provided by LANSCE[45]. This chapter focuses on all of these aspects and is finished with the discussion of the data set, collected during miniCAPTAIN neutron run during summer 2017. The chapter is mostly based on the miniCAPTAIN detector design paper published by CAPTAIN collaboration[46].

3.1 MiniCAPTAIN detector

Similar to DUNE, the miniCAPTAIN detector in its essence is a liquid argon time projection chamber (LArTPC). However, the beam at LANSCE provides neutrons on a wide range of energies; therefore, an additional measure of the incoming neutrons is needed. The miniCAPTAIN detector utilizes the photon detection system(PDS) alongside LArTPC to measure the time of flight of the neutrons as they arrive at the detector and create scintillation light. The detector is mounted on a cart so it can be rolled into and out of the neutron beam. Figure 3.1(a) shows the schematic of the detector while figure 3.1(b) shows the detector at its final assembling stage.

3.1.1 TPC design

The LArTPC in miniCAPTAIN is much smaller than DUNE with 400 kg of instrumented mass. The schematic drawing of the TPC part of the detector is shown in Fig. 3.2. The TPC has a hexagonal shape with an apothem of 50 cm and 32 cm of vertical drift between the cathode at the bottom and the anode at the top. The charged particles traveling through liquid argon create ionization

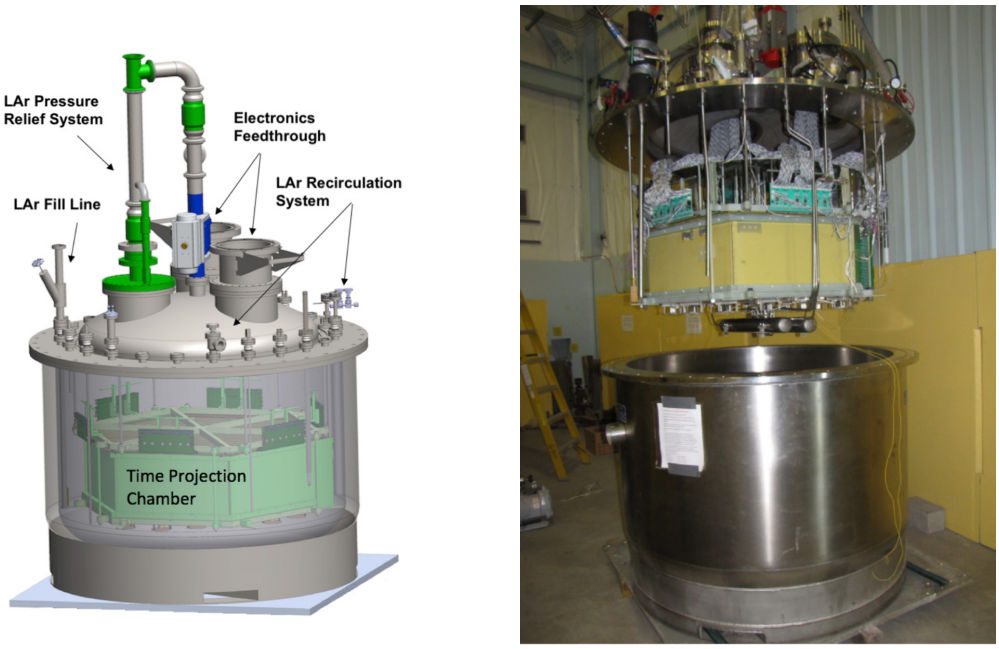

(a) MiniCAPTAIN detector schematic (b) MiniCAPTAIN detector photo

Figure 3.1: The schematic of the miniCAPTAIN detector(a) and the photo of the detector(b) at its final assembling stage[46].

electrons, which are detected using tree wire planes (X, U, and V). The so-called X wire plane is the collection wire plane with wires positioned almost perpendicular to the neutron beam (or X-axis in the coordinate system used in the analysis). The other two planes are induction wire planes called U and V. Wires on these planes are positioned $\pm 60^\circ$ with respect to the collection wire plane or $\pm 30^\circ$ to X-axis. Each wire plane has 337 copper-beryllium wires 75 μm in diameter. The distance between wires is kept 3.125 mm across all wire planes. The schematic of the positions of the wires with respect to the beam and the coordinate system used in the miniCAPTAIN are shown in figure 3.3.

The 500 V/cm electric field applied across the 32 cm TPC volume for the ionization electrons to drift toward wire planes. The provided electric field results in 1.6 $mm/\mu s$ electron drift velocity and maximum 200 μs drift time. The important requirement for the LArTPC is the purity of liquid argon. Both H_2O and O_2 have strong electron attachment rates in the provided electric field[47] and can greatly reduce the detector sensitivity. In order to maintain proper detector sensitivity for the 32 cm vertical drift region in miniCAPTAIN TPC 0.3 and 1.5 ppm concentrations of H_2O and O_2, respectively, are required. The extra purification of industrial liquid argon, delivered to Los Alamos, is performed in

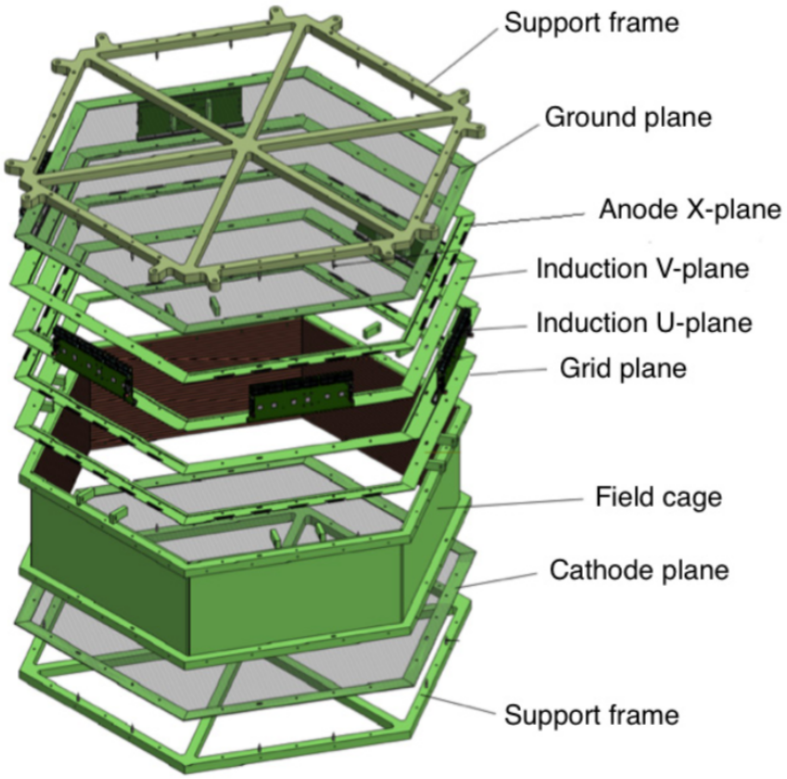

Figure 3.2: The schematic drawing of the TPC part of the miniCAPTAIN detector[46].

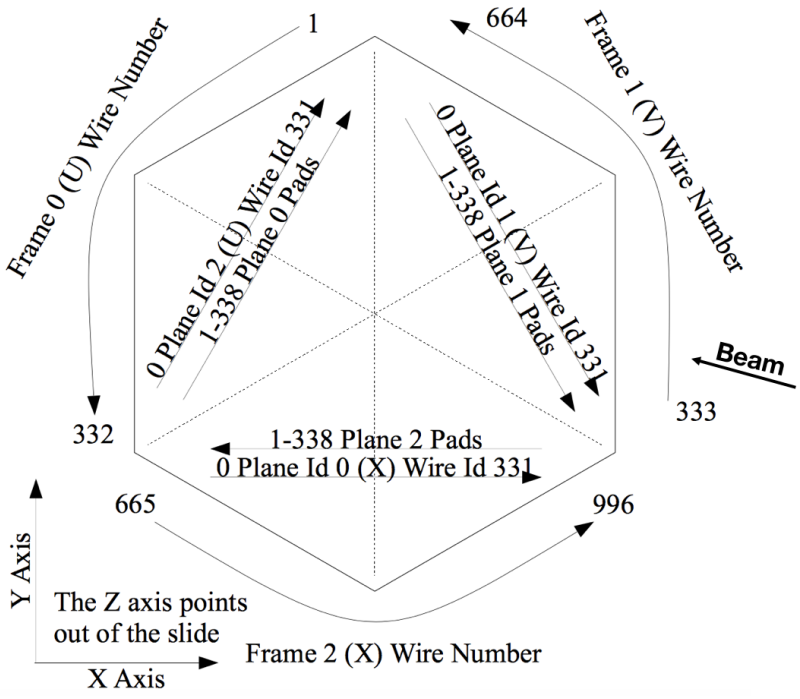

Figure 3.3: The schematic of the positions of the wires with respect to the beam in the miniCAPTAIN. The hexagonal plane of the TPC lays in the XY plane with zero coordinate in the middle of the cryostat. The Z-axis pierces the detector vertically with zero at the top of the cryostat.

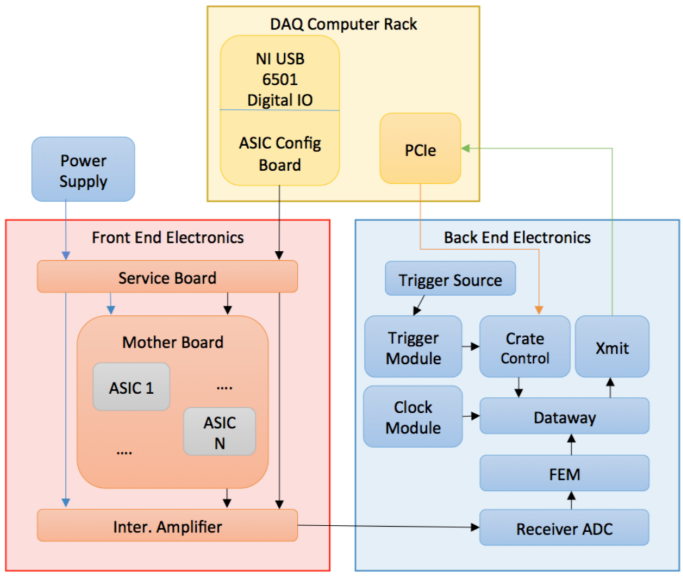

Figure 3.4: The diagram of readout electronics in miniCAPTAIN TPC[46].

three stages: inline filter, gas recirculation system, and a liquid argon purification system was from Criotec Impianti[48]. Figure 3.9(a) shows the construction of the inline filter. The part with a molecular sieve is used to remove H_2O, while and activated copper part serves for removal of excessive O_2. The next purification stage is gas recirculation system shown on figure 3.9(b). The system collects gas from the cryostat, runs if through the SAES cartridges to extract water and oxygen, then condense the remaining gas, and returns it to the cryostat. The last stage of the purification is a filtering system purchased from Criotec Impianti. The system purifies liquid argon by circling it through two tubes with copper-alumina filters inside as shown in figure 3.9(c). The combination of all three purification techniques provided 75 μs electron lifetime (Tab. 5.5), which is sufficient for the measurement.

The electronics used in miniCAPTAIN is separated into three categories. First, the electronics are mounted inside the cryostat and operate in liquid argon. It is called front-end electronics (FEE). The second electronics subsystem is operating outside the cryostat and is responsible for triggering and signal processing. It is called back-end electronics (BEE). The last subsystem is responsible for data acquisition from wire-planes(DAQ). The FEE was designed at Brookhaven National Laboratory and used in MicroBooNE experiment[49]. The design for BEE was developed at Nevis Lab[50]. Figure 3.4 shows the schematic summary of LArTPC

electronics.

3.1.2 PDS design

The photon detection system(PDS) measures the light from neutron interactions to establish the event timing as well as incoming neutron energy. The readout time for LArTPC is measured in milliseconds, while scintillation light detection brings the resolution to nanosecond order of magnitude.

The photon detection system consists of 24 Hamamatsu R8520-506 MOD photomultiplier tubes (PMTs), approximately 1" × 1" × 1" in size each. All PMTs have a borosilicate glass window and a special bialkali photocathode capable of operation at liquid argon temperatures (87 K). The PMTs are mounted on both top and bottom of the cryostat, with 8 PMTs on the top plane and 16 PMTs at the bottom. Figure 3.5 shows the locations of the PMTs. The signal from PMTs is digitized by three CAEN V1720 digitizers. The V1720 is an 8-channel, VME-based digitizer that samples at 250 MS per second (4 ns) at 12 bits. Each digitizer is taking data from 7 PMTs as well radio-frequency (RF) signal coming from the copper coil at the beam target location. Thus, only 21 out of 24 PMTs in miniCAPTAIN are digitized. All three digitizers are taking data separately and synchronized prior to the analysis. The synchronization process is described in details in chapter 4 section 4.3.2.

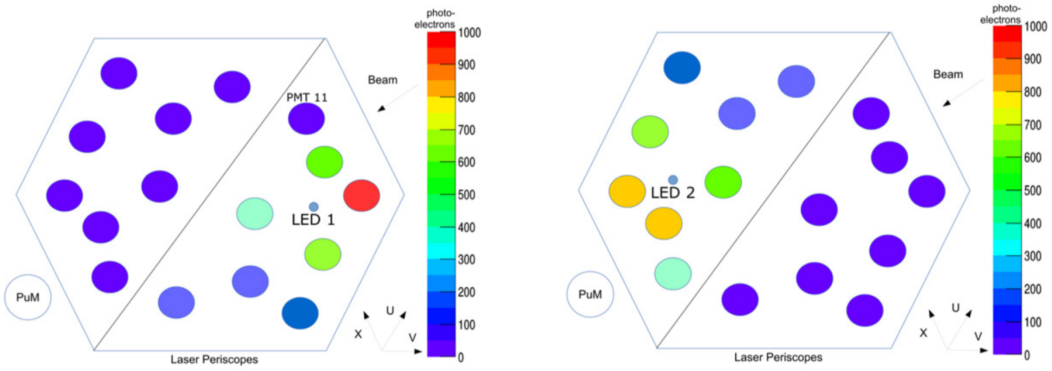

Figure 3.5: The PMT configuration for the PDS system, and the system's response to a calibration LED mounted on the (a) right or (b) left side of the field cage (looking downward)[46].

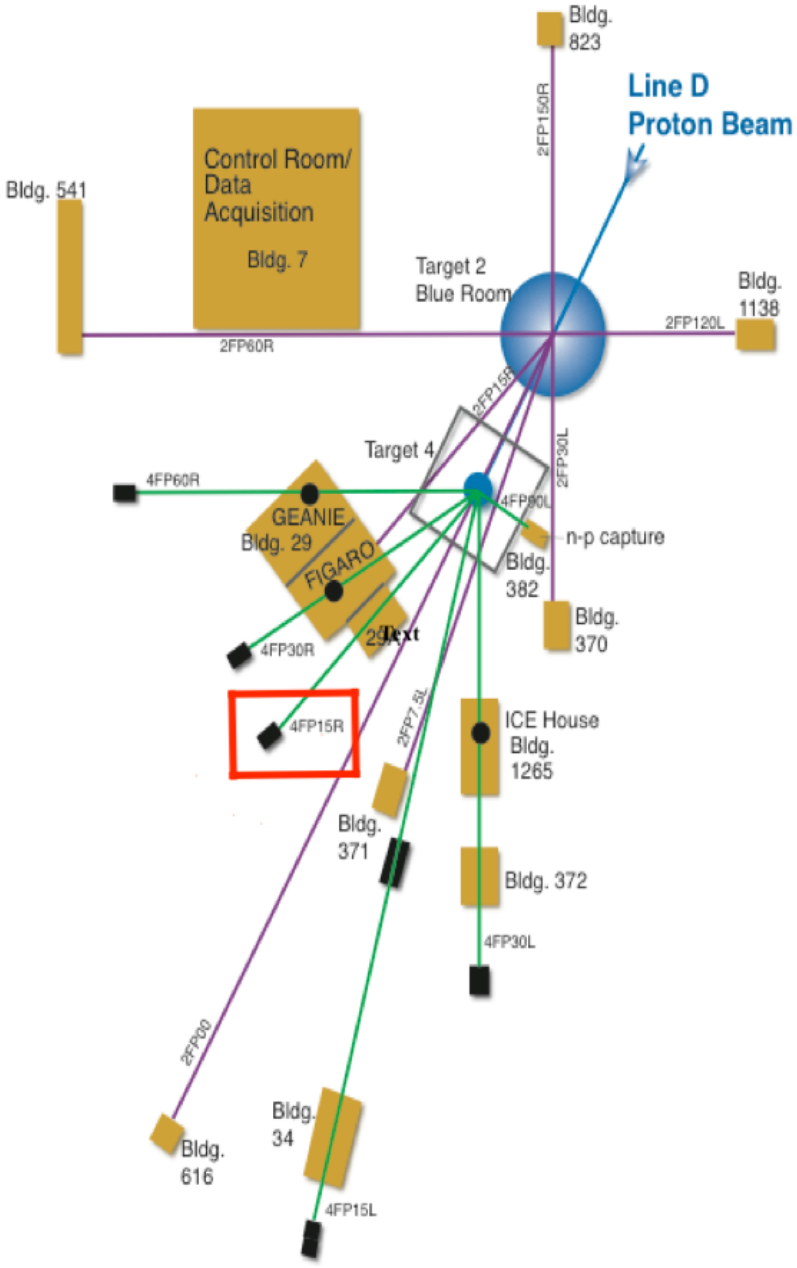

Figure 3.6: The diagrams of different beamlines provided at Target 4 LANSCE facility. The CAPTAIN experiment was positioned at 4FP15R (red square)[45].

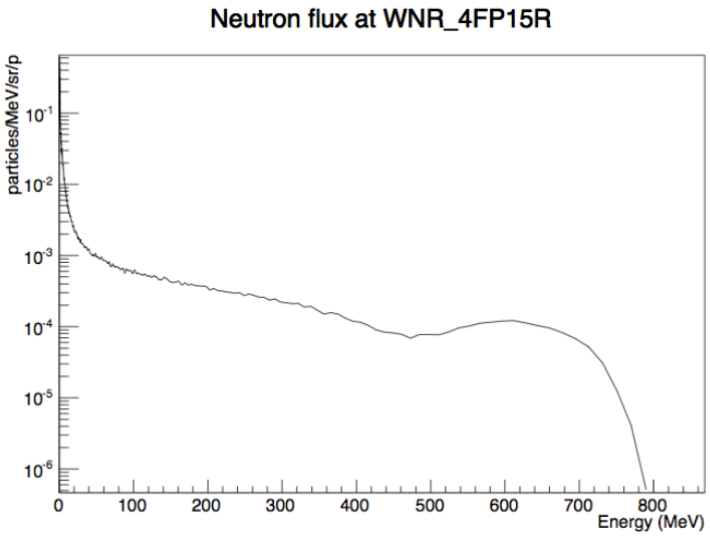

Figure 3.7: The neutron energy spectrum provided by LANL for the CAPTAIN experiment[51].

3.2 Neutron beam

The miniCAPTAIN detector was deployed at the Los Alamos Neutron Science Center (LANSCE) in the Target 4, flight path 15R (4FP15R) beamline of the Weapon Neutron Research (WNR) facility. The Target 4 facility uses a proton beam and tungsten(W) target to produce neutrons. The detector's center was located 23.2m from the target. The schematic of the layout of the facility and experiment beamline is shown in figure 3.6. The facility provides a neutron beam that mimics the cosmic ray spectrum at the Los Alamos altitude (2231m)[51]. The neutron energy spectrum covers energies from 1MeV up to 800MeV (Fig. 3.7).

Two beam structures were provided by the LANSCE. First, the regular beam operation represented in figure 3.8(a). The beam comes in macropulses 625 μs wide, separated by a minimum of 8.3 millisecond. Each macropulse consists of micropulses, which are 100 ps wide and separated by 1.8 μs. The second beam mode was provided specifically for the CAPTAIN experiment. The overall macropulse structure of the beam stayed the same. However, the number of micropulses inside each macropulse was reduced to 3. Thus, micropulses were separated by 199 μs, but had the same 100ps width as in the initial beam mode. Figure 3.8(b) shows the CAPTAIN-specific beam structure with TPC event window on top of it.

Aside from the reduced amount of micropulses per macropulse, extra reduction of neutron flux was required to prevent the event pile-up issues in the TPC where

the drift time was 200 μs. The experiment operated shutters mounted on the beamline to reach a neutron flux of about one neutron per macropulse.

3.3 Detector triggering and Analysis data set

MiniCAPTAIN collected data separately for the TPC and PDS systems. Two data streams were synchronized during the analysis stage described in chapter 4 section 4.3.5. Both systems were set to trigger by the radio-frequency (RF) pulse. The RF pulse is a signal from the copper coil around the target location representing the time protons strike the target. The TPC data acquisition window is 4.75 ms is designed to include 625 μs macropulse along with 1.85 ms and 2.3 ms prior and after the trigger time (fig. 3.8(b)). The detector operation time outside of the macropulse was used to collect cosmic muon data. The PDS system data acquisition window was set to 8 μs and triggered with the arrival of the RF pulse as well. However, the PDS could potentially trigger independent from the RF pulse if enough light was seen in the detector.

The data set used for the analysis was obtained during the CAPTAIN-specific beam structure on August 31, 2017. The analysis is done with approximately 6 hours of neutron data. The cosmic data collected during these hours are used to study detector performance.

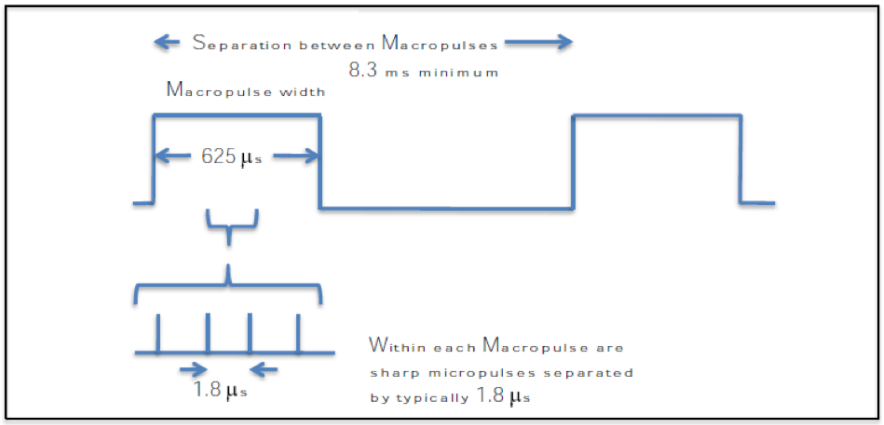

(a) Standard LANSCE beam structure at 4FP15[45]

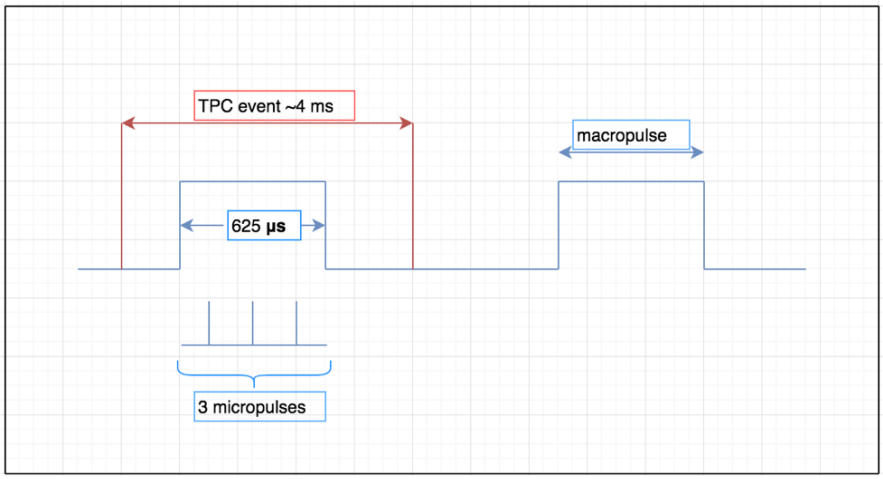

(b) Beam structure provided specifically for the CAPTAIN experiment

Figure 3.8: Two beam setup provided by LANSCE. First, the standard beam structure at 4FP15R(a). Second, the CAPTAIN-specific beam structure(b).

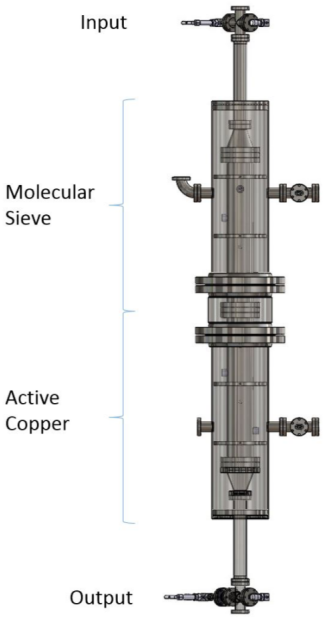

(a) MiniCAPTAIN inline filter

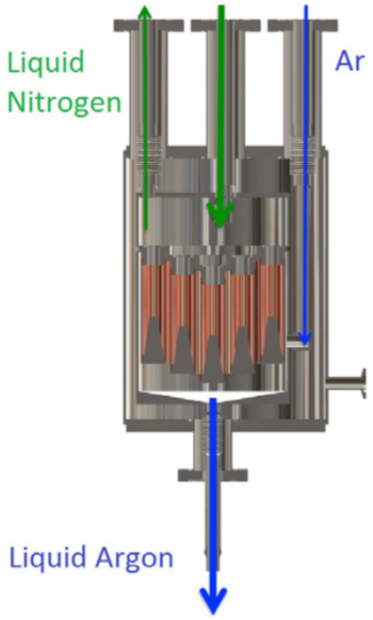

(b) MiniCAPTAIN gas recirculation system

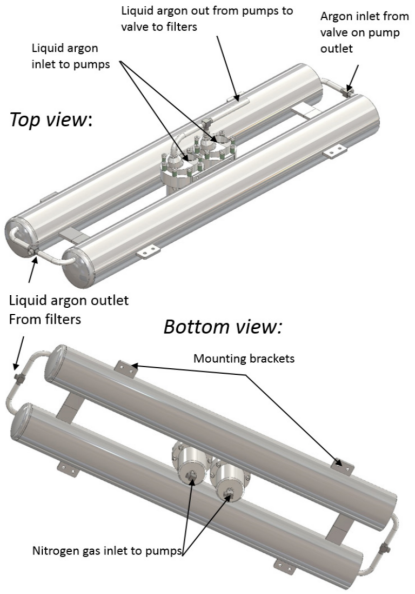

(c) MiniCAPTAIN liquid argon purification system

Figure 3.9: Three argon purification system used in miniCAPTAIN detector: the inline filter(a), the gas recirculation system, and the liquid argon purification system designed by Criotec Impianti[46].

Chapter 4

Reconstruction

MiniCAPTAIN detector uses two independent systems to collect data from neutron interactions. One is LArTPC and the other is PDS as described in the previous chapter. First, "raw" signal in each wire is calibrated and transformed into preliminary hits. Then, event reconstruction for both systems is done separately following by matching events from TPC and PDS to produce the final data set for the analysis. This chapter first described the TPC track reconstruction followed by the PDS event reconstruction. In the end, the chapter introduces the matching algorithm between events from these systems.

4.1 Calibration and "raw" hit finding

The signal from thermal electrons in each wire is calibrated prior to the reconstruction. The current in each wire is estimated using the The Shockley-Ramo theorem. Next, wires should be cleaned from the noise. The Wiener filer is developed to perform that task. Since the filter depends on true (unknown) signal, this signal should be estimated. The filter operates under the hypothesis that the signal is smooth as a function of frequency. The example of the signal estimate using smooth curve is presented in figure 4.1. Next, knowing the signal, the filter is constructed for each wire to remove noise at particular frequencies. The result of the procedure is presented in figure 4.2. The peaks that remain after the filtering are used to make "raw" hits, that will be used in reconstruction. In particular, each "raw" hit carries the information about its wire's number(coordinates), time, and charge integral. The example of the calibrated hit is shown in figures 4.3 and 4.5.

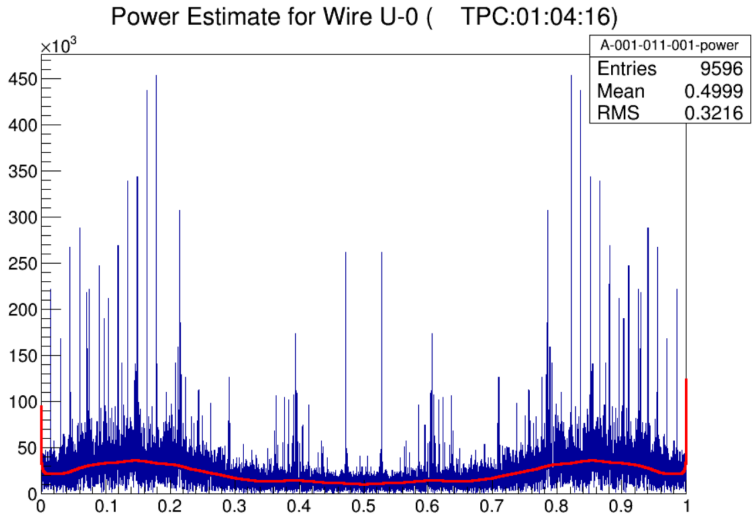

Figure 4.1: The example of the signal from the induction wire plane as a function of frequency. The red curve represents the estimated smooth signal for the filter.

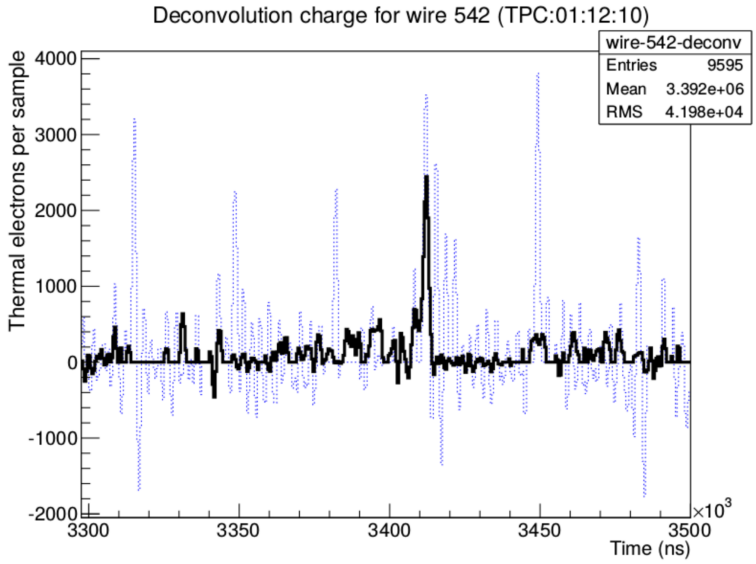

Figure 4.2: The example of the signal from the induction wire plane as a function of time. The dashed blue line represent the signal before the filtering and the black solid line is the final signal after the filtrating.

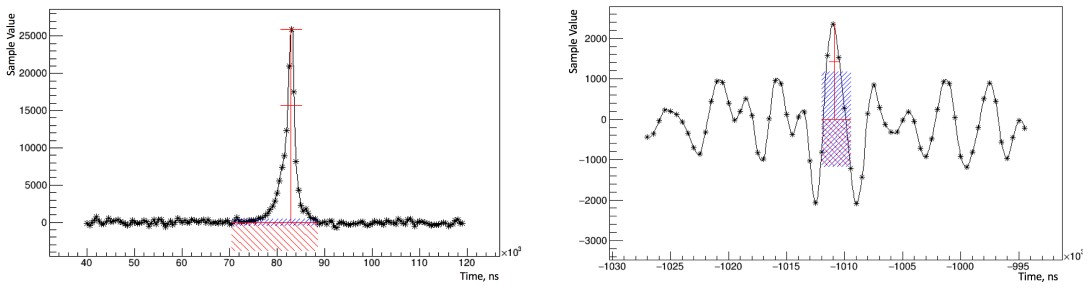

(a) Good X plane Hit

(b) Noise X plane candidate

Figure 4.3: The example of the clear signal hit(a) and the noise hit(b) from collection wire(X-plane). Sample value on the Y-axis is measured in the number calibrated electrons arrived at given wire at a given time.

4.2 TPC Reconstruction

The CAPTAIN experiment operates with neutron interactions in liquid argon. Thus, mostly linear objects are expected in the collected data set. They are mostly coming from protons, pions, and muons from neutron interactions as well as from cosmic muons. Consequently, the reconstruction algorithm in miniCAPTAIN detector LArTPC is designed to handle strait objects with possible small bands from secondary interactions. The track reconstruction process in miniCAPTAIN detector consists of 5 essential steps. Four of them, "Noise Cleaning", "Hit Transfer", "Clustering", and "Path Follow" are applied for each of the three wire planes separately. The last one is "Track Reconstruction" which combines objects from all three planes to form track-like objects and fit them to obtain proper stating positions and directions.

The reconstruction process follows a fixed sequence. First, all three planes go through "Noise Cleaning" algorithms. Second, all raw wire hits are converted into three-dimensional hits. Then, for each plane, these hits are clustered into distinct groups laying strictly on a line. The path following algorithm is applied using these preliminary clusters . It improves the clustering for long and curved objects such as tracks from multiple interactions. After that, clusters from all three planes are combined using time and position information into three-dimensional track-like objects. These objects are fitted to make final objects called tracks.

4.2.1 Noise cleaning

The "Noise Cleaning" algorithm is designed to clean the data from wire planes from obvious noise hits prior to the reconstruction. The X plane is different from U and V planes. The X plane is the collection wire plane. On the other hand,

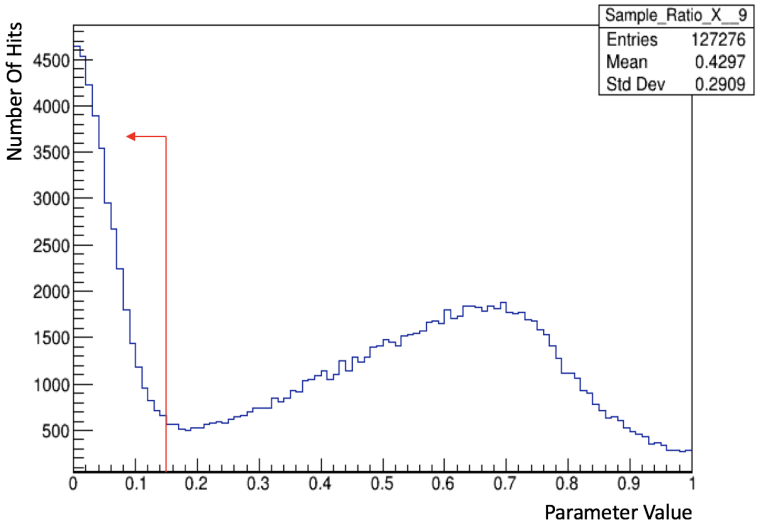

Figure 4.4: The criteria parameter values for all collection wire planes from the analysis data set. The red line show the cut for the parameter.(equation 4.1)

U and V planes are induction planes. Thus, the noise signature is expected to be different for different tips of wire planes. Since X plane is the collection wire plane it provides clear distinction between signal hits (Fig 4.3(a)) and noise hits (Fig 4.3(b)). A proper hit has a clean peak that stands well above the baseline.

However, noise hits are formed from signal fluctuations around zero value. To separate signal hits from the noise the criteria parameter "C_r" is introduced. The data from each wire comes in the form of sample values with assigned time stamps. The sample values are the number of calibrated electrons arrived at the wire at a particular time. Thus, to calculate the criteria parameter first, an absolute value of the sum of all sample values for the hit is taken. Next, it is divided by the sum of absolute values of all hit's sample values:

$$C_r = \frac{\mid \sum_i S_i \mid}{\sum_i \mid S_i \mid}, \tag{4.1}$$

where S_i is a sample value of ith sample and C_r is the criteria parameter. Figure 4.4 represents the value of C_r for all wire hits from the analysis data sample. To eliminate noise on the collection wire plane, the cut for this parameter is chosen to be 0.15.

The U and V planes are induction planes, and there is no clear distinction between noise and signal hit, as shown in figure 4.5. However, a close examination of the data implies that noise forms dense and short in time clusters in each affected

wire. Thus, the noise was partially eliminated from the induction wires by finding these dense in time clusters. The cluster of hits on the induction wire is marked as noise if it has more than 4 hits separated in time by less than 50 microseconds.

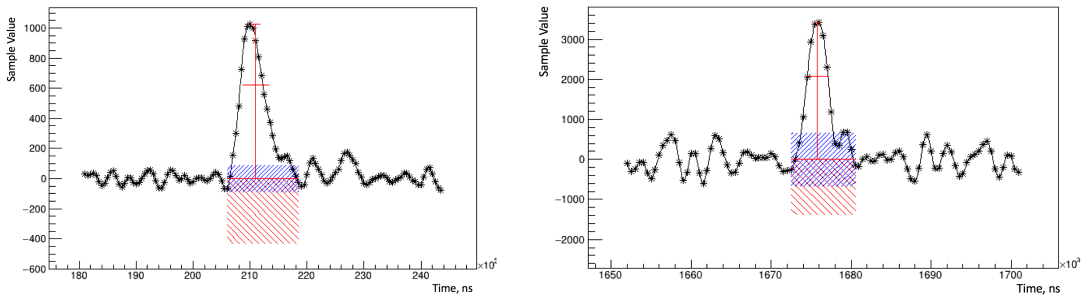

(a) Good U plane hit

(b) Noise U plane candidate

Figure 4.5: The example of the signal hit(a) and the noise hit(b) from one of induction wires(U-plane). Sample value on the Y-axis is measured in the number calibrated electrons arrived at a given wire at a given time.

4.2.2 Hit transfer

The "Hit transfer" algorithm goal is to create hit objects with proper attributes for the following reconstruction steps. The transfer is made for each wire plane separately. The "raw" hit that comes from calibrated data consists of three essential attributes, such as a wire number, time at which this hit appeared, as well as recorded charge. Wire number information provides X and Y coordinates for the hit in a form the coordinates of the wire center. The preliminary Z position of the hit is calculated from the recorded time. The time is multiplied by the drift time of an electron in liquid argon, which is 1.6 $mm/\mu s$. The time counting for wires starts with the TPC trigger. Thus, the preliminary Z coordinate can exceed the size of the detector but is adjusted later using PDS information. The charge, which was calculated as a number of electrons reached the wire, is transferred to the hit without any change. Thus, as an outcome of this reconstruction step, the set of hits for each separate plane is obtained. Each hit has an X, Y, and Z coordinate, as well as a charge assigned to it. Although all three coordinates are assigned for each hit, they technically remain 2D hits and correspond to each wire plane separately.

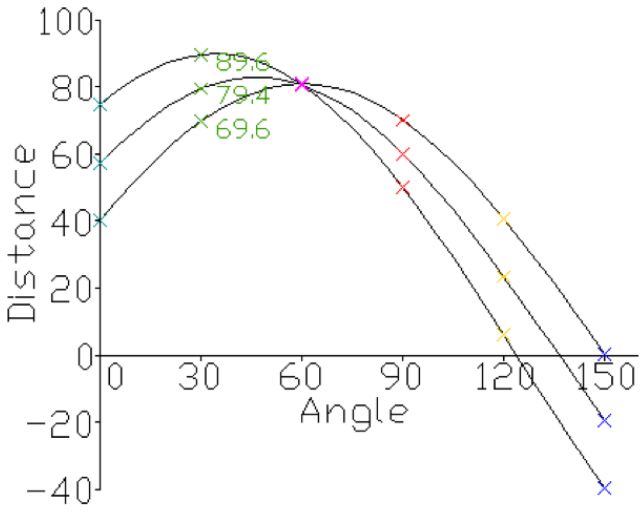

Figure 4.6: Hough (r,θ) space filled with transformed XZ points.

4.2.3 Clustering

The next step of the reconstruction is designed to cluster hits into specific groups. Taking into account the specifics of neutron interactions in liquid argon, most of the expected reconstruction objects are straight tracks. They come from protons, pions, and muons from neutron interactions or cosmic muons. Thus, the target shape of the cluster is set to be a straight line. In order to find straight lines in data efficiently, the Hough Transform algorithm is applied[52]. In general 2D Hough case, the 2D space XZ is chosen. Each point in the XZ space has to be transferred to the parametric space (r,θ) using the equation:

$$r = x \times sin\theta + z \times cos\theta \tag{4.2}$$

More specifically, for each point, r vs θ histogram is filled with all possible combinations of (r,θ) (Fig 4.6).

In Figure 4.6 each black curves correspond to one point from the XZ space. Thus, the crossing of these curves in (r,θ) indicates that point belongs to the same line in XZ space.

The Hough algorithm described above is directly applied to hits derived from the Hit transfer algorithm. However, proper Hough XZ space should be created for each wire plane. Each 3D hit is assigned specific new Hough-specific X and Z coordinates to be processed correctly. For all three planes, the Z coordinate is set to the z position of the hit. The new X coordinate is set to be the x

position of the hit for the X-plane since X-plane wires are parallel to X-axis, y coordinate for all these hits is zero. However, U and V plane wires have ±30 degrees angle with X-axis. Thus, the new X coordinate is calculated as a square root of the sum of squares for x and y coordinates of these hits. The (r,θ) histogram parameters are chosen in a way that each bin in r represents 1mm and each bin in θ represents 1 degree to accommodate detector resolution. Moreover, since the position resolution in the detector is about 3 mm in X and Y (due to the spacing between wires), the adjacent bins for each hit are filled as well. To be a line in XZ, the bin in (r,θ) histogram should have a value more than 4. Knowing r and θ, the line equation can be reconstructed:

$$z = x \times \frac{-sin\theta}{cos\theta} + \frac{r}{cos\theta} \tag{4.3}$$

Each found line is saved as a preliminary cluster with all hits within less than a 4mm window around it. One feature of Hough Transform that has to be taken into account is that it finds all hits corresponding to the line going through all detector's volume including the time of the whole TPC event. Thus, these preliminary clusters are divided into objects, separated by more than 50mm. These new objects are called clusters and have to contain at least 3 hits to be saved. The above algorithm is being repeated until all possible lines as well as clusters are found. Figures 4.7 and 4.8 represent the example of the miniCAPTAIN TPC event before and after the Clustering algorithm.

4.2.4 Path follow

The previous step of the reconstruction takes care only of very narrow linear objects. However, due to multiple scattering, long tracks can be curved (Fig 4.9). Figure 4.9 shows that the orange track-like cluster located between wires 241 and 250 and the navy track-like cluster located between wires 250 and 280 should be one cluster, but were split into two clusters because the track is bent. The reconstruction algorithm called Path Follow is designed to solve this problem. The algorithm uses clusters, provided from the previous step as well as hits, that did not fall into any cluster. For each cluster, starting from the longest one, a box at each end is drawn. Each box follows the direction of the cluster and has a length of 40mm and a width of 6.3mm. Then, the algorithm checks if there are unused hits or parts of other clusters inside these boxes. If there are several hits or clusters appear in the box, the closest to the initial cluster is chosen. If an unused hit is chosen it is added to the initial cluster which creates a new cluster with recalculated direction. On the other hand, if part of full other cluster got chosen only hits in the box are added to the initial cluster and subtracted from the chosen one. The initial cluster is recreated with additional hits while the chosen cluster

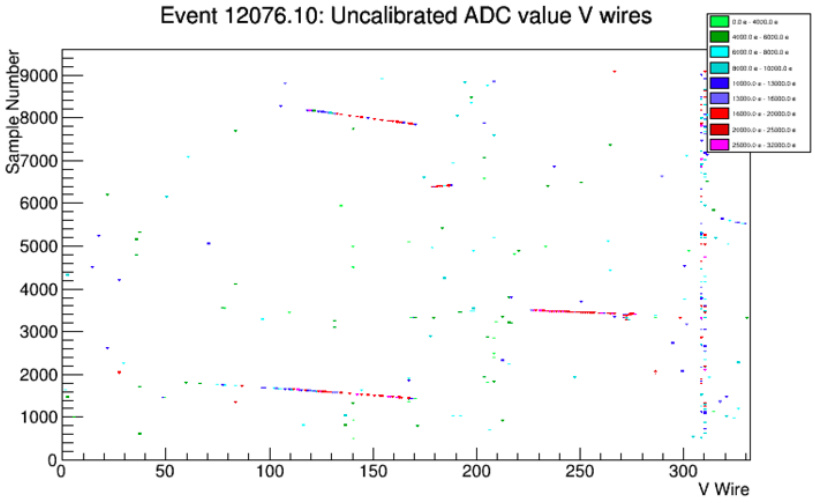

Figure 4.7: V-plane hits that came out of the HitTransfer algorithm. The X axis represents wire number, the Y axis shows timing information(each sample = 500ns), and the Z axis represents charge for each hit.

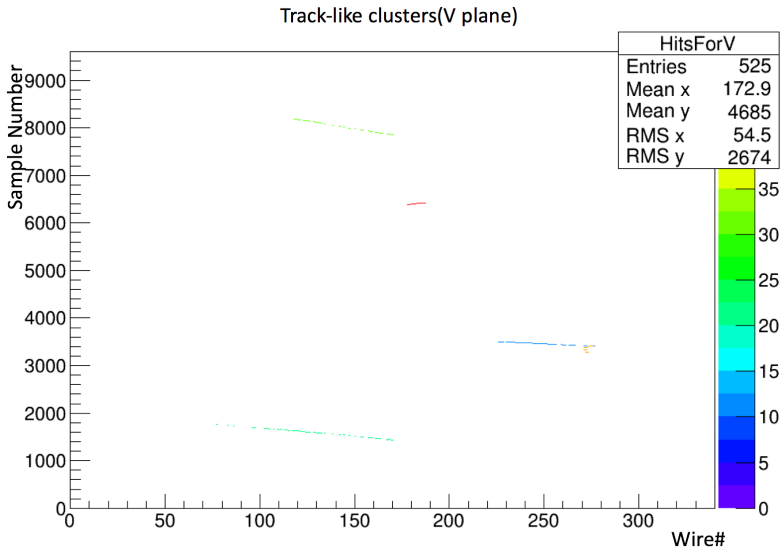

Figure 4.8: Clustered hits for a V-plane event from Fig 4.7. Each cluster shows as different color. The X axis represents wire number, the Y axis shows timing information(each sample = 500ns.)

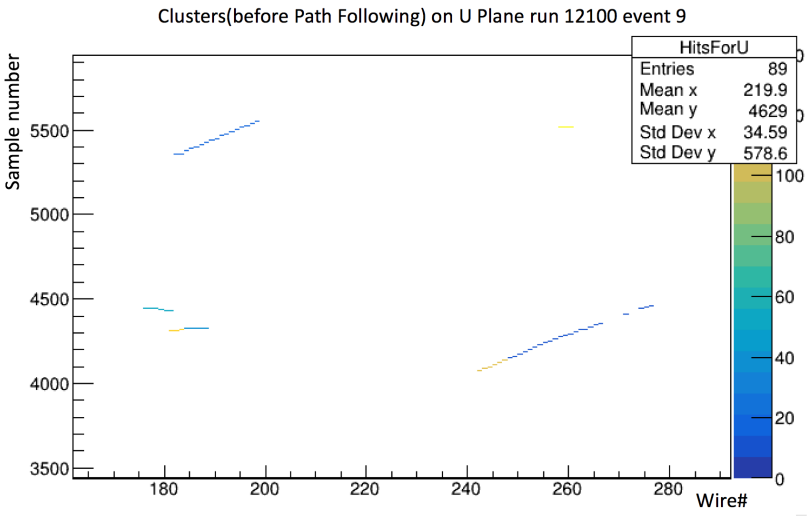

Figure 4.9: Found clusters before the Path Following algorithm was applied. Each cluster shows as a different color. The X axis represents wire number, the Y axis shows timing information(each sample = 500ns.

is recreated and stored without subtracted hits. The algorithm repeats itself until no clusters can be changed. As a result of the path following algorithm, the new final set of clusters is formed and ready for the track reconstruction (Fig 4.10).

4.2.5 Track reconstruction

Tracks are reconstructed using clusters formed on each plane. In order to reconstruct 3D tracks, clusters from 2D planes are combined based on time and space position in the detector. Prior to finding clusters that belong to tracks, obvious noise clusters are eliminated. Due to the specifics of the detector, it is extremely unlikely to detect a long vertical track. Thus, cut on the number of unique wires covered by the cluster is applied. On average, each hit in a cluster corresponds to one wire.

Cluster candidates for each track are found based on the Z position of starting and ending points of the cluster. The Z position represents the start and end time of the clusters because it is directly derived from the electron drift time in argon. It is impossible to know which end of the cluster is the beginning and which is the end. Thus, in order to compare two clusters, the algorithm takes one cluster's end as an arbitrary beginning of the cluster and calculates the distance between it and the arbitrarily chosen beginning of the other cluster. Then, the distance between the two other ends of these two clusters is added. This sum of two distances is

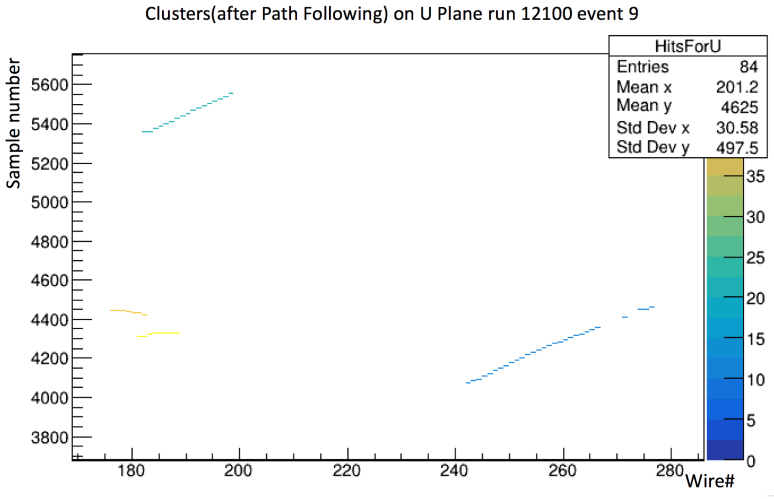

Figure 4.10: Found clusters after the Path Following algorithm. Each cluster shows as different color. The X axis represents wire number, the Y axis shows timing information(each sample = 500ns.

calculated for a different combination of beginning/endpoints for these clusters. The minimum value out of these two is considered to be the distance between clusters. For two clusters to be considered a track, the distance between them should be no more than 250mm. The cut is placed to prevent forming completely nonphysical tracks by connecting clusters from different beam pulses. If there are several clusters to obey these criteria, the closest two are selected. There are several ways to combine clusters. The most reliable way is when clusters from all 3 planes are present. Thus, the algorithm is looking for this option first (Fig 4.11).

Sometimes one plane can miss a cluster. Thus, when all possible combinations of 3 clusters are found, the algorithm starts searching for combinations of 2 clusters. The X plane clusters are the most reliable for position and charge due to the physics nature of this plane. Consequently, only the combinations between remaining X plane clusters and two other planes are searched. If there are no X plane clusters left or there is nothing on U and V planes to form a track, the algorithm stops.

After cluster combinations are found, they should be combined into a 3D object. The direction of a 3D object should be defined in order for 2D hits from clusters to be combined into 3D hits correctly and in the right order. For the case of 3 clusters, the direction is defined based on the XY position of the start/endpoints of each cluster. First, the direction of the X cluster is set to be in

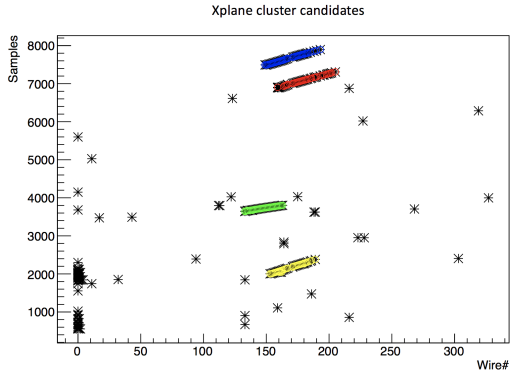

(a) X plane clusters

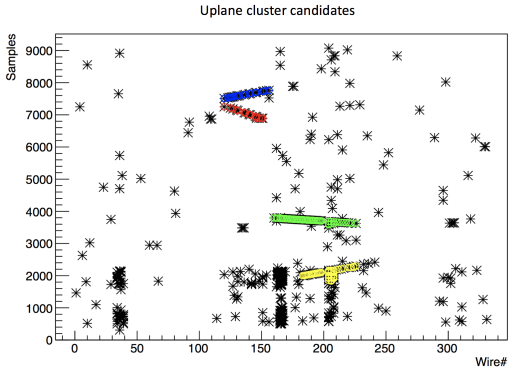

(b) U plane clusters

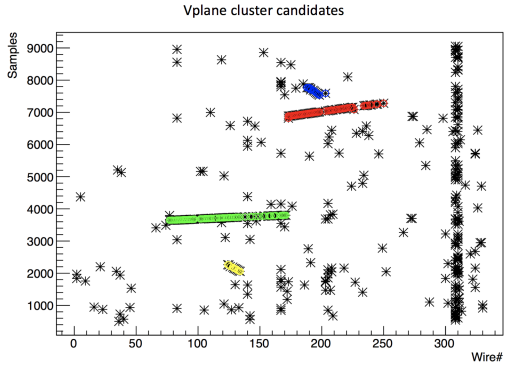

(c) V plane clusters

Figure 4.11: Clusters that are combined to be a track over all 3 wire planes. Each cluster combinations is shown as a different color. Black dots represent hits.The X axis represents wire number, the Y axis shows timing information(each sample = 500ns.

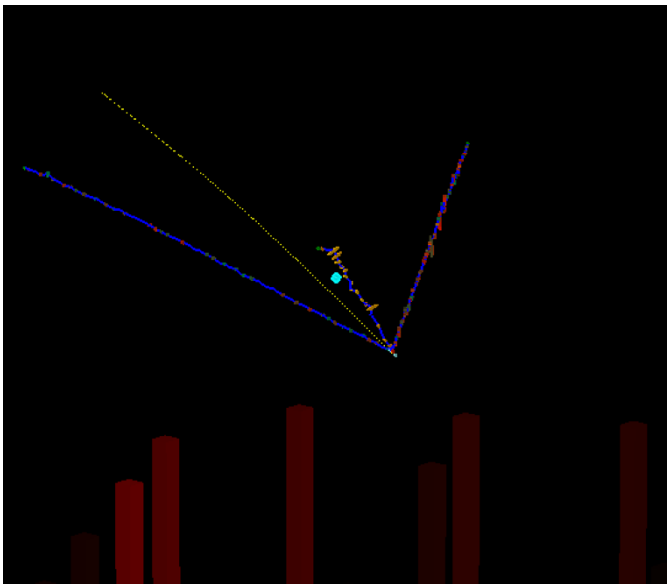

Figure 4.12: MC simulation of 600 MeV muon track starting in the middle of the detector(Yellow line). Blue lines represent clusters, reconstructed on each wire plane. Red dots are reconstructed Hits.

increasing wire numbering. Next, all possible combinations of start/end positions for U and V clusters are considered to compare to the X cluster. Distance between two arbitrary points from two different planes can be calculated using the equation:

$$d = -\frac{dx_2 \times (y_1 - y_2) + dy_2 \times x_2 - dy_2 \times x_1}{dx_2 \times dy_1 - dx_1 \times dy_2} \tag{4.4}$$

Where x_1,y_2 and x_2,y_2 are coordinates of these two points while dx_1,dy_1 and dx_2,dy_2 are axes of the considered planes. Since the X-plane direction is set as a default, the first point always belongs to the X plane with an axis along the global X-axis with dx_1=1 and dy_1=0. For U and V plane dx_2 and dy_2 vary because these two planes have ±30 degrees angle with global X-axis. Every 3 points from X, U, and V plane form a triangle. The side of this triangle can be calculated by taking the difference between XU and XV distances from equation 4.4. Choosing the smallest possible triangle defines start/end positions for U and V clusters corresponding to the default X cluster. For the case of just 2 clusters, this mechanism is not effective. The lack of 3rd point leads to an undefined triangle and as a result to the unconstrained cluster direction. Thus, in the case of two clusters, time(or Z coordinate) is used to define cluster directions. Clusters are simply combined starting from the earliest hit to the latest one.

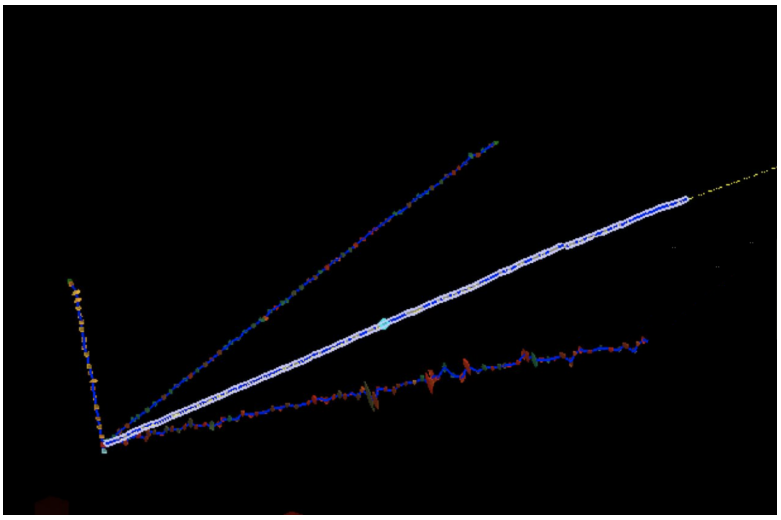

Figure 4.13: MC simulation of 600 MeV muon track starting in the middle of the detector(Yellow line). 3 Triangular Blue lines represent clusters, reconstructed on each wire plane. The 4th blue line in the middle is a 3D track reconstructed from combining 2D clusters. Red dots are reconstructed 3D hits.

The cluster's direction defined previously, orders hits from each cluster to be combined into proper 3D hits. Each cluster is divided into several parts which later will serve as track nodes. The number of nodes is equal to the number of unique wires in this cluster. However, if the number of wires is greater than 3 but less than 50, it is divided by 2. If it is greater than 50 and less than 100 it is divided by 5 and, finally, if the number of parts in the cluster is more than 100 it is divided by 10. This is done to reduce the number of hits in each node and to improve the precision of position reconstruction of the 3D hits. The number of track nodes is defined as the smallest number of parts from combining clusters. For each node, all possible combinations of 2D hits are used to create 3D hits (Fig 4.12,4.13).

For each 2D hit combination, the XY position of the 3D hit is calculated based on the average of the results of the equation 4.4. The Z position, time, and charge are defined as an average over combined 2D hits as well. Finally, all nodes are connected to form an object called the 3D track. The starting position of the track, as well as direction and the endpoint, are derived from the SIR (Sequential importance resampling) particle filter with forward/backward filtering. The charge deposited by the track is calculated as an average of sums of all charges of all unique 2D hits for each wire plane contributing to this track.

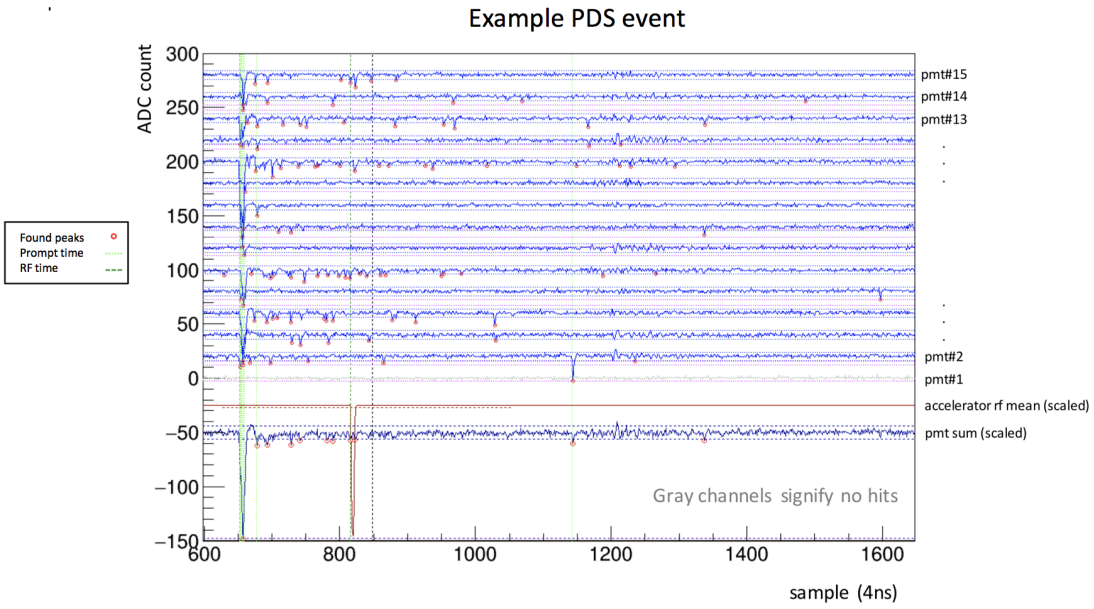

Figure 4.14: The example of PDS event. Red dots represent found peaks, the dark green line is a starting time of the RF pulse, and the light green line is a starting time of the coincidence with the most charge in it.

4.3 PDS reconstruction

The PDS system in mini-CAPTAIN consists of twenty-one instrumented PMT. PMTs are separated into three groups of seven PMTs each. Each group is assigned its own digitizer. All three store data independently. Thus, the PDS reconstruction goal is not only to find hits but also to synchronize data streams across these three digitizers.

Data reconstruction for the PDS system follows three major steps. First, all possible hits are found for each PMT as well as RF pulse, if it exists. Second, data from all 3 digitizes is aligned so PDS hits in each digitizer can be constructed in a single event. Finally, the coincidences between hits are found. These coincidences will later be used to distinguish neutron events.

4.3.1 Hit finding

Figure 4.14 shows the example of a PDS event. Each PDS event has data from 21 PMT and covers 8.4 μs in time spitted into 2100 samples with 4 ns width each. Down-going peaks represent possible hits that should be identified (Fig. 4.16). Each digitizer has an RF channel, that stores the information about the

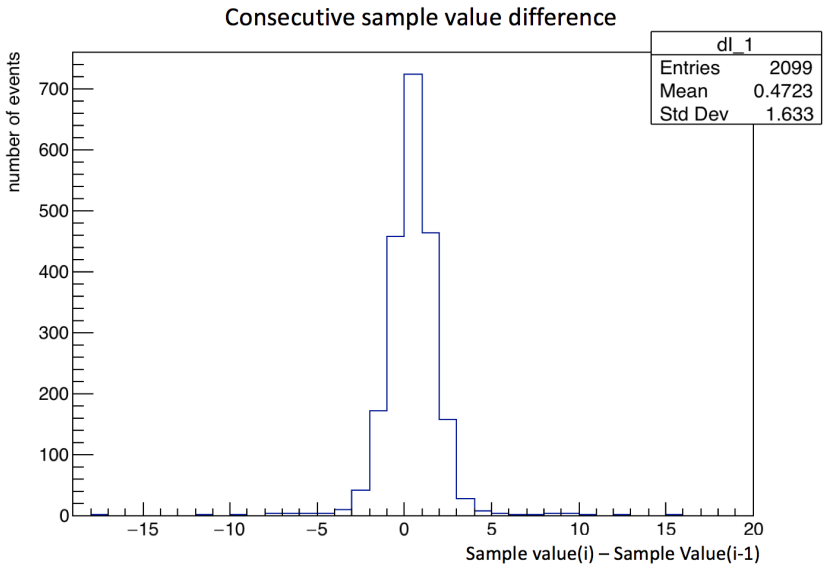

Figure 4.15: The example of the difference between sample values of two consecutive samples for one PMT in arbitrary PDS event.

RF pulse time and shape. The hit finding procedure is done separately for each PMT. First, the mean value for all samples in each PMT is calculated. This serves as a baseline for peak finding. Next, the average noise for the PMT is measured looking at fluctuation between two consecutive samples (Fig 4.15). The standard deviation of the distribution defines the noise RMS for the specific PMT.

The peak candidate is defined to be a sample with a value of more than 1.5 standard deviations above the mean PMT sample value.

The charge in PE(C_{PE}) for each peak is calculated using equation:

$$C_{PE} = \frac{S - M}{G}, \tag{4.5}$$

where S is the sample value of the peak, M is the mean sample value for the PMT, and G is the calibration gain constant for the PMT. The threshold to define a hit is chosen to be 0.4PE, which eliminates noise while selecting a single photo-electron signal.

Hits are constructed based on the found peaks. Figure 4.16 represents an arbitrary PMT peak, which is identified as a hit. First, well-separated peaks are considered. The starting time(sample) of the hit is set to be the first sample backward from the considered peak that falls into 1.5 standard deviations from the mean sample value for this PMT. The ending time of the hit is calculated in the same way but forward. Peak height for the hit is defined as its peak value

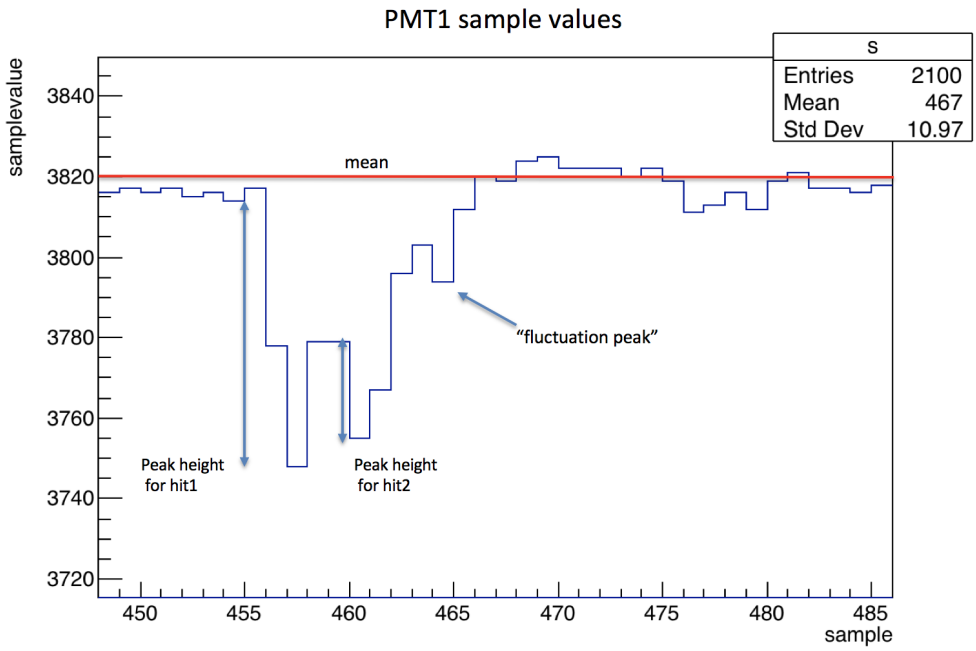

Figure 4.16: The example of finding hit parameters for two PDS hits close together.

minus sample value of the sample position 3 samples backward from the peak. The charge for the hit is calculated by dividing considered peak height by this PMT calibration gain constant. If two peaks are closer than 5 samples from one another, they might overlap. The starting time of the first hit is calculated the same way it is done for any separated hit. The ending time, as well as the starting time, of the second hit is set to be the middle sample between two considered peaks. The ending point of the second hit is calculated the same way as for the separate hit. Charge for the first hit is determined based on a peak height and PMT gain constant. However, the second hit peak height is set to be the difference between the peak sample value and the sample value of the starting point of this hit. Thus, the charge is equal to this new peak height divided by gain constant.

Each digitizer stores RF pulse information in a separate channel. The RF channel store the shape and time of the incoming RF pulse. The RF pulse finding is significantly more simple. For each PMT trigger, they count as RF pulse if there are samples in the RF channel with values more than 500 above the mean value for this channel.

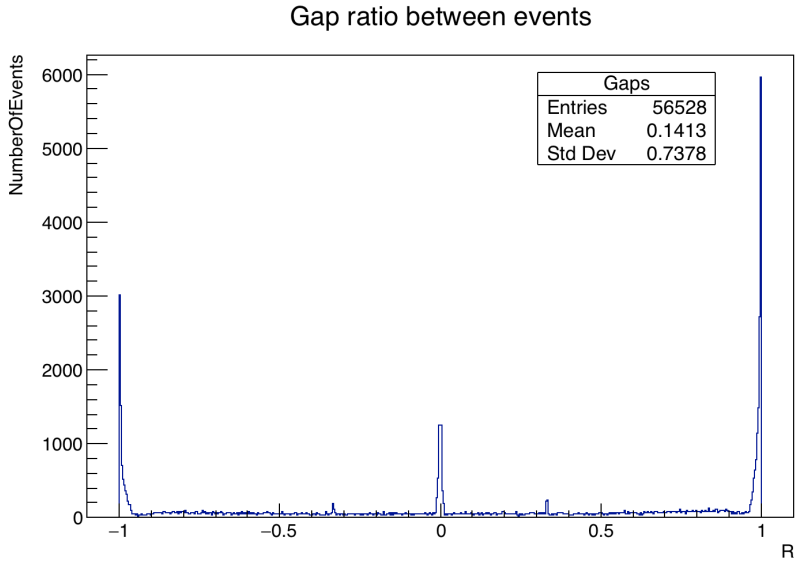

Figure 4.17: The ratio between two consecutive gaps across three digitizers before alignment

4.3.2 Digitizer alignment

All 3 digitizers are treated as separate data streams. Detailed data analysis showed that these data streams got desynchronized and duplicated in a few places. First, the duplicated data is found. If data repeats itself 2000 events in advance, it is marked as a duplicated and will not be considered during the synchronization process. In total there are 2000 duplicated events for each of the digitizers 0 and 1, and 3854 duplicated events for digitizer 2. The synchronization can be performed only using data samples without duplicates.

The purpose of the synchronization algorithm is to assign for each event in the digitizer 0 events from digitizers 1 and 2. The algorithm is based on a comparison of time gaps between events across 3 data streams. First, these gaps are calculated for each digitizer separately. Two gaps are calculated for each event: one is called "first", which is from previous event digitizer time, and another one called "last", from the next event digitizer time. Using these gaps, digitizers 1 and 2 are compared to digitizer 0. The comparison between two gaps is done based on the ratio:

$$R = \frac{g_i - g_j}{g_i + g_j}, \tag{4.6}$$

where $g_{i,j}$ are widths of the compared gaps. Figure 4.17 shows that three data streams are seriously desynchronized according to gap analysis. However, some

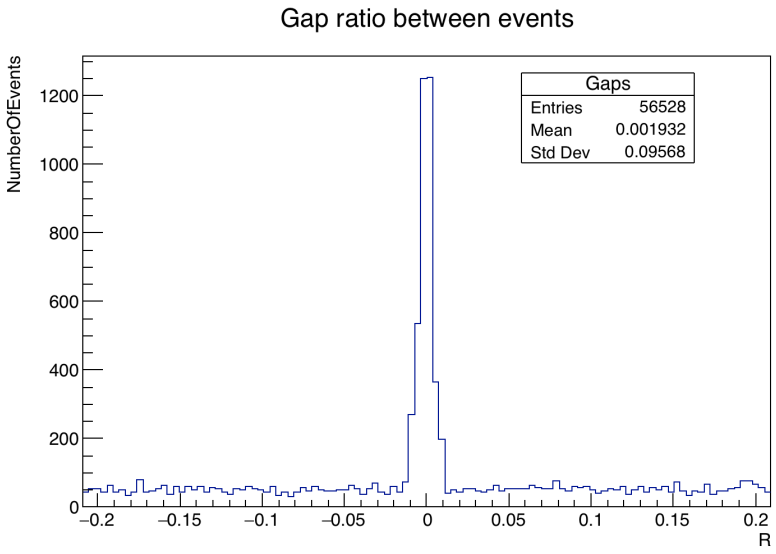

Figure 4.18: The ratio between two consecutive gaps across three digitizers before alignment(zoomed at aligned region)

data parts are in sync, which is represented as a peak around zero. By zooming in this peak the cut on two gaps being aligned is defined (Fig. 4.18). If the ratio is less than 0.02, the corresponding digitizer 0 event is marked as aligned and receives a matching event number from the other digitizer. It is always the case that the last gap indicates the start of misalignment. Thus, if the ratio for the last gap is greater than 0.02, the corresponding event in the digitizer 0 receives null entry for alignment with the other digitizer. Then, the next event in the digitizer 0 is compared to 15 next gaps from the other digitizer. The ratio for the first gap can vary if digitizers are missing events. Consequently, again only the ratio for the last gaps is checked to be less than 0.02. If an aligned event is found, 16 next gaps are checked and 15 of them must align to exclude random alignment. The alignment in this particular case means the ratio for first gaps should be less than 0.05 and for last gaps should be less than 0.01. If all the above criteria are met, the new aligned event for the considered digitizer 0 event is found, if not, it is marked as not aligned.

After the synchronization is done, several small adjustments are made to make it exact. First, events 14, 15, and 16 from the digitizer 0 are marked as not aligned with the digitizer 2. This is done because, despite the right gap alignment, these events in digitizer 2 received no data. The RF pulses comparison between aligned digitizer events shows that 0.13%(484) events have mismatched RF pulses (Fig 4.19). These events are marked as bad as well, due to the data quality.

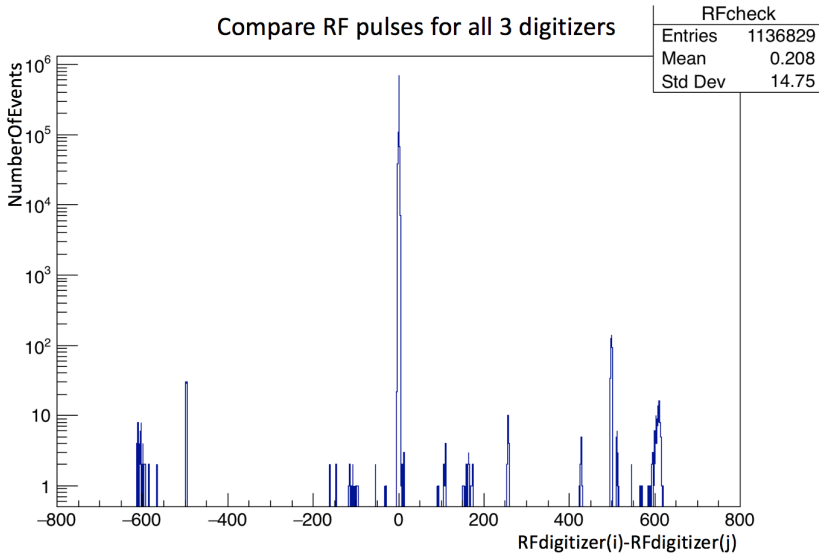

Figure 4.19: The difference between starting time of the RF puls of digitizer i and j, where i,j can be 0,1 or 2.

4.3.3 Coincidence finding

The aligned PDS events from the previous step are used to find coincidence hits between PMTs. For each aligned event, all found hits are taken and the new time is assigned to them. If the RF pulse is present in this event, the new time is set to be the difference between the hit's peak time and RF pulse starting time for the corresponding digitizer. If there is no RF pulse, the time is set to be just the time of the peak for each hit. Then, all hits are sorted based on a new time low to high. Blocks of hits separated by less than 4 samples(16 ns) are found from this data stream. The coincidence is called at least two PMTs having hits in this 16ns time windows.

4.3.4 Neutron energy measurement

Found coincidences can be used to define gamma peak as well as neutron energy spectrum. For each coincidence, the time difference of the earliest peak and corresponding RF pulse is plotted (Fig 4.20). Figure 4.20 shows clear evidence of the gamma peak. The gamma peak was fitted with a Gaussian fit. The exact position of the gamma peak from the fit is -629.8±0.1 with σ=4.431±0.068.

Knowing the gamma peak position neutron energy spectrum can be calculated. For each coincidence, the RF pulse time is subtracted from all hit times. The hit

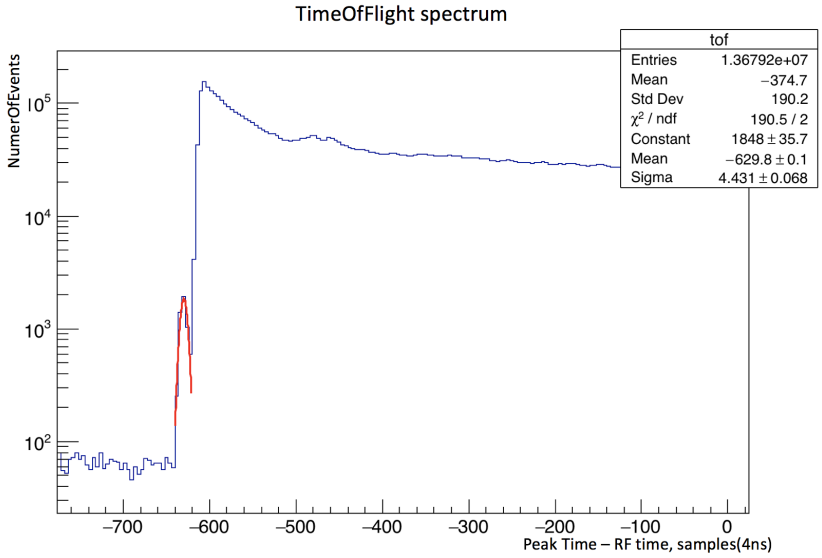

Figure 4.20: Time of flight spectrum for all found coincidences in aligned PDS events. The Gaussian fit represents gamma peak.

with a maximum difference is used to calculate neutron energy for this coincidence. First, this new time(dt) is corrected for gamma peak(t_{gamma}) and flight path between the detector and the target, which is L=23.2 meters:

$$t = (dt - t_{gamma}) \times 10^{-9} + \frac{L}{c}, \tag{4.7}$$

where c is speed of light. Corrected time can be used to calculate the momentum of the neutron:

$$p = \frac{m \times L}{\sqrt{t^2 \times c^2 - L^2}}. \tag{4.8}$$

where m=939.6 MeV is neutron mass. Then, the neutron momentum can be converted into neutron kinetic energy:

$$E = \sqrt{p^2 + m^2} - m. \tag{4.9}$$

This technique is called the time of flight(TOF) technique and is used to assign energy for each neutron, registered in the detector.

4.3.5 PDS-TPC alignment

TPC reconstruction does not provide the correct Z position of the track inside the detector. The Z position from TPC is the time from the beginning of the beam macropulse converted to distance using electron drift speed in liquid argon. Thus, it can even exceed the detector size. The exact Z position for each track is found using PDS data. Thus, each TPC event should be assigned with. a corresponding one or several PDS events. Since the beam is coming every 200 μs, it was decided to assign to it all PDS events that are in ± 100 μs time range around considered TPC event. Detailed data investigation of both, TPC and PDS, revealed two alignment features. First, all TPC events are shifted by 200 μs compared to PDS. Second, two times per miniCAPTAIN neutron run PDS wrote an extra event, which shifted times of the following events. However, after fixing these two misalignments features the normal order between PDS and TPC is achieved.

Chapter 5

Data Study

The TPC and PDS event reconstruction, described in the previous chapter, is directly applied to the data collected from miniCAPTAIN specific low-intensity beam. Although it can work with a high-intensity beam as well, the extra tuning for multiple parameters is required. Thus, this work is focused exclusively on low-intensity data. The reconstruction validation is done using reconstructed neutron data to reproduce the neutron beam inside the miniCAPTAIN. The other data studies described in this chapter, such as electron lifetime, wire charge collection, and wire efficiency measurements, are performed using reconstructed cosmic muons.

5.1 Beam Spot Study

The reconstruction validation is done by identifying the beam spot inside the detector using the reconstructed track information. The detector was turned to the beam in such a way that the beam enters it at the 4th quadrant with nearly maximum possible X coordinate (and wire number) and close to zero but negative Y. Thus, the starting position of all tracks is set to be the one with the highest X coordinate. First, the beam spot in time (Z coordinate) is found. Prior to PDS adjustment, the Z coordinate is the time multiplied by electron drift time in liquid argon. The Z coordinate can exceed the size of the detector since detector time for data collection covers whole beam macropulse and beyond. The plot of the Z coordinate of all reconstructed tracks inside all TPC events from the low-intensity beam is shown in figure 5.1.

Figure 5.1 shows the three expected peaks between -1000mm and 0mm, which represents three expected micropulses in a given macropulse. These peaks are separated by approximately 199 μs(or 318.4 mm), which reproduces the provided beam structure. Two peaks at 1000 and 2000 are noise signatures on wires that

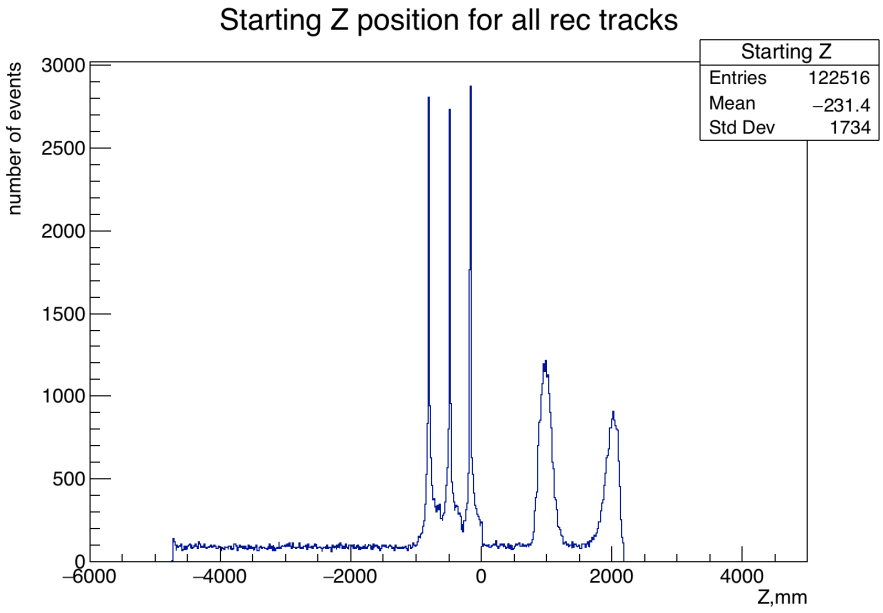

Figure 5.1: The starting Z position of all reconstructed tracks. The starting position is defined as one with maximum X coordinate.

are sometimes identified as a track and happen outside of the macropulse.

Next, the PDS correction is applied to the data between -1000 and 0 mm, since it corresponds to a macropulse. The PDS corrections try to identify the best Z position for each track in the event such that they all are corrected inside the detector. However, for events with more than one reconstructed track, the ambiguity in choosing the right PDS correction exists. In order to eliminate it, only events with one reconstructed track is used in the analysis. The summary of the initial and corrected Z position of these tracks is shown in figure 5.2.

The events with one reconstructed track and proper PDS correction can be used to study the shape of the beam. The detector is divided into 5 equal slices in X between -450 and 450 mm. For each slice, the starting Z position of tracks inside of it is plotted. Next, the peak of each distribution is fitted with a Gaussian function to determine the approximate mean value as well as the spread of the beam. Also, the data far from the peak is fitted with a straight line ($y = \alpha \times x + \beta$) to define the background. Each slice with Gaussian and background fits is shown in figure 5.6. The result of all five background fits is shown in table 5.1.

The summary of all mean values and sigma values from the Gaussian fits is shown in figures 5.4(a) and 5.4(b), respectively. The shift of the first bin down on figures 5.4(a) is about 3mm, which is small in comparison with the analysis region

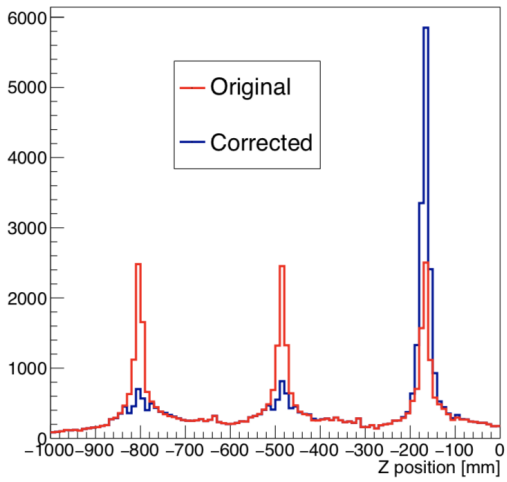

Figure 5.2: The Z position of a track. The red line is the original Z position, while the blue line is the Z position corrected using PDS information. Tracks below -300 mm correspond to neutrons from second and third micropulse that have no proper PDS correction.

of 50mm around the beam spot. Thus, it does not provide significant systematic effect. Given distributions are fitted with a strait line to define the Z properties of the beam. The results of the linear fit with interpolated values at the front of the detector are presented in table 5.2.

Next, the XY beam position can be defined. Starting XY points for tracks that got properly adjusted using PDS information are shown in figure 5.3. Figure 5.3 shows that reconstructed tracks reproduce the hexagonal shape of the detector. From the reconstruction, the beam enters at 4th quadrant and has a slight angle with the X-axis as expected. The same slices in X, as was described above, are used to study the beam evolution vs the depth in the detector. Each slice with Gaussian and background fits is shown in figure 5.7. The result of all five background fits is shown in table 5.3.

The summary of all mean values and sigma values from the Gaussian fits is shown in figures 5.5(a) and 5.5(b) respectively. Both distributions are fitted with a strait line to define the Y properties of the beam. The results of the linear fit with interpolated values at the front of the detector are presented in table 5.4.

As a result, the beam travels parallel to the XY plane and with about 6.7° degrees angle to the X-axis. The beam center propagation is best described by the line:

$$y = -0.1188 \times x - 54.9894, z = -165mm \tag{5.1}$$

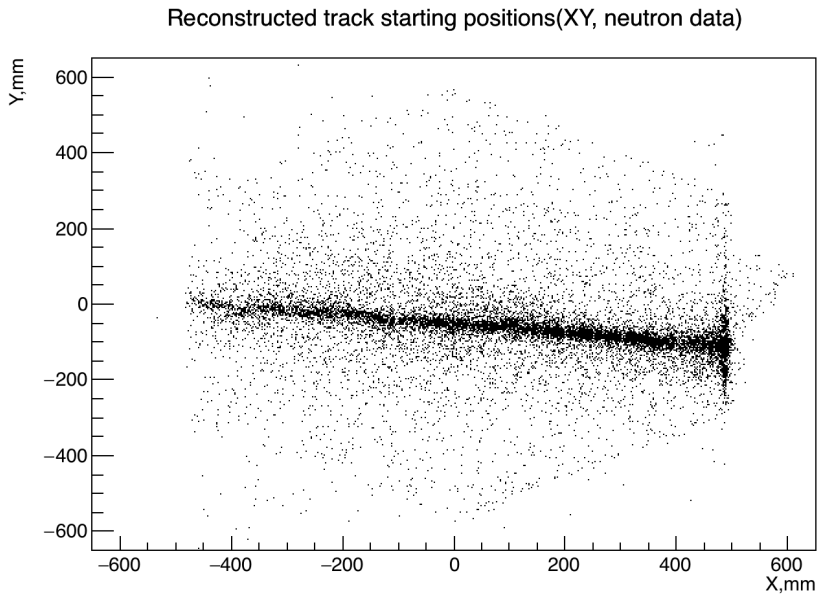

Figure 5.3: Starting XY position of the reconstructed tracks inside the beam time. The beam time is defined between -1000 and 0 on Figure 14. Transparent red line represent linear fit for the beam.

Slice	α	β
Slice X=[270,450]mm	8.3±0.4	-0.0046±0.002
Slice X=[90,270]mm	11.8±0.5	-0.0094±0.0026
Slice X=[-90,90]mm	13.83±0.5	-0.0116±0.0028
Slice X=[-270,-90]mm	12.3±0.5	-0.016±0.0025
Slice X=[-450,-270]mm	7.1±0.38	-0.0057±0.002

Table 5.1: The linear background fit for Z position distribution for five slices in X. The line form is: $y = \alpha \times x + \beta$.

Fit	α	β
Mean value fit	-0.0026±0.00014	-165.5±3.7
Sigma value fit	-0.00012±0.00005	7.7±0.14

Table 5.2: The results of linear fits of mean values and sigmas of Gaussian data peaks in Z for all five slices in X. The line form is: $y = \alpha \times x + \beta$.

Slice	α	β
Slice X=[270,450]mm	5.4±0.26	-0.0045±0.0008
Slice X=[90,270]mm	4.67±0.21	-0.00084±0.0005
Slice X=[-90,90]mm	6.1±0.22	-0.00066±0.00058
Slice X=[-270,-90]mm	4.5±0.2	-0.0023±0.0005
Slice X=[-450,-270]mm	3.9±0.21	-0.0011±0.00064

Table 5.3: The linear background fit for Y position distribution for five slices in X. The line form is: $y = \alpha \times x + \beta$.

Fit	α	β
Mean value fit	-0.1188±0.00014	-54.98±6.67
Sigma value fit	-0.0064±0.0015	13.97±0.39

Table 5.4: The results of linear fits of mean values and sigmas of Gaussian data peaks in Z for all five slices in X. The line form is: $y = \alpha \times x + \beta$.

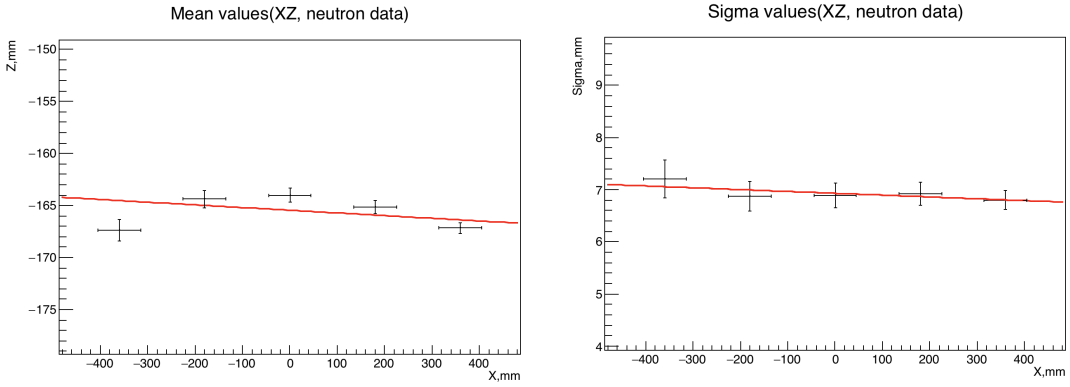

(a) Mean values (b) Sigma values

Figure 5.4: Mean values(a) and sigma values(b) of Gaussian data peaks in Z for all five slices in X.

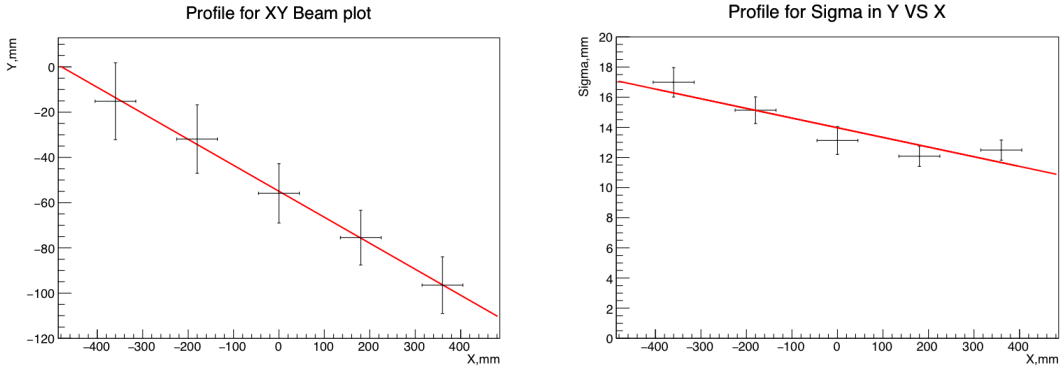

(a) Mean values (b) Sigma values

Figure 5.5: Mean values(a) and sigma values(b) of Gaussian data peaks in Y for all five slices in X.

5.2 Electron Life Time

The electron lifetime study was done using a sample of long cosmic muon tracks. A muon track is defined as a track with a length in the Z-axis more than 30 cm, which means it crosses the whole detector. The maximum length is 32 cm. The muon track also should be outside of the beam spot, which means it has a reconstructed Z position of less than -1320mm or greater than 320mm. This study is done without PDS time information. That means there is no way of defining the right time between tracks. However, assuming all tracks crossed the whole detector the problem can be solved. Each track is around 32 cm long which is 200 μs based on the electron drift time in liquid argon. Thus, the time of the starting point of all tracks can be set to zero and the time of the following hits is calculated relative to that zero value. Next, the analysis is done for 3 wire planes separately. The deposited charge is calculated for each time as a sum of charges of unique 2D hits in a given time frame. Charges are corrected based on the angle between them and wire planes.

	X plane	U plane	V plane
Electron Life Time	73.41± 0.59 μs	72.23± 0.53 μs	87.91± 0.82 μs
Normalization factor	9.97 ± 1.13×10^{-2}	10.61 ± 1.14×10^{-2}	10.04 ±1.15×10^{-2}

Table 5.5: Electron Life Time fit results

The logarithm of the deposited charge is plotted against the time and shown in figure 5.8 for all 3 wire planes. Figure 5.8 shows profiles of these plots as well as a linear fit. Electron lifetime derived from the profile linear fit for each wire plane separately is given in Table 5.5. The achieved electron lifetime is long enough for tracks to drift to the collection plane.

5.3 Wire efficiency and collected charge

The detailed investigation of data revealed that many tracks have several wire gaps in them. The gaps are identified using 3D tracks that are fully reconstructed. Each 3D track is split into its 2D constituents and in each 2D cluster pairs of consecutive hits are studied.

Consecutive hits might not be a consecutive wires. Following this logic, for each wire the number of times this wire is missing(N_{disapp}) from a track and the number of times the wire is appeared as intended(N_{app}) are counted. The inefficiency($\bar{\epsilon}$) of the wire can be calculated using the equation:

$$\bar{\epsilon} = \frac{N_{disapp}}{N_{app} + N_{disapp}}. \tag{5.2}$$

Figure 5.9 represents inefficiency for each wire for all 3 wire planes based on the average charge of neighboring hits.

Regions with inefficient or not instrumented wires appear as yellow bands (eg. wire numbers 290-310 on U-plane). The inefficiency of the low charge is also expected. However, there are regions in the detector where wires are instrumented that are inefficient for high charge hits. Mostly inefficient wires are concentrated between wire number 180 and 330 of the X plane and between 0 and 150 wire numbers of the U and V planes, which corresponds to the upstream part of the detector. The inefficient wires are eliminated from the data reconstruction as well as from any MC miniCAPTAIN simulation.

The total charge collected by each wire was studied on tracks from long cosmic muons. The same sample of muons as described in section 5.2 is used. Figure 5.10 shows the collected charge for each wire for all three wire planes. Blank regions represent wires either turned off during construction or eliminated as inefficient. The remaining wires show a smooth picture of collected charge across all 3 planes and provide a calibration of the wire energy response for miniCAPTAIN electronic simulation.

The study shows that the mean collected charge is uniform across the detector. Moreover, the collected charge from MIP is way above threshold (3 on the presented figure 5.10). Hit finding efficiency is good across all wires with more dead wires in the upstream part of the detector.

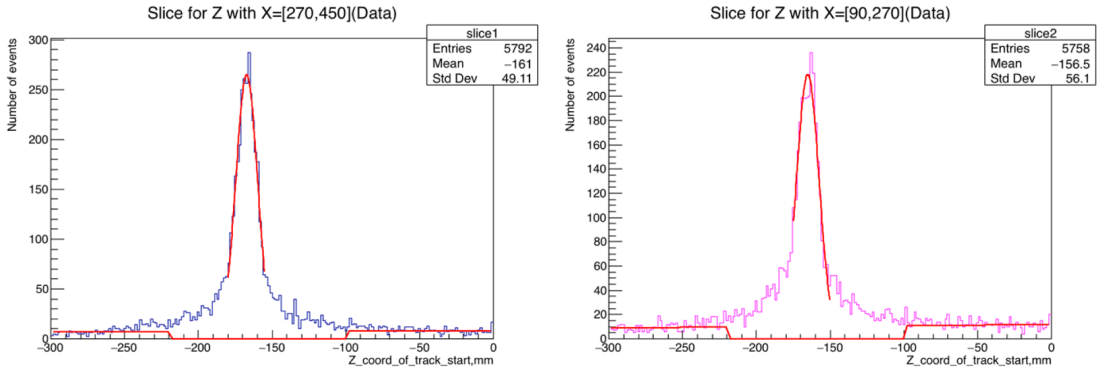

(a) Slice X=[270,450]mm

(b) Slice X=[90,270]mm

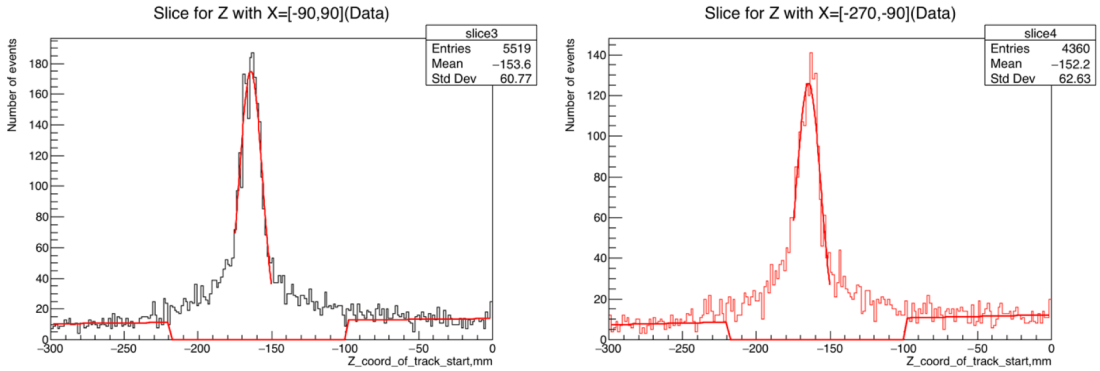

(c) Slice X=[-90,90]mm

(d) Slice X=[-270,-90]mm

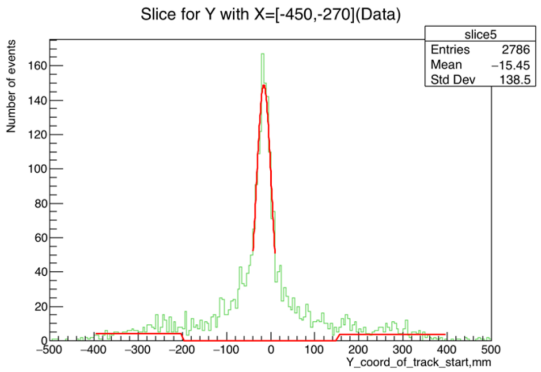

(e) Slice X=[-450,-270]mm

Figure 5.6: The evolution of starting positions (Z coordinate) of reconstructed tracks.

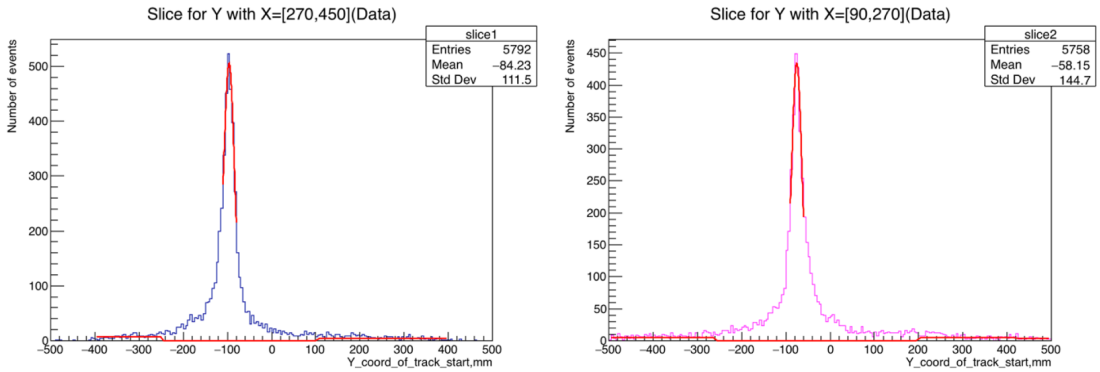

(a) Slice X=[270,450]mm

(b) Slice X=[90,270]mm

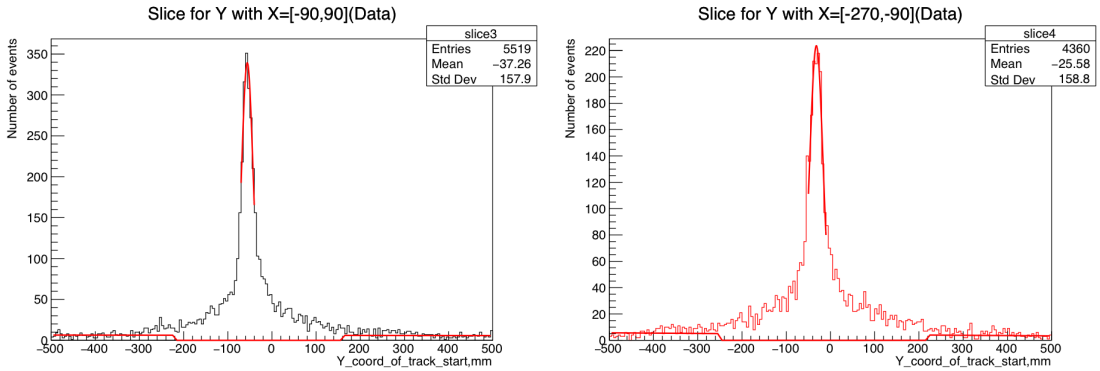

(c) Slice X=[-90,90]mm

(d) Slice X=[-270,-90]mm

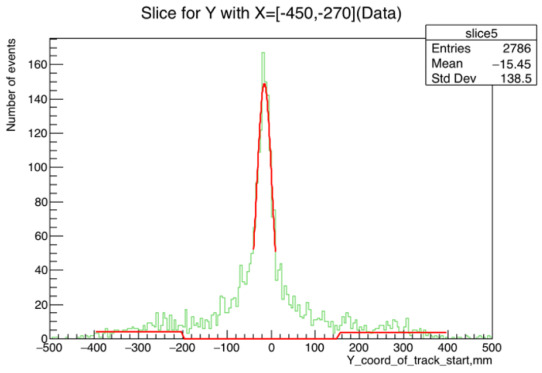

(e) Slice X=[-450,-270]mm

Figure 5.7: The evolution of starting positions (Y coordinates) of reconstructed tracks.

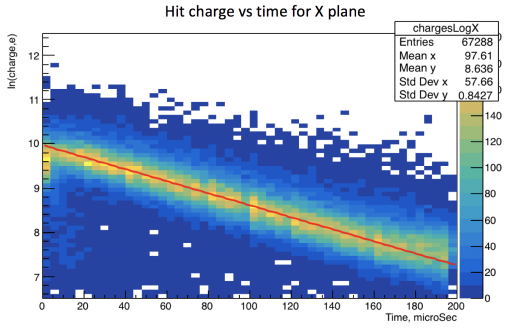

(a) X plane hit charge vs time

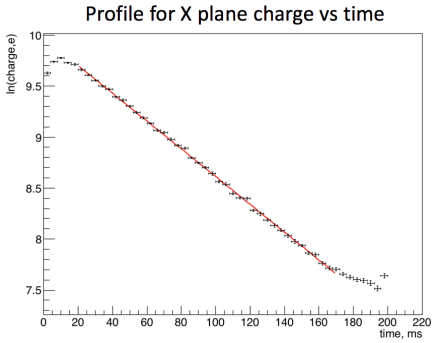

(b) profile for Fig 5.8a

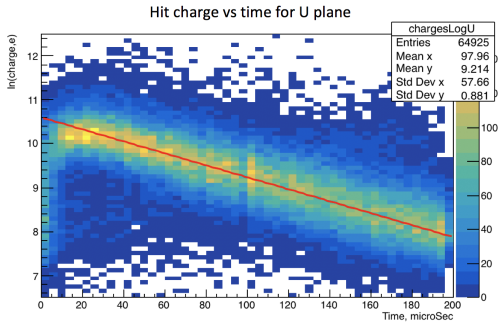

(c) U plane hit charge vs time

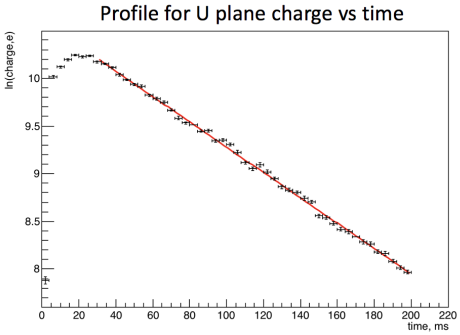

(d) profile for Fig 5.8c

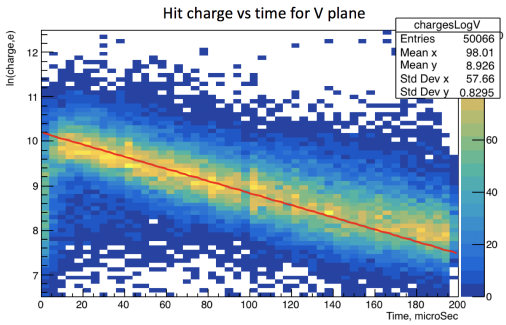

(e) V plane hit charge vs time

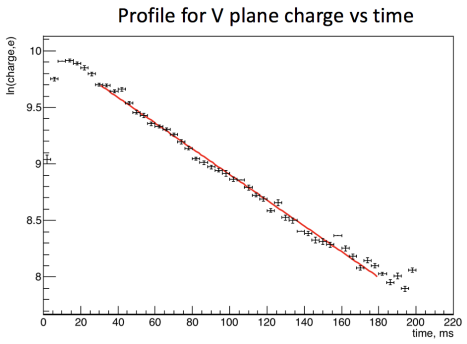

(f) profile for Fig 5.8e

Figure 5.8: On the left is the logarithm of the deposited charge vs time for selected long muon tracks(a,c,e). On the right are profiles of the electron lifetime plots(b,d,f).

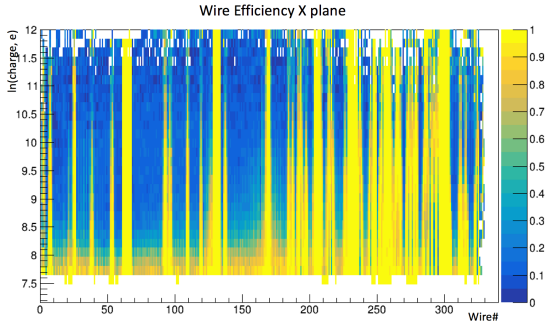

(a) X plane wire inefficiency

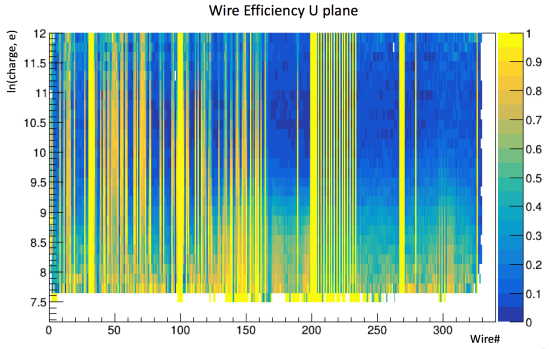

(b) U plane wire inefficiency

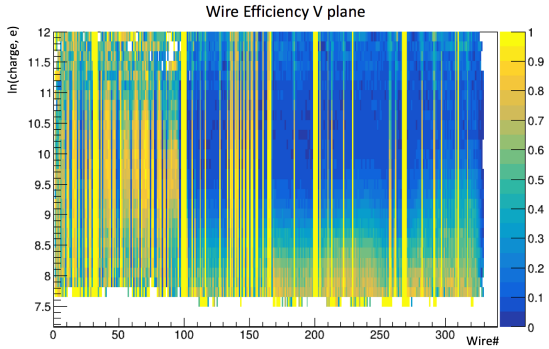

(c) V plane wire inefficiency

Figure 5.9: Inefficiency for each wire for all 3 wire planes based on an average charge of neighboring hits. Yellow color specter represent the most inefficient wires, while blue stands for efficient wires.

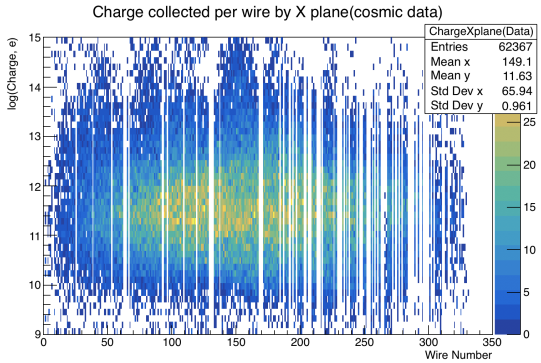

(a) X plane collected charge

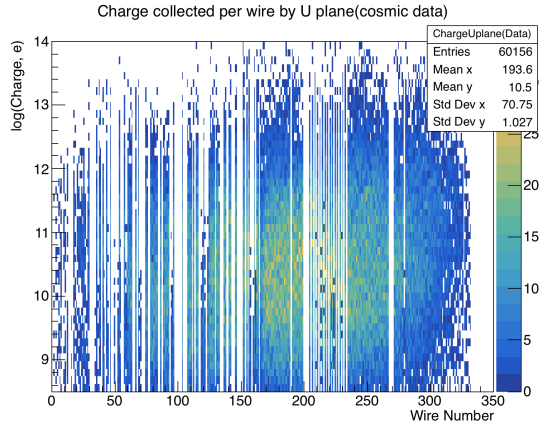

(b) U plane collected charge

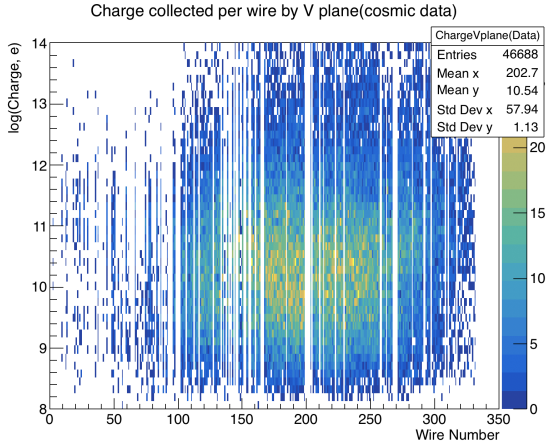

(c) V plane collected charge

Figure 5.10: Collected charge for each wire for all 3 wire planes. Blank regions represent wires either turned off during construction or eliminated as inefficient.

Chapter 6

Monte Carlo(MC) simulation

The Monte Carlo simulation for miniCAPTAIN is done based on $GEANT\_4.10.3$ with $QGSP\_BERT$ physics list[53]. It is used to study the performance of the reconstruction as well as to do Data/MC fit to get neutron cross section measurement. The chapter describes the MC and Data comparison to understand if the simulation can be used to perform Data/MC fit and study systematic uncertainties.

6.1 Simulation description

The detector volume and the energy depositions by the charged particles are simulated using $GEANT\_4.10.3$ with $QGSP\_BERT$ physics list[53]. The NEST [54] model is used to properly calculate the number of thermal electrons and scintillation photons. Ionization electrons are allowed to drift toward wire planes via applied magnetic field. The drift is described as an exponential model based on the electron lifetime observed in the experiment. The small diffusion is introduced to the electron velocity and path.

The Shockley-Ramo theorem is used to estimate induced current in wires after the cloud of ionization electrons is reaching wire planes. It calculates the "weighting field", E_i, of a wire by holding it at +1V and treating the rest of the wires as grounded. The induced current is given as:

$$i = -q \times v_d \times E_i \tag{6.1}$$

where v_d if drifting speed of electrons in argon. The method is chosen to model the approximate di/dt on the wire. The magnitude of the current induced by a drifting electron is separately fixed to get the proper normalization. The shape of di/dt is modeled by assuming the electron drifted directly to the wire. The time of arrival is modeled assuming the electron followed a "right angle" path.

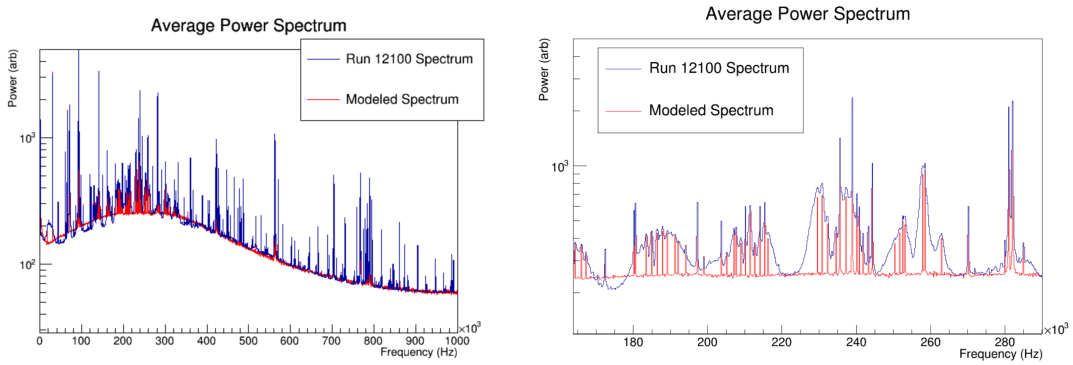

(a) Full frequency spectrum (b) Zoom between 170 kHz and 290 kHz

Figure 6.1: The comparison between the simulated noise and noise observed in one of the neutron runs. The blue line is noise observed in the experiment, the red line is simulated noise.

The chosen model is sufficient for the experiment since it does not perform any measurement based on precise energy deposition calculations. All wires are used in a binary fashion, which means they are having a signal or not based on the amount of charge received. The threshold choice is based on the data and the uncertainty in its choice is handled by systematic.

The noise is modeled in two steps. First, the continuum noise is modeled as $1/f^{\alpha}$ plus Gaussian noise that is shorted through an impedance. The "impedance" is modified to better fit observed data. Second, the non-continuum(discreet) noise is simulated. This type of noise has relatively narrow bandwidth around a set of specific frequencies. Position and amplitude of the noise peaks are identified from the data. Thus, it is modeled using random phase and amplitude at the peak frequency. The amplitude is chosen using a Gaussian with the mean power of the peak and the phase is derived from a uniform distribution. The phase between the different frequencies is not correlated. Each noise peak is modeled as being at a single frequency. The result of the noise modeling is presented in figure 6.1.

6.2 Collected Charge Study

First, the study of the collected charge for each wire is repeated for the MC simulation. The charge collection study for the data described in the previous chapter was done with cosmic muons. Thus, several mono-energetic 8GeV muon samples are simulated. The simulations are done for each plane separately. In each simulation, muons are travailing along the axis, perpendicular to the wires of the particular wire plane. Muons started above the detector outside its volume and

traveled through the entire detector in Z. Figure 6.2 demonstrate the reconstructed charge for three wire planes. In the case of U and V plane muon tracks are not crossing all the wires. This is happening due to the hexagonal shape of the detector. However, all wires are simulated equally. Thus, the covered region is representative of the entire wire plane.

The collected charge from the cosmic muons in date (fig. 5.10) can be compared against the collected charge from simulated muons 6.2. The summary of mean charge and spread are listed in table 6.1.

Parameter	Data Value, log(#e)	MC Value, log(#e)
Mean Charge Xplane	11.63	10.21
Charge Spread Xplane	0.91	0.34
Mean Charge Uplane	10.5	10.8
Charge Spread Uplane	1.0	0.36
Mean Charge Vplane	10.54	10.91
Charge Spread Vplane	1.13	0.42

Table 6.1: The comparison between mean collected charge and charge spread across the detector for reconstructed cosmic muons in Data and simulated 8GeV muons in MC. Values are given as a log of number of collected electrons.

The comparison shows that MC produces a slightly lower charge intake for the X plane due to lower gain values, but produces proper mean charge for U and V planes. The overall collected charge from MIP is above the threshold for the MC (3 on fig. 6.2).On the other hand, the charge spread in MC is much lower than shown in the Data. The next section describes the adjustment done to the MC simulation to accommodate for this discrepancy.

6.3 Wire Efficiency MC/Data

The charge collection study showed that the spread in collected charge for the MC is much lower than observed in Data. This can lead to higher hit finding efficiency in MC than in Data. However, to perform Data/MC fit and study systematic uncertainties properly, the efficiency of the detector should be roughly the same. It is especially important in a beam region of the detector, where the analysis takes place.

In order to make efficiencies for MC and Data match across the detector, the wire inefficiency correction is introduced in MC. First, all wires are simulated with 100% efficiency, which means that if the collected charge is above a certain threshold, a hit is found with certainty. Initially, the threshold was set to 3000

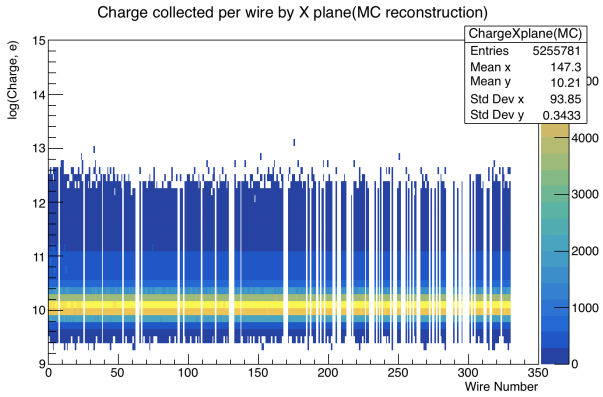

(a) X plane collected charge

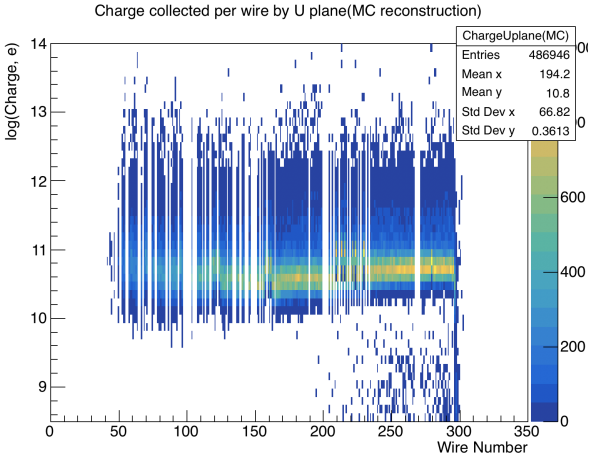

(b) U plane collected charge

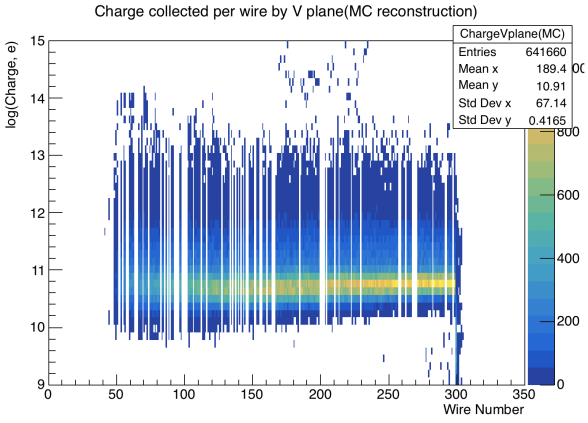

(c) V plane collected charge

Figure 6.2: The collected charge for each wire for all 3 wire planes. Blank regions represent wires turned off to represent the data.

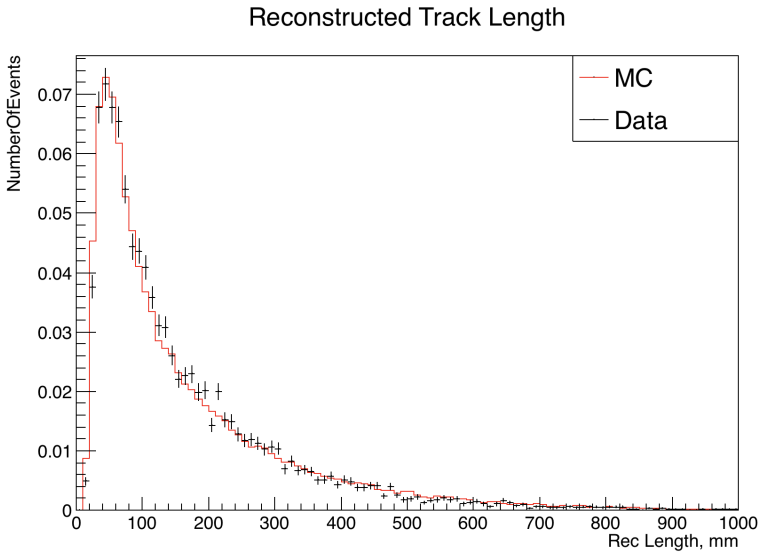

Figure 6.3: Track length distribution for reconstructed Data and MC tracks from neutron interactions.

electrons for all wire planes in MC to mimic the same cut in Data. The inefficiency in simulation is introduced by making the threshold vary slightly around its initial value. The cut for each wire hit is chosen as a random variable chosen from the Gaussian distribution around the fixed thresholds for a given plane. The fixed threshold for each lane as well as sigma of the distribution was adjusted in a way to make efficiencies in simulation match data observations (Tab. 6.2).

Plane	Threshold, #e	Sigma, %×threshold
Xplane	3000	12.5
Uplane	2500	85
Vplane	2900	75

Table 6.2: The optimized values of the charge threshold and sigma for the simulation. The threshold is given in the number of electrons, and sigma is a percentage of the threshold.

The next step is to compare the efficiency of the simulation with the data. A new set of muons is simulated for each wire plane and compared against the cosmic muons from the data. The efficiency is calculated the same way for MC and Data in two different categories.

First, the efficiency vs drift time is checked. Efficiency is calculated for each

plane separately. For each reconstructed track, all pairs of consecutive 2D hits are chosen. If the pair has a gap, the hit that supposes to be in this gap counts as "disappeared"(N_{disapp}). Hits that are present in the track receive the appearance mark(N_{app}). The drift time for present hits is calculated based on reconstructed time, while for missing hits it is inherited from the two neighboring registered hits.

$$\bar{\epsilon} = \frac{N_{app}}{N_{app} + N_{disapp}}. \tag{6.2}$$

The result of the detector efficiency vs drift time is shown in figure 6.7 for all 3 wire planes. The beam region for the analysis is between 78.75 μs and 128.75 μs. The Analysis also covers side bins, that extend the beam region up to 53.75 μs on the left and 153.75 μs on the right. The study shows that the MC simulations properly reproduces the hit finding efficiency vs drift time in the beam region.

The other important study is the efficiency vs the depth inside the detector as the neutron beam travels along the X-axis(wire number). This efficiency is calculated only for the 50mm diameter region around the beam. As previously discussed, each reconstructed track is split into 3 wire plane projections for the analysis. For each projection, two registered hits are identified. One of these hits stands right above the beam window in time, while the other one is below. Next, based on a time difference between these two-wire hits, the time is predicted for all wire hits in between. Hits whose predicted time falls into the beam window contribute to the total appearance for corresponding wires and serve as a denominator in the efficiency calculation 6.3, N_{tot}. The appeared wires in the beam window matching the prediction is defined from reconstructed hits and serves as a numerator in the efficiency equation 6.3, N_{app}.

$$\epsilon = \frac{N_{app}}{N_{tot}} \tag{6.3}$$

Figure 6.6 shows the result of the wire efficiency for each wire plane around the beam. Wires in the MC are simulated with the same efficiency of about 97% around the beam spot and shown as a red line. The result shows that wire efficiency does not change across the detector with an exception of several wires, thus providing the uniform response needed for cross section calculation. Moreover, the simulation efficiency is in close agreement with the data.

6.3.1 Track Length study MC/DATA

In order to see if MC simulates detector response and overall neutron beam properly, the study of reconstructed track length distribution is performed. The nar-

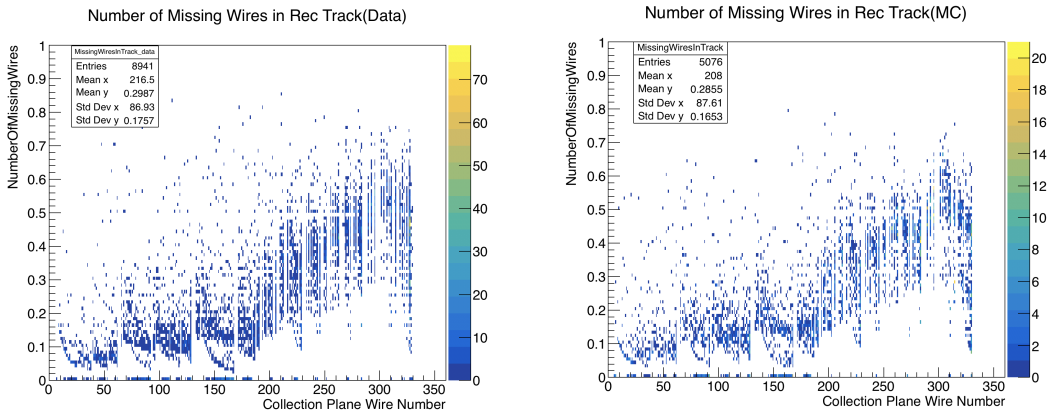

(a) Data result (b) MC result

Figure 6.4: Number of X wires missing in reconstructed track for the Data (a) and MC (b) vs collection plane wire number.

row neutron beam is simulated. The simulated beam has one neutron per event with energies spread linearly between 100 and 800 MeV. It starts just outside the miniCAPTAIN detector and follows the experimental beam direction described in the previous chapter. The diameter of the simulated beam is chosen to be 50mm with no angular spread. The data set for the Data is narrowed to only tracks participating in published analysis with extension to full detector volume. This includes the following applied cuts:

- Only tracks withing 25mm(radius) from the beam are considered;
- There should be only one track inside a defined region per event;
- Tracks with length less than 15mm are not considered.

Fig. 6.3 shows track length distribution for reconstructed Data and MC tracks. The study shows that the simulation properly reproduces track lengths through the entire detector volume in X near the beam.

6.3.2 Track Gap study MC/DATA

Each wire plane in mini-CAPTAIN detector has regions with several consecutive uninstrumented wires and some wires with lower hit finding efficiency. These regions have significant influence over the track reconstruction. MC simulation should reproduce the effects seen in the data. In order to prove that, the number of missing wires in reconstructed track in Data and MC is studied as well as the maximum gap appeared in reconstructed tracks. The data set for this study was

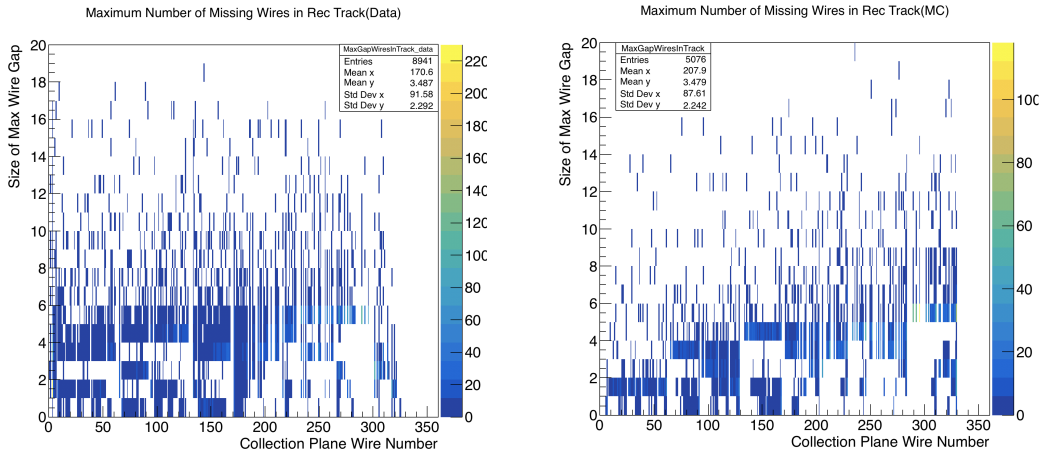

(a) Data result (b) MC result

Figure 6.5: Maximum number of wires missing per reconstructed track for the Data (a) and MC (b) vs collection plane wire number.

chosen to be the one that obeyed the analysis criteria described in section 6.3.1. The MC simulation for this analysis is the same as described in section 6.3.1 as well.

Fig. 6.4 represents the number of X wires missing in the reconstructed track for the Data (a) and MC (b) vs collection plane wire number. Fig. 6.5 shows the maximum number of wires missing per reconstructed track for the Data (a) and MC (b) vs collection plane wire number. The Data and MC are in good agreement. Thus, MC simulates detector features caused by missing wires in the Data properly.

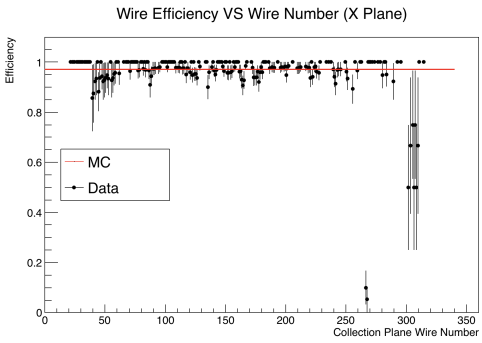

(a) X plane wire efficiency

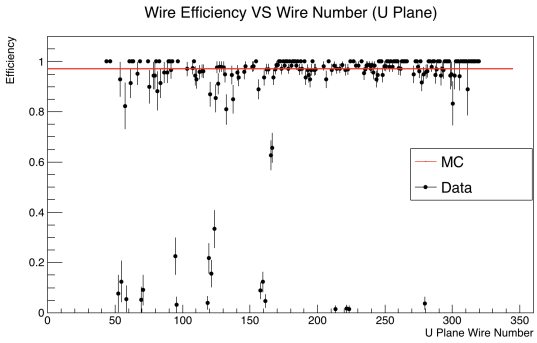

(b) U plane wire efficiency

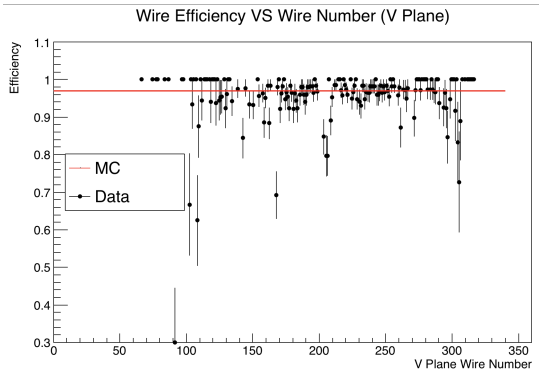

(c) V plane wire efficiency

Figure 6.6: Efficiency for each wire for all 3 wire planes in 25mm region around the beam. The black dots represent data, and the Red line is MC efficiency.

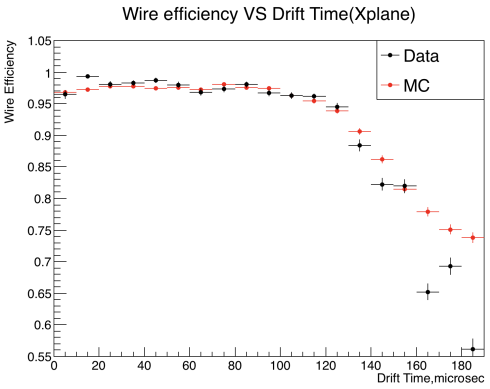

(a) X plane detector efficiency vs drift time

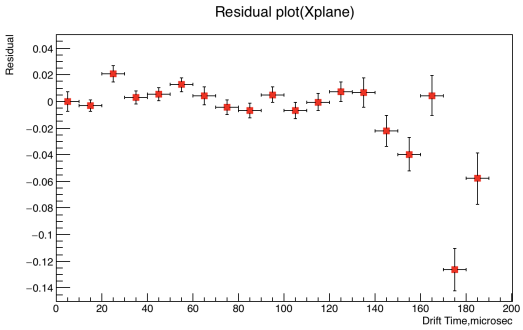

(b) Residual for X plane efficiency

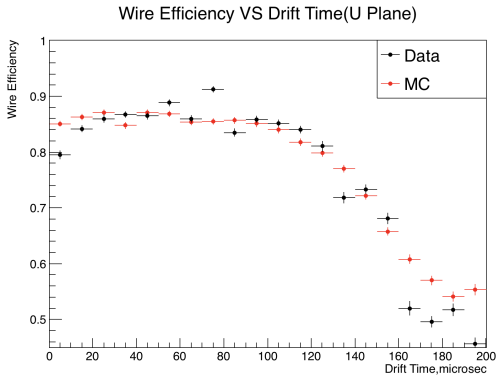

(c) U plane detector efficiency vs drift time

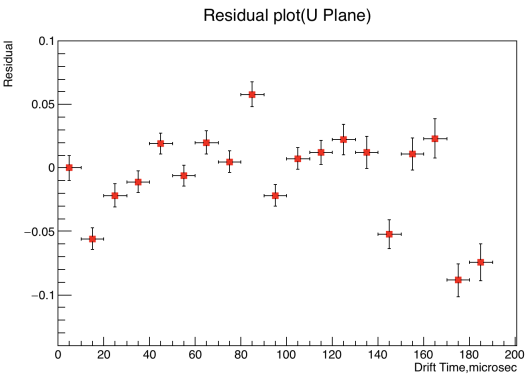

(d) Residual for U plane efficiency

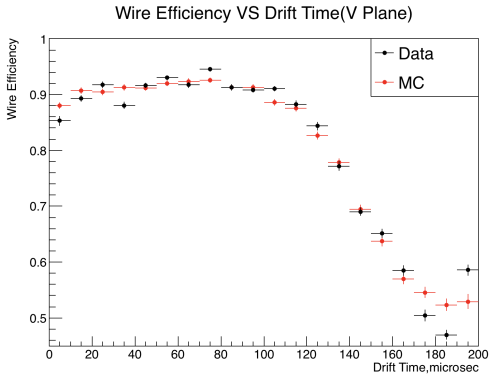

(e) V plane detector efficiency vs drift time

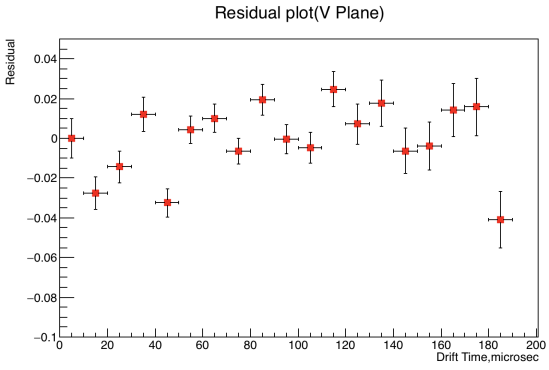

(f) Residual for V plane efficiency

Figure 6.7: On the left is the detector efficiency vs drift time for X, U, and V wire planes(a,c,e). On the right are residual plots comparing Data and MC efficiencies(b,d,f).

Chapter 7

Neutron Cross Section Measurement

This chapter is focused on the main method of measuring the neutron cross section used by CAPTAIN collaboration. The first half of the chapter describes the method itself as well as its validity for the given experiment. The second half demonstrates the result of the method application to collected neutron data. The result is published in PRL July 2019[7]. Thus, this chapter is mostly influenced by the material in the paper.

7.1 Measurement Method

The primary hypothesis for the analysis is that the total neutron-argon cross section can be derived from the neutron beam attenuation in the detector. Neutrons interact with argon while traveling through the medium. Thus, neutron flux decreases as a function of the depth in the detector. The attenuation process shown in figure 7.1 is described by the equation:

$$\frac{dN_B}{dx} = -T\sigma_T N_B \rightarrow N_B(x) = N_0 e^{-T\sigma_T x} \tag{7.1}$$

where σ_T is the total neutron cross section, x is the distance neutron traveled in the medium, and $T = \rho_{LAr} \times N_{Avogadro}/m_{Ar}$ is the nuclear density of liquid argon. The nuclear density is a constant in the experiment and equal $2.11 \times 10^{22} cm^{-3}$ $[T = (1.3973 g/cm^3 \times 6.022 \times 10^{23} n/mol)/39.948 g/mol]$.

For the method to work, the event topology that corresponds to a fraction of the total cross section should be chosen. Next, the measurement of the change of the rate of this topology vs the depth inside the detector should be measured. This yields a measurement of the total cross section if the fraction of the total

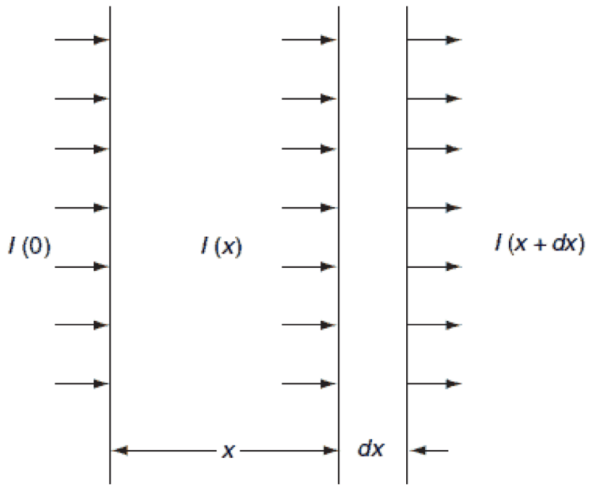

Figure 7.1: The neutron beam attenuation process.

cross section that results in the selected topology does not change as a function of depth. This statement is satisfied under several extra assumptions that should be discussed:

- The target volume must be uniform;
- The incoming flux must be monochromatic;
- The particles in the beam do not rescatter within the selection region;
- The additional neutrons from the background are negligible

These conditions are met in the analysis.

First, the uniformity of the target volume is satisfied by the construction feature of the miniCAPTAIN detector. The liquid argon target purity is an essential requirement of the experiment to detect drift electrons from the ionized particles. In chapter 5 section 5.2 the study of the electron lifetime was presented. It shows that the experiment achieved sufficient argon purity to perform the desired measurement. The detector charge collection uniformity was studied using cosmic muons as well. In details this study is presented in chapter 5 section 5.3. Based on this study, the uniformity of the mean collected charge across the detector is established. Moreover, it shows that hit finding efficiency is good across all wires with the collected charge from MIP being far above the threshold. It also points out that there are more dead wires in the upstream part of the detector. The effect of this behavior is demonstrated in figure 7.2. The MC simulation of the

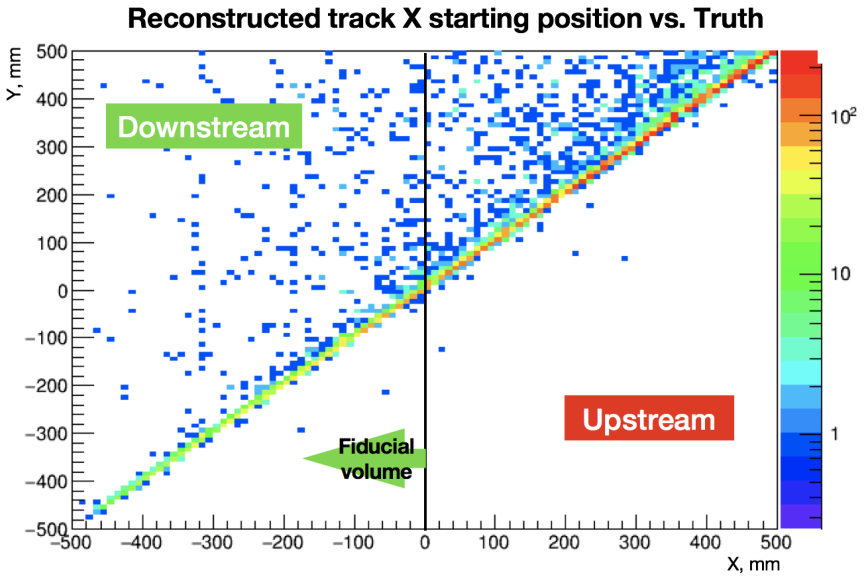

Figure 7.2: The Reconstructed X coordinate of starting pistons of proton tracks vs its true values (MC simulation).

proton beam was designed in a way to cover all energies between 500 MeV and 800 MeV. The proton beam starts just outside the detector volume and travels parallel to the XY plane and 45° to the X-axis. Figure 7.2 shows the reconstructed starting X position of the proton tracks vs its true values. It shows that true and reconstructed values are in agreement across all detector volume. However, the discrepancy is higher in the Upstream part[0mm-450mm on X-axis] due to many dead wires. Thus, only tracks starting in the Downstream part[-450mm-0mm on X-axis] are considered in the analysis.

Second, the neutron flux from the LANSCE is not uniform as it can be seen in Figure 3.7. However, the energy of each incoming neutron is known based on the Time Of Flight. Thus, in the analysis, the energy bins for the measurement are chosen in a way that allows to sustain fairly uniform neutron flux in each of them.

Third, the rescattering of the particles back into the analysis beam region is eliminated in two steps. The rescattering can occur due to multiple elastic/inelastic scattering. In order to reduce this behavior to a minimum the very narrow selection region around the beam is chosen in the analysis. Also, only events with one reconstructed track in this selection region are considered for the measurement. Data analysis shows that there are only 5% of the events that have multiple reconstructed tracks in the chosen area. These events are excluded from

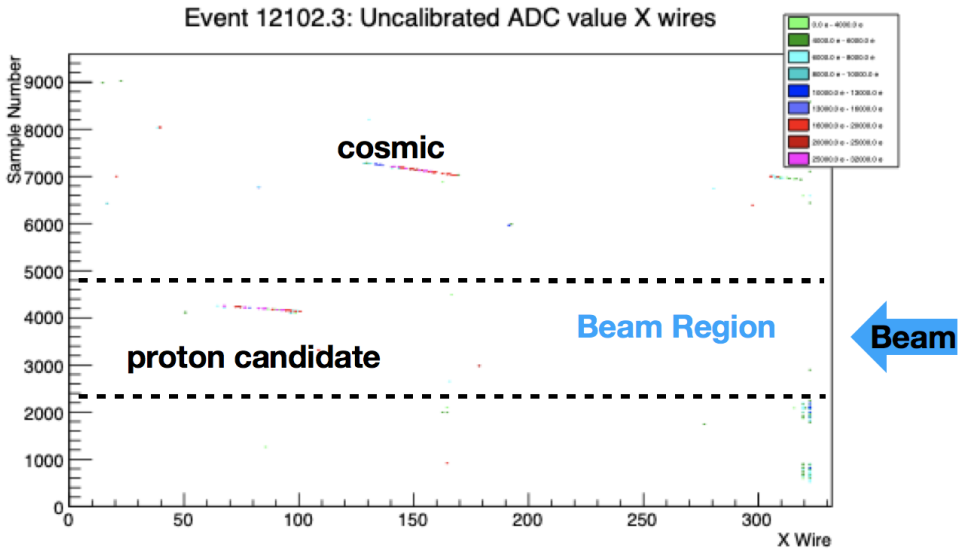

Figure 7.3: X-plane hits from the event that obeys all selection criteria in the analysis. The X axis represents wire number, Y axis shows timing information(each sample = 500ns), and Z axis represents charge for each hit.

the analysis.

Finally, the background neutrons are eliminated as a result of the experiment design. All TPC events considered for the measurement associated with a PDS event, which is triggered by the RF signal. Since the RF signal comes directly from the target, this requirement mitigates the external neutron background.

7.2 Selection topology

The event topology for the analysis is chosen based on the requirements for the measurement method to be valid as well as detector resolutions. The selected TPC event obeys the following criteria:

1. TPC event should have at least one PDS hit associated with it;
2. The energy of incoming neutron reconstructed from PDS should be above 100MeV;
3. The event has only one reconstructed track in a signal region;
4. Reconstructed track length is more than 15 mm;

5. Reconstructed tracks start in a small region (54mm diameter) around the beam.

6. Reconstructed tracks start inside the fiducial volume (downstream part of the detector);

The measurement is done for six narrow energy bins where the total cross section and partial cross sections are not expected to vary significantly.

The total number of events with at least one reconstructed track from 4.5 hours of low-intensity neutron beam at the WNR is 115880. Then, cuts 1 through 5 are applied, and the number of events is reduced to 9911. The last cut, that chooses the events with tracks only starting in the downstream part of the detector, reduces the number of events to 2418. These events make the final data set for the neutron cross section measurement.

7.3 Neutron cross section

The described beam attenuation measurement method is applied to the final data set. The distribution of the starting position of all tracks along the beam is fitted with an exponential function. Each energy bin is fitted separately. Figure 7.5 shows exponential fits done for each of six neutron energy bins. The method of choosing binning in X for the fit is based on the available statistics and in detail described in [55]. Thus, the number of degrees of freedom vary for different energy bins.

Energy range, [MeV]	Cross section, [b]	$\chi^2/NDOF$	Number of tracks
100-199	0.49±0.34	1.48/3	264
199-296	0.88±0.16	11.81/7	536
296-369	0.89±0.26	4.739/5	329
369-481	0.94±0.20	8.262/6	413
481-674	1.20±0.18	5.713/6	624
674-900	0.83±0.32	0.1323/4	252

Table 7.1: Neutron cross section in bins of kinetic energy. The χ^2 per degrees of freedom is presented, as well as the total number of tracks used for the fit in each bin. The exact functional form used for the fits is $f(x) = c_1 e^{-c2x}$[7]

The cross section is extracted from the exponential fits using the equation 7.1. The final neutron cross section measurement is represented in figure 7.4. Figure 7.4 shows values obtained from GEANT and FLUKA [53, 56] simulation as well.

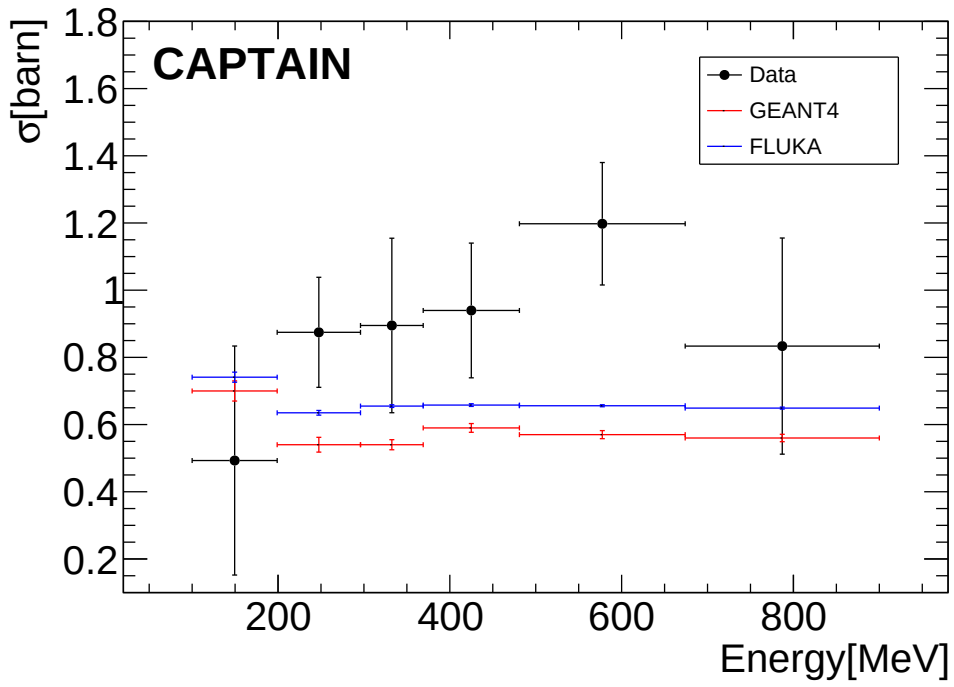

Figure 7.4: Neutron cross section measurement as a function of neutron kinetic energy. Black dots are data points, Read and blue are values obtained from simulation. The simulation cross sections are obtained from exponential fits to the distribution of tracks as a function of depth into the detector. The errors bars correspond only to the statistical uncertainty of the fits, for both data and simulation[7].

The simulation cross sections are obtained from exponential fits to the distribution of tracks as a function of depth into the detector. This is summarised in detail in table 7.1. All but the last fits have p values in an acceptable range. The energy bin that corresponds to the highest neutron energy has a large p value equal to 0.988. However, it is still consistent with the exponential fit assumption given the limited statistics and the number of trials available.

7.4 Systematic effects

The measurement method is designed in a way that it does not depend on beam flux normalization. The only significant property of the flux is its relative intensities at different depths into the detector. However, there are multiple system-

atic uncertainties considered for this measurement. First, it is the distortion of the reconstructed starting position. This can potentially lead to event migration between the bins and impact the exponential fit. Second, it is the systematic uncertainties associated with track angle and inability of the reconstruction to distinguish between the front and endpoint of the reconstructed track. Finally, the effect of choosing only single track events is considered.

The uncertainty from the starting position reconstruction distortion is studied using proton simulation. The simulation is the same that was used to study the detector response uniformity and described in section 7.1. The protons with energies between 50 and 800 MeV are simulated and the reconstructed position of proton tracks is compared against their true values. The comparison is shown in figure 7.2. The study suggests that the track position reconstruction resolution for the miniCAPTAIN is less than 20mm in the downstream part of the detector [-400,0]mm. The size of the bins in X for the exponential fits vary between 40 and 45 mm in the measurement(7.5). Thus, the small in comparison to bin size, fluctuation of the starting position can lead to the migration of no more than 4% of the tracks. This effect is considered negligible if compared to the statistical uncertainty in the measurement.

The other two potential systematic effects are track angle and choice of front/back position of the track. Track parallel to wire planes can make just a few hits. Since the reconstruction algorithms consider tracks with at least 4 hits, some tracks can be missed. The proton simulation mimicking the beam direction and angular distribution are used to study this effect. However, the reconstruction of the true proton tracks shows that angular distribution observed in the experiment is not affected by this detector feature.

The reconstruction is designed in a way that it can not distinguish the front and back position of the track. Thus, in the experiment, all reconstructed tracks are assumed to have a starting position at the lowest X(closest to the beam entry point into the detector). This causes the ambiguity between upward and backward moving particles. However, the particles created from neutron interaction are expected to follow forward direction along the beam. Using the same proton simulation, the upper limit on this systematic uncertainty is set at a few percent and can be neglected if compared to the statistical uncertainty in the measurement.

The dominant systematic uncertainty in the experiment is caused by multi-track events. The effect is studied using MC simulation of the neutron beam. For each energy bin used in the analysis, 500000 neutrons are simulated with constant energy equal to the mean bin energy. The neutron beam has a diameter of 1mm, starts just outside of the detector, and follows the X-axis. Then, two cross section measurements are performed using the exponential hypothesis and

only true information. The data set for the first measurement obeys the following criteria:

- First charged track in the event born from initial neutron interaction is selected;
- Track starts 50mm(diameter) region around the beam;
- Tracks with a length above 15mm are considered (to mimic reconstruction response).

The data set for the second measurement includes all criteria from the first data set but excludes events with multiple tracks in the selection region around the beam. The selection algorithm checks if there are no other charged tracks with a length above 15mm in the 25mm region around the beam. The second track counts as a separate track if it is at least 10mm apart from the first track(since reconstruction would count close tracks as one). For both groups, the starting X position of the first charged track is plotted for the downstream part of the detector(to mimic fiducial volume in the experiment) and fitted with the exponent. The cross sections extracted from the exponential fits with relative errors are summarised in table 7.2. Moreover, the presented data shows the increase in multi-track events with energy.

The suggested systematic uncertainty is calculated as cross section difference between two data sets with a combined error of both measurements. Moreover, the ratio of events with one track and multiple tracks that is shown in table 7.2 is different from the data. The data ratio is about 5% across all energy bins. Using this difference, the MC systematic error is scaled to get Data systematic error. The uncertainty values for each neutron energy bins before and after scaling are presented in table 7.3.

The average error across all energy bins presented in table 7.3 is 7.55%. Thus, the upper limit on this type of systematic can be placed at 10%. Although this systematic uncertainty dominates the contribution of over considered effects, it is still small if compared with the statistical uncertainty in the experiment. Thus, the uncertainty of the neutron cross section measurement in the experiment is dominated by statistical uncertainty.

In conclusion, the result presented in this chapter is the first measurement of the total neutron cross section on argon in the energy range of 100–800 MeV. The energy averaged cross section across all bins is $0.91 \pm 0.10(stat) \pm 0.09(syst)$ b with a $\chi^2 = 4.2/5$ ndof.

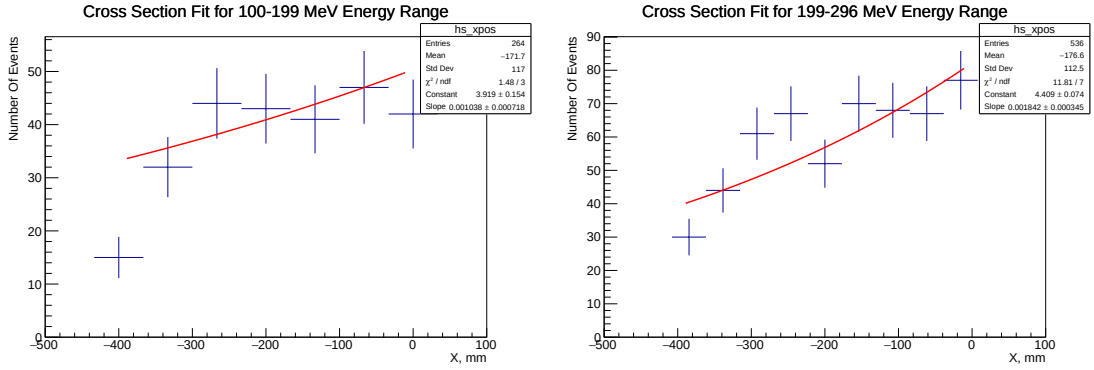

(a) Neutron energy : [100,199]MeV

(b) Neutron energy : [199,296]MeV

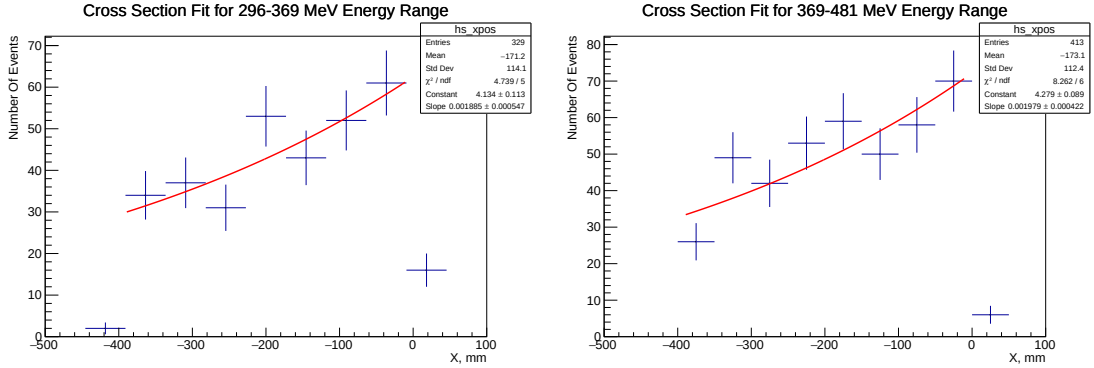

(c) Neutron energy : [296,369]MeV

(d) Neutron energy : [369,481]MeV

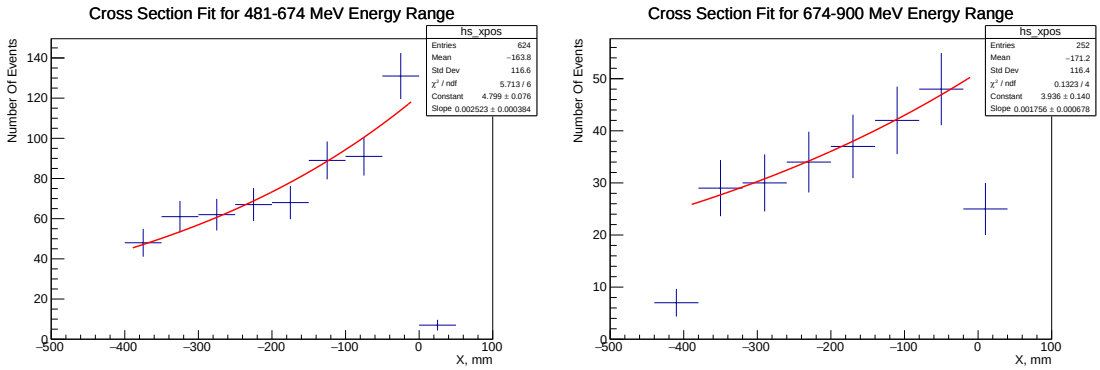

(e) Neutron energy : [481,674]MeV

(f) Neutron energy : [674,900]MeV

Figure 7.5: The exponential fit for starting position of reconstructed tracks from neutron interaction vs the depth in the detector.

Energy bin, MeV	Total number of events	Number of multi-track events	Cross section for all events (error), [b]	Cross section excluding multi-track events(error), [b]
100-199	$\sim 4.5 \times 10^4$	~ 225	0.6937 (4.47%)	0.6948 (4.34%)
199-296	$\sim 7.5 \times 10^4$	~ 1000	0.5480 (4.2%)	0.5409 (4.1%)
296-369	$\sim 10 \times 10^4$	~ 2100	0.5669 (3.4%)	0.5489 (3.36%)
369-481	$\sim 13 \times 10^4$	~ 3900	0.5586 (2.9%)	0.5461 (2.8%)
481-674	$\sim 15.5 \times 10^4$	~ 5500	0.6172 (2.3%)	0.5891 (2.3%)
674-900	$\sim 17 \times 10^4$	~ 7000	0.5770 (2.26%)	0.5632 (2.17%)

Table 7.2: The cross section for single and multi-track events in selection region. The results are obtained from neutron simulation exponential hypothesis.

Energy bin, [MeV]	Suggested systematic uncertainty from MC	Scaled to Data systematic uncertainty
100-199	6.3%	11.8%
199-296	7.16%	2.57%
296-369	7.98%	6.65%
369-481	6.3%	7.98%
481-674	7.85%	7.6%
674-900	5.13%	8.7%

Table 7.3: The cross section for single and multi-track events in selection region. The results are obtained from neutron simulation exponential hypothesis.

Chapter 8

Extended Neutron Cross Section Measurement

The final chapter focuses on the extension of the method of measuring the neutron cross section in liquid Argon described in the previous chapter. The new approach is based on developing the MC/Data fit. First, the fit structure is described. Second, the chapter focuses on fit validation and systematic studies using the Asimov sample. Finally, the fit application to the neutron data is described as well as the final cross section result.

8.1 Fit data structure

The data structure used for the fit borrows the idea of the initial cross section measurement method described in the previous chapter. The event selection criteria for the data and MC are the same:

- Only one reconstructed track in the total analysis region(50mm radius around the beam center) per micropulse for the Data and per event for MC;
- Reconstructed track should be at least 15mm long in the X projection (beam direction).

The fit is comparing histograms resembling the neutron beam attenuation inside the detector with a particular time of flight measurement.

First, there are 5 separate sets of histograms(bins) corresponding to different neutron time of flights. Time of flight bins are chosen based on PDS information from CAPTAIN low-intensity neutron run and available statistics for each TOF range. Figure 8.1 shows the measured time of flight for the CAPTAIN neutron

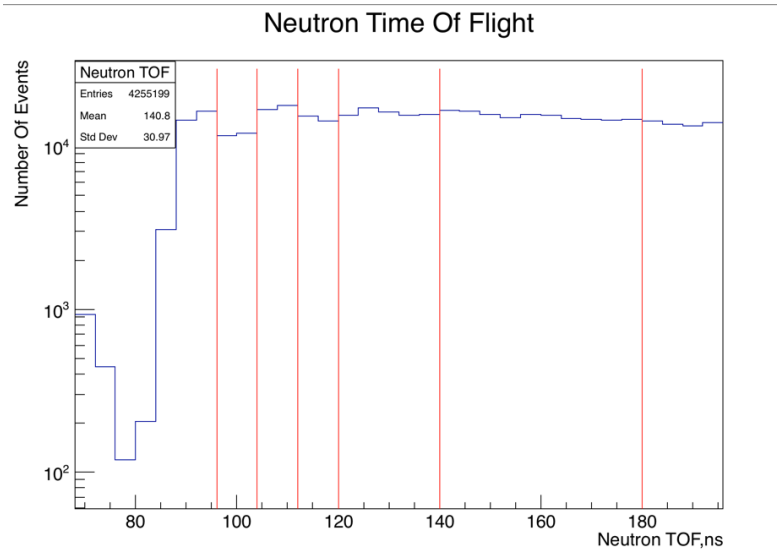

Figure 8.1: Neutron time of flight measured with PDS for the entire CAPTAIN data set.

data set. The 4ns bins on the plot resemble the resolution of the photon detection system. In total, the fit operates with five TOF bins, which confined between red lines in figure 8.1 : [140-180]ns , [120-140]ns , [112-120]ns , [104-112]ns , [96-104]ns.

The neutron time-of-flight for the MC simulation is calculated based on initial neutron energy and the distance between the source and the first sufficient interaction point inside the detector. The interaction point is defined as sufficient if it produces a charged particle with a track above 10mm inside the detector region, observed by photo-multiplier tubes. Figure 8.2 shows the selected TOF bins and corresponding neutron energy ranges in between red lines. The distribution of neutron energies inside each TOF bin according to simulation is shown in figure 8.3. The neutron energy ranges corresponding to selected TOF bins with flux averaged energies are listed in table 8.1.

Second, for each time-of-flight bin for the fit, the data is separated into two regions. The signal region that includes reconstructed tracks started in 25mm radius around the beam center and side region with track starting position between 25 and 50mm radius around the beam center. Both signal and side region histograms are filled based on the X coordinate of the starting position of the reconstructed track. The number of bins in X is chosen to be 6 in the signal region and 4 in the side region across all TOF bins. The binning choice is based on the available statistics in data. The fiducial volume for the detector is extended by 400mm along Xaxis in comparison with the initial measurement. Now it cov-

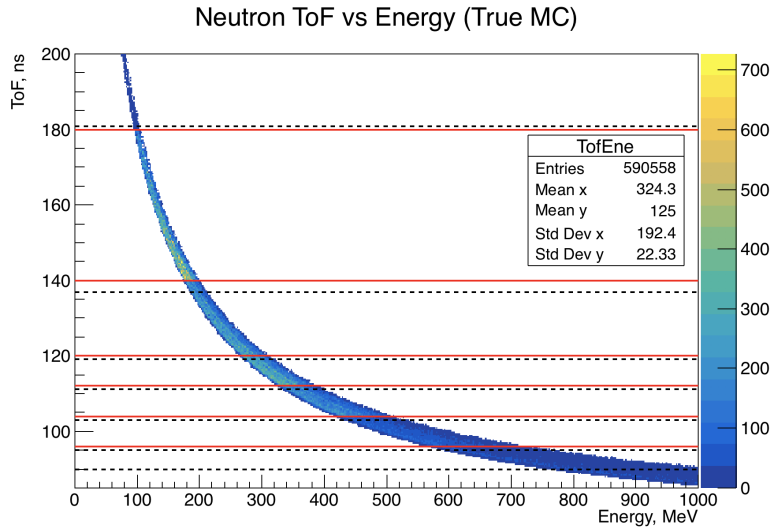

Figure 8.2: Neutron time of flight calculated based on MC simulation vs initial neutron energy. The red lines are chose TOF bins in the extended measurement. The black dashed lines are initial measurement Energy bins

ers full detector drift including upstream and downstream parts of the detector between -400 and 400mm.

To summarise, the new method has several critical differences in the track selection procedure in comparison with the initial analysis. The previous analysis used a 15mm cut in overall track length, while the new approach utilizes a 15mm cut only in the X projection of the reconstructed track. Moreover, the initial analysis only counted events with only one reconstructed track inside a 25mm radius around the beam center. The new method demands that there is only one reconstructed track in the 50mm region around the beam center. Finally, the fiducial volume is doubled in the new approach. These changes result in an overall increase in available statistics. The total number of considered events in the data (using the same low-intensity CAPTAIN neutron runs as before) grew 2.4 times from 2418 events to 5810 events across all neutron energies. The statistics available in each TOF bin is presented in table 8.2.

8.2 Fitting function and algorithms

The result of the procedure described above is a set of two histograms, one for the neutron data and the other for the MC simulation. Each histogram is divided into 5 large sections based on the time of flight of the neutron (TOF bins). Each TOF

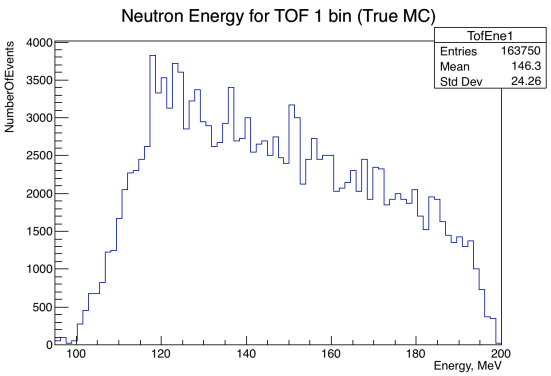

(a) TOF=[140,180]ns
$E_{Avg} = 143MeV$

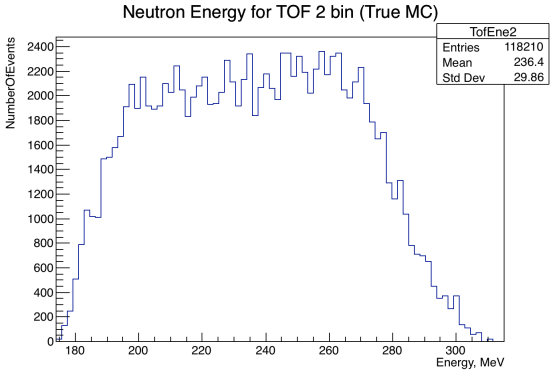

(b) TOF=[120,140]ns
$E_{Avg} = 236MeV$

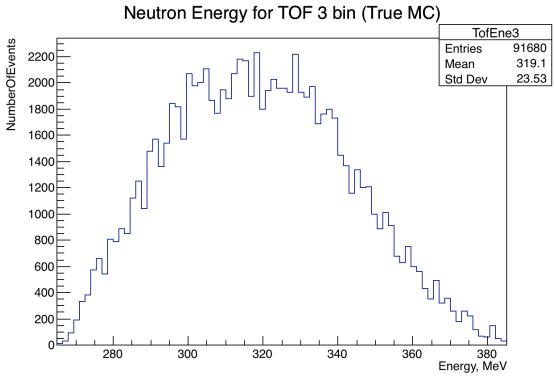

(c) TOF=[112,120]ns
$E_{Avg} = 319MeV$

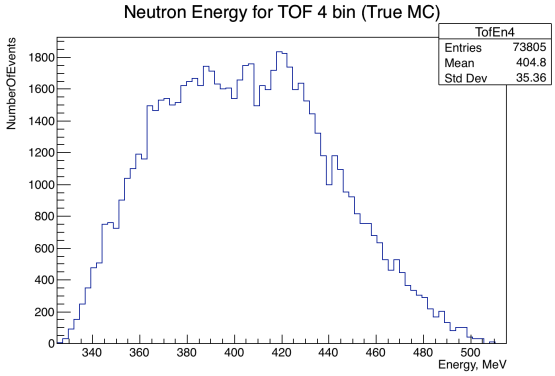

(d) TOF=[104,112]ns
$E_{Avg} = 404MeV$

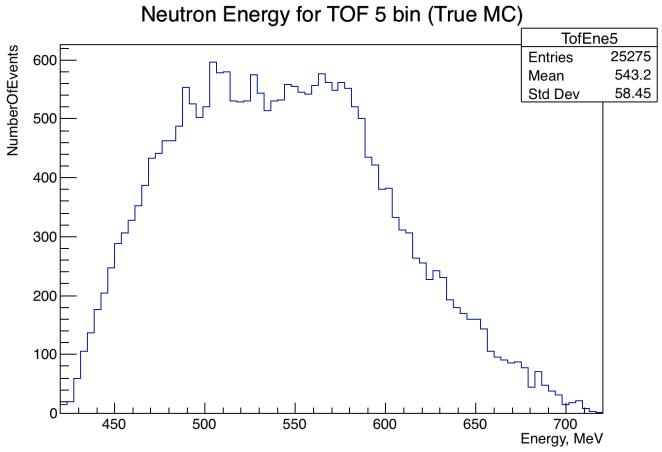

(e) TOF=[96,104]ns
$E_{Avg} = 543MeV$

Figure 8.3: The neutron energy distribution for each TOF bin according to MC simulation using neutron energy spectrum provided by LANSCE[51]. The flux weighted average energy for each bin is given in captions.

TOF range, [ns]	Energy Range, [MeV]	Flux averaged energy, [MeV]
140-180	95-200	143
120-140	174-315	236
112-120	265-385	319
104-112	325-515	404
96-104	420-720	543

Table 8.1: The neutron energy range and the flux weighted average energy for each TOF bin according to MC simulation using neutron energy spectrum provided by LANSCE[51] .

TOF range, [ns]	Number Of Events
140-180	625
120-140	1344
112-120	985
104-112	1272
96-104	1584

Table 8.2: Number of events in each TOF bin for the CAPTAIN low-intensity neutron data.

bin is separated into two subsections corresponding to the signal region and side region of the beam. Finally, each subsection is filled with the X coordinate of the starting position of the reconstructed track. These two histograms are compared against each other using χ^2 method. Thus, the fitting procedure is focused on minimizing the constructed χ^2 function.

$$\chi^2 = \sum_{i=1}^{n_{bins}} \frac{Data_i - MC_i}{Data_i} + C \tag{8.1}$$

where $Data_i$ is a number of events in i bin of Data histogram, MC_i is a re-weighted and normalized number of events in i bin of MC histogram, and C terms add constraints to fitting parameters. Each event in MC simulation is re-weighted based on the starting position of the initial neutron and the event topology it belongs to.

The study of neutron beam from low-intensity CAPTAIN runs is discussed in detail in chapter 5. The best fit line for the beam is given by the equation 5.1. The beam center of the MC simulation is set along the given line. However, the spread of the beam is set to be much wider than the data suggests. The beam spread

(sigma) observed in data and interpolated to the detector entrance is about 9.3mm in the Y direction and 7mm in the Z direction. The simulation uses a spread of 24mm in each direction. Thus, each MC event is assigned an initial weight based on the starting point of the initial neutron. The beam is assumed to have a Gaussian shape in both Y and Z directions. Thus, the simulated distribution of initial neutrons is fitted with function:

$$g = p_0 e^{-\frac{(x-p_1)^2}{2p_2^2}} \tag{8.2}$$

Next, parameter p_2 is set to resemble beam spread observed in the data. The final beam shape weight assigned to each MC event is the following:

$$W_{BeamShape} = \frac{g_{y_{new}}(y_n)}{g_{y_{initial}}(y_n)} \times \frac{g_{z_{new}}(z_n)}{g_{z_{initial}}(z_n)} \tag{8.3}$$

where g is Gaussian fit with and without corrected p_2 parameter in both directions, y_n and z_n are corresponding coordinates of the initial neutron.

The next re-weighting step is based on the event topology. All event topology definitions are based on primary neutron interaction in the detector. The primary interaction is defined such that neutron produces charged particles with the track above 15mm in X projection inside the detector fiducial volume (between -400mm and 400mm along the X axis). There are three event categories used in the analysis. First is the "signal" category. It is defined as the following:

- The true track from primary interaction has an initial neutron as a parent particle;
- The true track starting position deviates less than 0.1 mm from the path of the initial neutron.

The second category is called "elastic" and represents an event with neutron undergoing one or multiple elastic scatterings prior to the primary interaction. Moreover, interactions with the low energy transfer which do not change the ID of the particle in the GEANT simulation are also a part of this category. Thus, the category is defined as follows:

- The true track from primary interaction has an initial neutron as a parent particle;
- The true track starting position deviates more than 0.1 mm from the path of the initial neutron.

The final category for the re-weighting is called "Other". It combines all other possible event topologies including inelastic scattering, gamma production, etc.

Since the fitting histogram for the MC is filled based on the information coming from the reconstruction, some events do not have any true information associated with them. These events fall into a separate category called "NoTrueInfo". They get proper weigh based on the beam shape but are not re-weighted based on the event topology (have weight=1).

Weight for each category is assigned based on the survival probability of the neutron inside the detector. The probability is inherited from equation 7.1 and is given by:

$$P_{surv} = e^{-T \times l \times \sigma^{tot}} \tag{8.4}$$

where σ^{tot} is the total neutron cross section, l is the distance neutron traveled in the medium, and $T = \rho_{LAr} \times N_{Avogadro}/m_{Ar}$ is the nuclear density of liquid argon. The nuclear density is a constant in the experiment and equals $2.11 \times 10^{22} cm^{-3}$ [$T = (1.3973 g/cm^3 \times 6.022 \times 10^{23} n/mol)/39.948 g/mol$]. Thus, each "Signal category" event can be assigned with weight:

$$W_{Signal} = \frac{e^{-T \times l \times \sigma^{tot}_{new}(TOF)}}{e^{-T \times l \times \sigma^{tot}_{MC}(TOF)}} \tag{8.5}$$

where the $\sigma^{tot}_{new}(TOF)$ represents fitting cross section parameter for a given TOF bin. The $\sigma^{tot}_{MC}(TOF)$ represents the base flux averaged GEANT value for the neutron cross section for a given TOF bin. The values of $\sigma^{tot}_{MC}(TOF)$ for each TOF bin are obtained using a thin target measurement. The thin target measurement for each TOF bin was performed using a simulation of two million neutrons with energy equal to the fluxed averaged energy of a given bin. The large number of events allowed for a negligible statistical uncertainty. The cross section was extracted using the attenuation of the beam after 1 cm traveling distance. The neutron is counted as interacted if the charged particle track with a length above 15mm in X projection was produced. The results are presented in table 8.3.

TOF range, [ns]	Base cross section value, [b]
140-180	0.59
120-140	0.53
112-120	0.53
104-112	0.56
96-104	0.58

Table 8.3: Cross section values used as a base values in the fit. Values obtained via thin target measurement for each TOF bin.

The weight for the "Elastic category" events is assigned in a similar way with extra parameter describing branching ratio between two event categories:

$$W_{Elastic} = \frac{e^{-T\times l\times\sigma^{tot}_{new}(TOF)}}{e^{-T\times l\times\sigma^{tot}_{MC}(TOF)}} \times e^{-\alpha(TOF)} \tag{8.6}$$

where the $\alpha(TOF)$ represents fitting branching ratio parameter for a given TOF bin. The "Elastic category" can include multiple elastic events prior to the main interaction as well as other effects. Thus, the α parameter accounted for all these effects. The final "Other" category weight is defined as a free parameter and set to be:

$$W_{Other} = e^{-\delta(TOF)} \tag{8.7}$$

where the $\delta(TOF)$ represents fitting parameter for a given TOF bin.

The final step of the re-weighting process is a proper normalization of the MC. The normalization is applied for each TOF bin separately. The numerator of the normalization coefficient(N_{Data}) is the total number of neutron data events in a given TOF bin (both signal and side regions). The denominator(N_{MC}) is the total number of re-weighted MC events in a given TOF bin. The final form of the normalization coefficient is given as:

$$Norm(TOF) = \frac{N_{Data}(TOF)}{N_{MC}(TOF)} \tag{8.8}$$

The combination of all re-weighting steps gives the final form of the term MC_i in the initial χ^2 equation 8.1:

$$MC_i = Norm(TOF) \times \sum_{j=1}^{N_i}(W_{BeamShape} \times W_{Category}) \tag{8.9}$$

where Norm(TOF) is given by equation 8.8 for a given TOF bin, the N_i is a total number of events in i bin of the fitted histogram, and $W_{BeamShape}$ and $W_{Category}$ are weights assigned for each event in the beam based on the starting position of the initial neutron and event topology respectively.

To summarise, the χ^2 function given with equation 8.1 has 5 cross section parameters for each TOF bin, 5 parameters for the "elastic" topology re-weighting, and 5 parameters for the "other" topology. The total number of bins in the histogram is 50 (5 TOF bins with 6 signal region bins and 4 side region bins in each TOF bin). Thus, the number of degrees of freedom in the problem is 35. The fitting algorithm for this problem is chosen to be SIMPLEX[57] to find a function minimum. The Hessian matrix is calculated near the found minimum.

The approach also utilizes MINOS[58] algorithm near the minimum in order to find precise parameter errors in case of asymmetric function.

8.3 Asimov sample studies

The fit sensitivity can be evaluated using the so-called "Asimov" data set. The Asimov data set represents an average expectation of the experiment with given true cross-section parameters; the fit itself is also a sanity check of the fitting framework before analyzing data.

In order to construct a proper "Asimov" sample, the MC simulation of two million neutrons with a proper energy spectrum is taken. Since the MC simulates a broader beam than the one observed in the experimen,t the simulation is re-weighted based on the starting position of the initial neutron as described in the previous section. Finally, each TOF bin in MC scaled to the number of events observed in the experiment in a given bin.

The fitting technique described in the previous section is applied to "Asimov" data in order to check the function behavior and fit convergence capability. The preliminary study showed numeric convergence problems due to high correlations between the parameters in each TOF bin and overall function behavior near the minimum. The χ^2 function was studied around that minimum. The function has a similar shape for all ten non-cross section parameters, which is shown in figure 8.4. The function shape shows the presence of a plateau region that might interfere with numerical minimization algorithms. In order to fix this issue, the loose constraint for each non-cross section parameter is introduced. Each of the parameters initially set to the default GEANT values, which in this case are all zero (to make weight equal one). The variation of each parameter is allowed to be 2.3, which brings the exponential from equation 8.7 term to ± 10 possible variation around the base value. Thus, the constraint term in the equation 8.1 is given as:

$$C = \sum_{k=1}^{5} \frac{\alpha_k^2}{2.3^2} + \sum_{k=1}^{5} \frac{\delta_k^2}{2.3^2} \tag{8.10}$$

where k represents the number of TOF bin.

The application of the described constraint significantly improved the correlations. However, for the first TOF bin (highest time of flight or lowest energy neutrons) the correlations remain too high for the algorithm to perform proper error calculations around the minimum. Due to the low energy of incoming neutrons in this TOF bin, the number of expected events in the "other" category is low. Thus, the parameter δ_1 is fixed to the default GEANT value (zero) and is excluded from the fit. These changes led to the stable numeric convergence of the

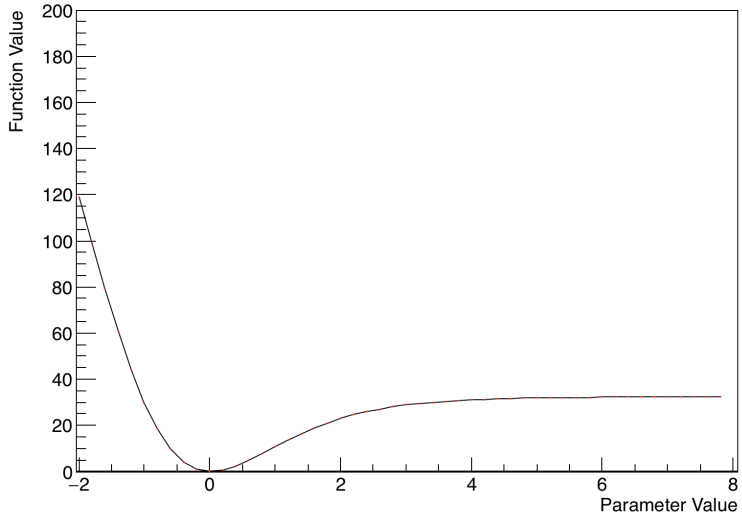

Figure 8.4: The general shape of the given χ^2 function near the minimum for all non-cross section parameters in the fit.

given algorithms with proper second derivatives around the minimum. Moreover, the number of parameters reduced by one brings the number of degrees of freedom in the problem to 36.

Fit in its final form was performed multiple times with various starting points for cross-section parameters to ensure that the algorithm finds the unique minimum. Out of 50 trials, fit successfully converged to a base cross-section values (table 8.3) with maximum divergence of 0.37%.

There are four major systematic effects on cross section parameters that are studied using the "Asimov" data set:

- The effect of "Other" topology events;
- The effect of "Elastic" events;
- The effect of multiple-track events in the cross section calculation;
- The effect of dead wire in the upstream region of the detector.

The "Other" category includes primarily inelastic events. Thus, the parameters describing this category are closely related to the inelastic neutron cross section in argon. Thus, the maximum uncertainty that can be put on these parameters can be derived from the difference between the cross section measurement described in [6] (for neutrons below 50MeV) and the initial measurement of CAPTAIN collaboration described in [7] (for energies above 100MeV). The core

TOF range, [ns]	Base cross section value , [b]	Post-fit cross section value, [b]	Statistical uncertainty, b	Systematic uncertainty, %
140-180	0.59	0.512	8.2×10^{-2}	13.2
120-140	0.53	0.533	7.4×10^{-2}	0.5
112-120	0.53	0.540	8.5×10^{-2}	1.8
104-112	0.56	0.568	6.8×10^{-2}	1.4
96-104	0.58	0.586	9.7×10^{-2}	1

Table 8.4: The result of the fit to "Asimov" data set with 4 times increased number of "Other" category events. Statistical uncertainties are taken from Hessian matrix.

difference between the given measurements is detector sensitivity. The inelastic threshold in liquid argon as given in [6] is 1.5MeV. However, the minimal detected energy loss is considered to signal interactions according to simulation in the mini-CAPTAIN detector is 60MeV, as presented in figure 8.5. Two measurements are different by a factor of 4. Thus, the variation on the number of "other" in the "Asimov" data set is set to be 4 times the simulated value. The result of the fit with 4 times increased number of "other" events in each TOF bin is presented in table 8.4. According to the study, only the first TOF bin has a significant systematic effect from this change evaluated at 14%.

The evaluation of the systematic effect of "Elastic" events on cross-section parameters is based on the same logic as described above. The maximum variation on the number of "elastic" events in the "Asimov" data set is set to be 4 times its initial value. The result of the fit with this change is presented in table 8.5. The results suggest that fit is not sensitive to the given change in the "Elastic" topology.

The effect of multi-track events was the dominant systematic effect for the initial cross section measurement. The Initial study shown in table 7.2 suggests that, according to simulation, the expected number of multi-track events is 5% of a total. Thus, the total number of events in the "Asimov" data set is varied by $\pm5\%$ in order to determine the effect of these events on cross section parameters. The table 8.6 shows that the change in cross section does not exceed 2%. Thus, the effect of multi-track events is negligible in the new measurement.

The final studied systematic effect is caused by uncertainty in the number of inefficient wires in the upstream part of the detector. All wires in the MC simulation have the same efficiency of 97%, while wire efficiency in the experiment can vary. The full comparison is described in chapter 6 and presented in figure 6.6. The total number of disabled wires in the upstream part of the detector is 65 out

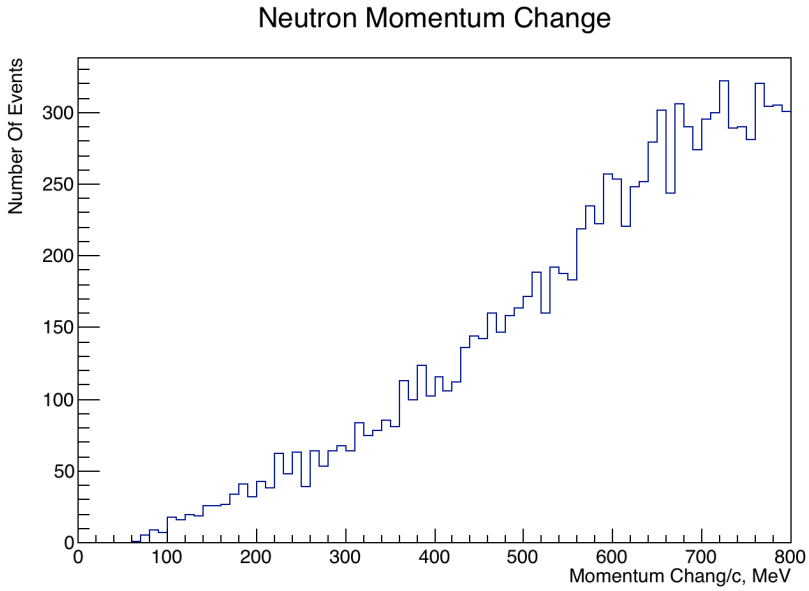

Figure 8.5: The Momentum change of the initial neutron in interactions considered for the cross section measurement.

of 165. In order to estimate the uncertainty on this number, the effective number of expected inefficient wires is calculated. The efficiency of each wire observed in the experiment in the upstream part of the detector is subtracted from the simulated uncertainty. The sum of absolute values of these differences is 6.4 for the X plane. This number is used as a desired uncertainty. The effect of this uncertainty is studied using the "Asimov" data set. Each functional wire in the upstream part of the MC simulation is set to be skipped with a 7% probability. This led to approximately 7 wires variation out of 100 simulated functional wires. The fit result presented in table 8.7 suggests that this is not a dominant systematic uncertainty in the experiment.

To summarise, the dominant systematic uncertainty for the first TOF bin is variation in cross section of "other" events and evaluated as 14%. For the rest of the TOF bins studied systematic uncertainties do not exceed 4%.

8.4 Neutron data fit

Finalized fit can be used to study neutron data from CAPTAIN low-intensity runs. The data set for this study is the same as described in CAPTAIN PRL paper [7].

First, the SIMPLEX algorithm was run multiple times with various starting

TOF range, [ns]	Base cross section value , [b]	Post-fit cross section value, [b]	Statistical uncertainty, b	Systematic uncertainty, %
140-180	0.59	0.588	8.9×10^{-2}	0.34
120-140	0.53	0.526	7.7×10^{-2}	0.75
112-120	0.53	0.522	7.8×10^{-2}	1.5
104-112	0.56	0.54	6.5×10^{-2}	3.57
96-104	0.58	0.569	9.5×10^{-2}	1.89

Table 8.5: The result of the fit to "Asimov" data set with the 4 times increase in the number of "Elastic" category events. Statistical uncertainties are taken from Hessian matrix.

TOF range, [ns]	Base cross section value , [b]	Post-fit cross section value, [b]	Statistical uncertainty, b	Systematic uncertainty, %
140-180	0.59	0.592	11×10^{-2}	0.339
120-140	0.53	0.532	7.3×10^{-2}	0.377
112-120	0.53	0.532	9.5×10^{-2}	0.377
104-112	0.56	0.571	7.9×10^{-2}	1.96
96-104	0.58	0.585	9.8×10^{-2}	0.862

Table 8.6: The result of the fit to "Asimov" data set with $\pm5\%$ variation of total number of events to accommodate to the predicted number of multi-track events in the experiment. Statistical uncertainties are taken from Hessian matrix.

points for each cross-section parameter to prove the existence of the unique minimum. Figure 8.6 shows the result of multiple fits performed with various starting points. The fit converged successfully to the same point with a maximum of 5% variation across all cross-section parameters.

Second, all parameters were set to a base GEANT values defined in table 8.3 for cross-section parameters and zeros for the rest. The SIMPLEX algorithm is performed followed by Hessian matrix calculation around the minimum. Next, the error calculation is performed by the MINOS algorithm around the minimum. The cross section result of the fit for each TOF bin is presented in table 8.8 with global correlations derived from the Hessian matrix. The results for "Elastic" and "Other" parameters are shown in tables 8.9 and 8.10 respectively.

Fit demonstrates good agreement between the data and MC. The final value of χ^2 is 42.12 with 36 degrees of freedom. Thus, the p-value is 0.223. The comparison

TOF range, [ns]	Base cross section value , [b]	Post-fit cross section value, [b]	Statistical uncertainty, [b]	Systematic uncertainty, %
140-180	0.59	0.572	10.1×10^{-2}	3.05
120-140	0.53	0.519	8×10^{-2}	2.08
112-120	0.53	0.527	7.9×10^{-2}	0.57
104-112	0.56	0.558	7.7×10^{-2}	0.36
96-104	0.58	0.578	8.2×10^{-2}	0.34

Table 8.7: The result of the fit to "Asimov" data set with 7% variation of the number of efficient wires in the upstream part of the detector. Statistical uncertainties are taken from the Hessian matrix.

between the data and posterior MC distributions for each TOF bin are presented in figure 8.7 for the signal region and in figure 8.8 for the side region. The p-values for the side regions of the first two time of flight bins are about 0.04. However, this is still consistent with the fit assumption given the limited statistics and the number of trials available. The final cross sections are given for flux averaged energies in considered time-of-flight bins: $\sigma_{146} = 0.601^{+0.140}_{-0.143}\pm0.084(syst)$ b, $\sigma_{236} = 0.722^{+0.103}_{-0.101}\pm0.036(syst)$ b, $\sigma_{319} = 0.804^{+0.129}_{-0.121}\pm0.040(syst)$ b, $\sigma_{404} = 0.739^{+0.135}_{-0.091}\pm 0.037(syst)$ b, $\sigma_{543} = 0.741^{+0.088}_{-0.088}\pm0.037(syst)$ b. The result is consistent with the hypothesis of small cross section change across considered energy range. The χ^2 for a given function with flux averaged cross section of $0.731\pm0.4(syst)$ across all TOF bins gives value of 44.27. This value in combination with 36 degrees of freedom yields p-value of 0.162. The result of the extended measurement is consistent with the result of the initial measurement as shown in figure 8.9.

TOF range, [ns]	Parameter	Post-fit cross section value, [b]	Global correlation
140-180	σ_{146}	$0.601^{+0.140}_{-0.143}$	0.111
120-140	σ_{236}	$0.722^{+0.103}_{-0.101}$	0.138
112-120	σ_{319}	$0.804^{+0.129}_{-0.121}$	0.226
104-112	σ_{404}	$0.739^{+0.135}_{-0.091}$	0.544
96-104	σ_{543}	$0.741^{+0.088}_{-0.088}$	0.429

Table 8.8: The post-fit cross sections for flux averaged energies inside each neutron time of flight bin. The Statistical error is calculated using MINOS[58] algorithm.

TOF range, [ns]	Parameter	Post-fit parameter value	Statistical uncertainty	Global correlation
140-180	α_1	-4.3×10^{-3}	0.219	0.111
120-140	α_2	0.176	0.539	0.915
112-120	α_3	0.143	0.887	0.929
104-112	α_4	0.283	0.771	0.892
96-104	α_5	-0.211	0.208	0.528

Table 8.9: The post-fit "elastic" category parameter values for each neutron time of flight. The Statistical error is calculated using Hessian matrix.

TOF range, [ns]	Parameter	Post-fit parameter value	Statistical uncertainty	Global correlation
140-180	-	-	-	-
120-140	δ_2	-1.01×10^{-3}	0.606	0.915
112-120	δ_3	-0.035	0.713	0.931
104-112	δ_4	0.029	0.679	0.898
96-104	δ_5	2.051	1.238	0.373

Table 8.10: The post-fit "other" category parameter values for each neutron time of flight. The Statistical error is calculated using Hessian matrix.

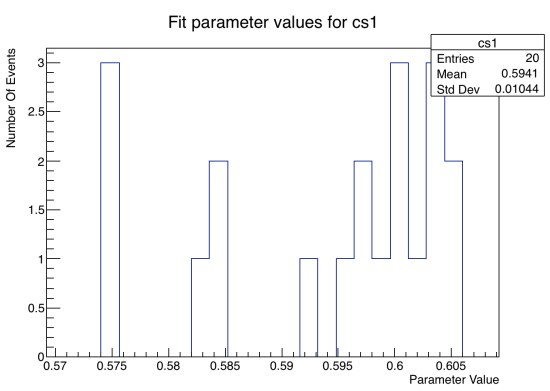

(a) TOF=[140,180]ns

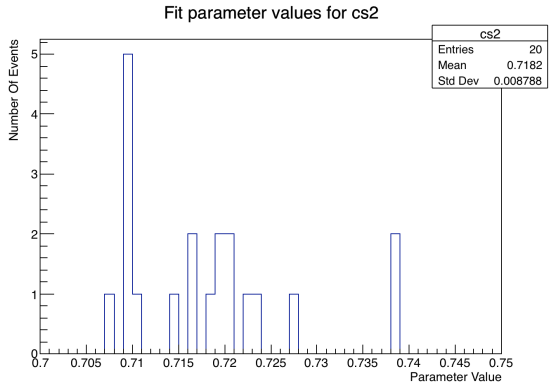

(b) TOF=[120,140]ns

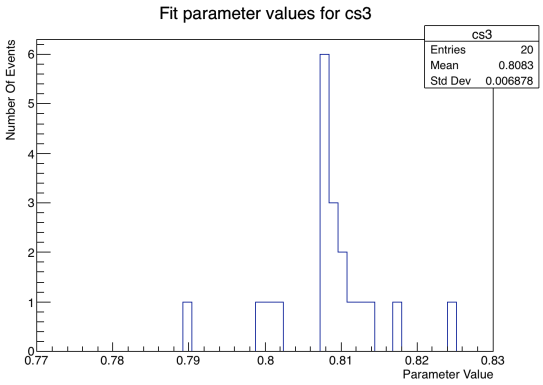

(c) TOF=[112,120]ns

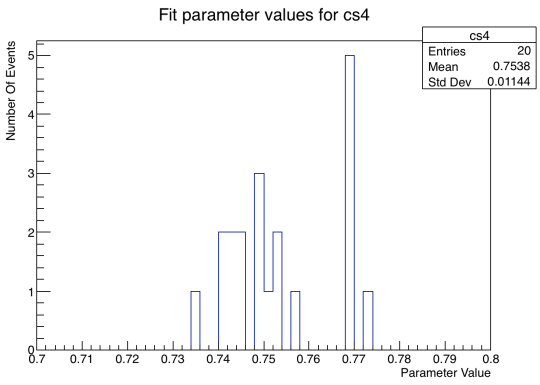

(d) TOF=[104,112]ns

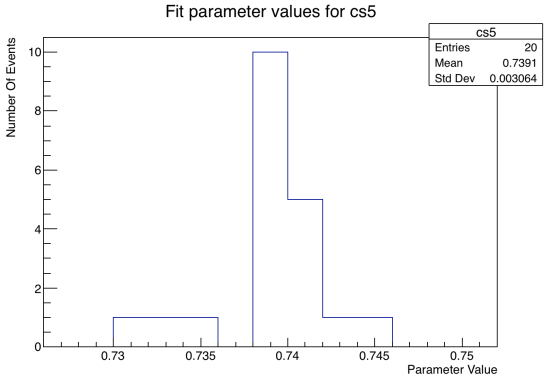

(e) TOF=[96,104]ns

Figure 8.6: The results of the Data/MC fit for all cross section parameters with variation of starting point of the fit.

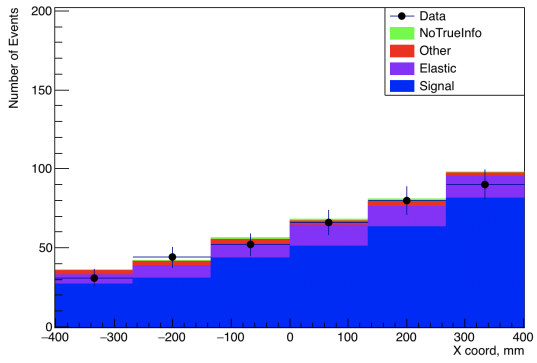

(a) TOF=[140,180]ns
$\chi^2/NDF = 2.23/6$

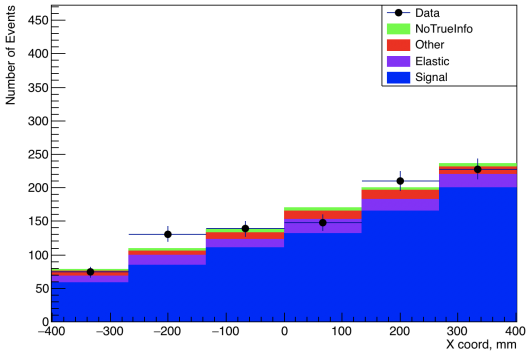

(b) TOF=[120,140]ns
$\chi^2/NDF = 7.65/6$

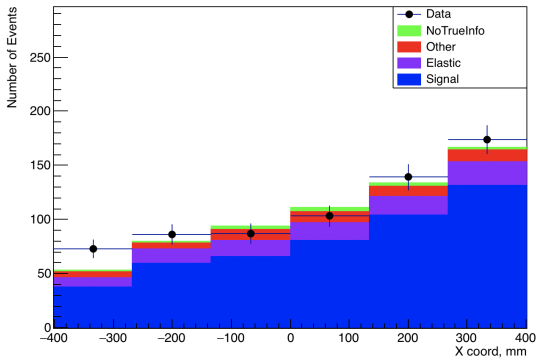

(c) TOF=[112,120]ns
$\chi^2/NDF = 7.48/6$

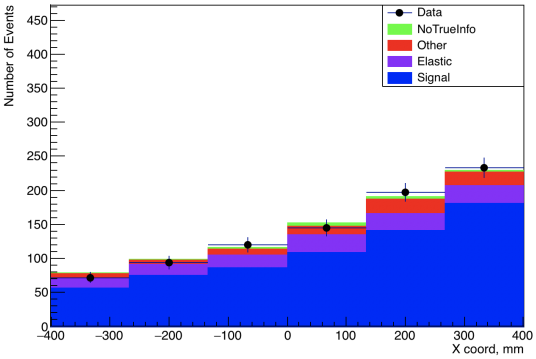

(d) TOF=[104,112]ns
$\chi^2/NDF = 1.716/6$

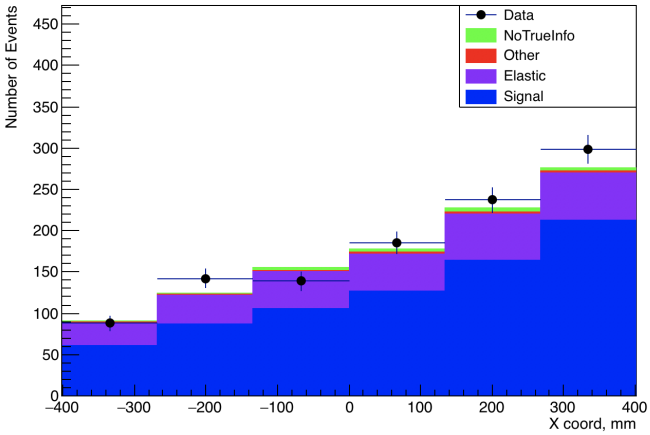

(e) TOF=[96,104]ns
$\chi^2/NDF = 6.33/6$

Figure 8.7: Post-fit distribution of starting position of reconstructed tracks inside the signal region for each TOF bin.

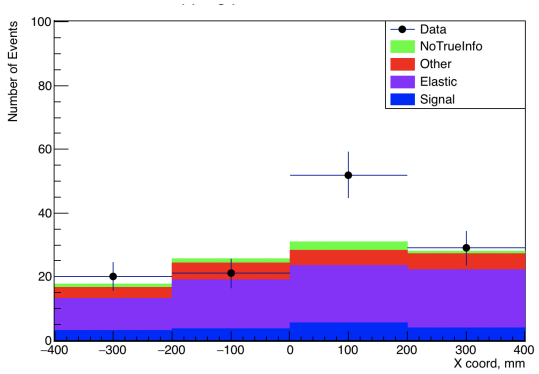

(a) TOF=[140,180]ns
$\chi^2/NDF = 9.897/4$

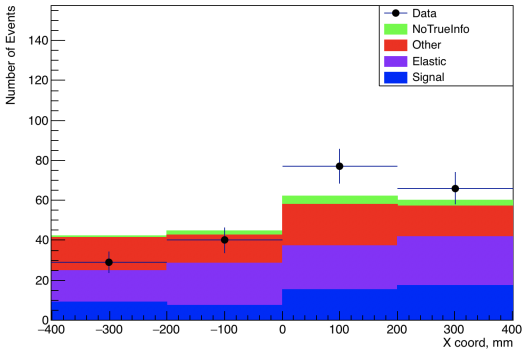

(b) TOF=[120,140]ns
$\chi^2/NDF = 10.16/4$

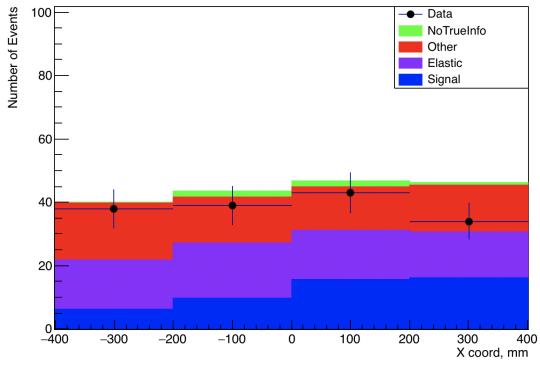

(c) TOF=[112,120]ns
$\chi^2/NDF = 5.29/4$

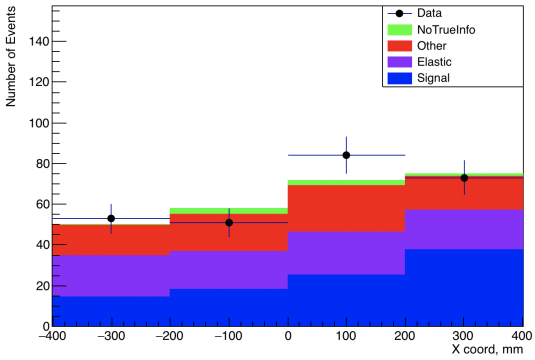

(d) TOF=[104,112]ns
$\chi^2/NDF = 3.02/4$

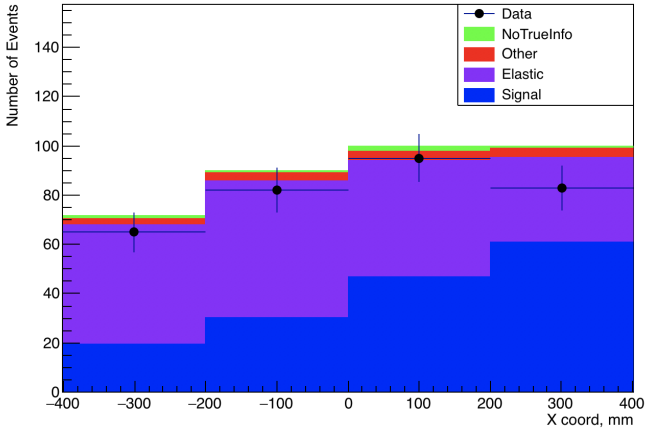

(e) TOF=[96,104]ns
$\chi^2/NDF = 5.175/4$

Figure 8.8: Post-fit distribution of starting position of reconstructed tracks inside the side region for each TOF bin.

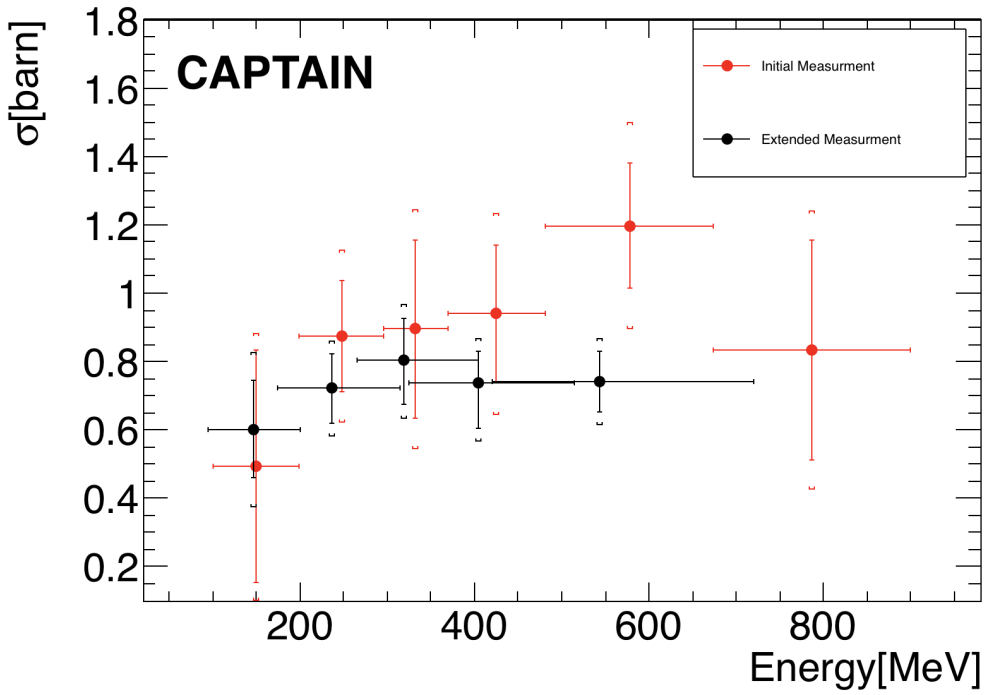

Figure 8.9: The comparison between the initial neutron cross section measurement and the extended measurement. The red points represent the initial neutron cross section measurement with statistical(lines) and systematic(hats) errors. The black dots represent extended cross section measurements for flux averaged energy in each of five considered time-of-flight bins. The extended measurement presented with with statistical(lines) and systematic(hats) errors.

Chapter 9

Summary

The Liquid Argon TPC (LArTPC) technology originally proposed for neutrino detectors [1] as an analog to bubble chambers, where the charged particle tracks could be clearly seen by the eye, is now being used in multiple neutrino experiments [2–5]. This detection method has high precision and a low energy threshold, which together allows highly detailed reconstruction of neutrino events. As a charged particle passes through a medium, it creates ionization. An electric field causes the produced electrons to drift to wires at the top(bottom) of the detector. The drift time and the position of the hit wire are combined to provide a 3D reconstruction of the event, neutrons are produced as well. Neutrons have no electric charge and can't be directly detected. However, they carry a considerable amount of energy. This energy escapes detection, thus provide a significant uncertainty to neutrino energy reconstruction and as a result neutrino oscillation probability. Models used to estimate missing energy, including neutrons, have large unconstrained uncertainties.

The CAPTAIN (Cryogenic Apparatus for Precision tests of Argon Interactions with Neutrinos) experiment's goal is to measure the neutron cross section and define the neutron signature in liquid argon in the 100 MeV to 800 MeV energy range. This measurement is of great interest in neutrino physics. In particular, data provided by the CAPTAIN collaboration will serve the needs of the planned experiment DUNE (Deep Underground Neutrino Experiment), which will be a neutrino oscillation experiment using a Liquid Argon detector. The simulation shows that the energy that will be carried away by neutrons in DUNE vary from MeV to 2 GeV. However, prior to the work of CAPTAIN collaboration, the Neutron-Argon cross section data was only published up to 50 MeV of kinetic energy [6].

The work presents the first measurement of the neutron cross section on argon in the energy range relevant for the DUNE experiment(100–800 MeV). The measurement is obtained using the data from a 4.3-h exposure of the Mini-CAPTAIN

detector to the WNR/LANSCE beam at Los Alamos National Lab. The measured cross section is presented in two forms.

First, the total cross section is measured from the attenuation coefficient of the neutron flux as it traverses the liquid argon volume. The method utilizes only the downstream part of the detector with a set of 2631 candidate interactions divided in bins of the neutron kinetic energy calculated from time-of-flight measurements. The energy averaged cross section is 0.91 ± 0.10(stat) ± 0.09(syst) b.

Second, the extended measurement performed using custom-made data/mc fit based on attenuation of the neutron flux. The detector fiducial volume for the measurement is doubled and statistics improved by the factor of 2.4. The new approach utilizes time-of-flight bins instead of energy bins. The final cross sections are given for flux averaged energies in considered time-of-flight bins: $\sigma_{146} = 0.601^{+0.140}_{-0.143} \pm 0.084(syst)$ b, $\sigma_{236} = 0.722^{+0.103}_{-0.101} \pm 0.036(syst)$ b, $\sigma_{319} = 0.804^{+0.129}_{-0.121} \pm 0.040(syst)$ b, $\sigma_{404} = 0.739^{+0.135}_{-0.091} \pm 0.037(syst)$ b, $\sigma_{543} = 0.741^{+0.088}_{-0.088} \pm 0.037(syst)$ b. The result is consistent with the hypothesis of small cross section change across the considered energy range. The χ^2 for a given function with an average cross section of 0.721 across all TOF bins gives value of 43.89. This value in combination with 36 degrees of freedom yields p-value of 0.172. Finally, both cross section measurements described in this work are consistent with one another.

Improvements in fit are needed to further increase the precision of the measurement. The current version of the fit defines event category based on first neutron interaction with a track longer than 10mm. Moreover, the fit divides all events between three base event typologies. The approach that can utilize the detailed structure of each neutron event in mini-CAPTAIN is needed. The "Other" topology can be expended to several more precise categories such as inelastic scattering and gamma production. All of these changes can lead to a better re-weighting and overall improvement of the fit quality.

The described measurement utilizes only the data from 4.3h exposure to a low-intensity neutron beam. However, the mini-CAPTAIN had a high-intensity neutron run for about a day as well. The data from this period can significantly reduce the statistical uncertainty in the experiment and open the possibility of determining partial neutron cross sections.

The analysis of high-intensity neutron data poses a big challenge. The resolution of current reconstruction algorithms in mini-CAPTAIN should be reworked and optimized to serve the extended data set. Moreover, the more sophisticated algorithms for the photon detection system can be applied to improve the energy resolution in the experiment.

The Liquid Argon neutrino experiments such as DUNE are poised to shape the future measurements in neutrino physics. It is my humble wish that this study will be a valuable help on a way toward this goal.

References

[1] C. Rubbia. The liquid-argon time projection chamber: a new concept for neutrino detectors. Technical Report CERN-EP-INT-77-8, CERN, Geneva, 1977. URL `https://cds.cern.ch/record/117852`.

[2] B. Abi et al. The DUNE Far Detector Interim Design Report Volume 1: Physics, Technology and Strategies. 2018.

[3] M. Antonello et al. A Proposal for a Three Detector Short-Baseline Neutrino Oscillation Program in the Fermilab Booster Neutrino Beam. 2015.

[4] R. Acciarri et al. Design and Construction of the MicroBooNE Detector. *JINST*, 12(02):P02017, 2017. doi: 10.1088/1748-0221/12/02/P02017.

[5] F. Cavanna, M. Kordosky, J. Raaf, and B. Rebel. LArIAT: Liquid Argon In A Testbeam. 2014.

[6] R. R. Winters, R. F. Carlton, C. H. Johnson, N. W. Hill, and M. R. Lacerna. Total cross section and neutron resonance spectroscopy for $n+^{40}ar$. *Phys. Rev. C*, 43:492–509, Feb 1991. doi: 10.1103/PhysRevC.43.492. URL `https://link.aps.org/doi/10.1103/PhysRevC.43.492`.

[7] B Bhandari, J Bian, K Bilton, C Callahan, J Chaves, H Chen, D Cline, RL Cooper, D Danielson, J Danielson, et al. First measurement of the total neutron cross section on argon between 100 and 800 mev. *Physical review letters*, 123(4):042502, 2019.

[8] Sheldon L Glashow. Partial-symmetries of weak interactions. *Nuclear physics*, 22(4):579–588, 1961.

[9] Steven Weinberg. A model of leptons. *Physical review letters*, 19(21):1264, 1967.

[10] Abdus Salam. Weak and electromagnetic interactions. In *Selected Papers Of Abdus Salam: (With Commentary)*, pages 244–254. World Scientific, 1994.

[11] H David Politzer. Reliable perturbative results for strong interactions? *Physical Review Letters*, 30(26):1346, 1973.

[12] David J Gross and Frank Wilczek. Ultraviolet behavior of non-abelian gauge theories. *Physical Review Letters*, 30(26):1343, 1973.

[13] Dave Fehling. The standard model of particle physics: A lunchbox's guide. *The Johns Hopkins University, Retrieved on*, pages 12–03, 2008.

[14] Pauli letter collection (german). URL `http://cds.cern.ch/record/83282/files/meitner_0393.pdf`.

[15] Лев Борисович Окунь. *Физика элементарных частиц*. URSS, 2008.

[16] Bruce T Cleveland, Timothy Daily, Raymond Davis Jr, James R Distel, Kenneth Lande, CK Lee, Paul S Wildenhain, and Jack Ullman. Measurement of the solar electron neutrino flux with the homestake chlorine detector. *The Astrophysical Journal*, 496(1):505, 1998.

[17] M Cribier, W Hampel, G Heusser, J Kiko, T Kirsten, M Laubenstein, E Pernicka, W Rau, U Rönn, C Schlosser, et al. Results of the whole gallex experiment. *Nuclear Physics B-Proceedings Supplements*, 70(1-3):284–291, 1999.

[18] JN Abdurashitov, EP Veretenkin, VM Vermul, VN Gavrin, SV Girin, VV Gorbachev, PP Gurkina, GT Zatsepin, TV Ibragimova, AV Kalikhov, et al. Solar neutrino flux measurements by the soviet-american gallium experiment (sage) for half the 22-year solar cycle. *Journal of Experimental and Theoretical Physics*, 95(2):181–193, 2002.

[19] Y Fukuda, T Hayakawa, E Ichihara, K Inoue, K Ishihara, Hirokazu Ishino, Y Itow, T Kajita, J Kameda, S Kasuga, et al. Evidence for oscillation of atmospheric neutrinos. *Physical Review Letters*, 81(8):1562, 1998.

[20] KamLAND& Eguchi, S Enomoto, K Furuno, J Goldman, H Hanada, H Ikeda, K Ikeda, K Inoue, K Ishihara, W Itoh, et al. First results from kamland: evidence for reactor antineutrino disappearance. *Physical Review Letters*, 90 (2):021802, 2003.

[21] S Abe, T Ebihara, S Enomoto, K Furuno, Y Gando, K Ichimura, H Ikeda, K Inoue, Y Kibe, Y Kishimoto, et al. Precision measurement of neutrino oscillation parameters with kamland. *Physical Review Letters*, 100(22):221803, 2008.

[22] S Schael, R Barate, R Bruneliere, John Renner Hansen, Peter Henrik Hansen, Bj^rn Stefan Nilsson, et al. Precision electroweak measurement on the z resonance. *Physics Reports*, 427(5-6):257–454, 2006.

[23] Michele Maltoni and Alexei Yu Smirnov. Solar neutrinos and neutrino physics. *The European Physical Journal A*, 52(4):87, 2016.

[24] Lincoln Wolfenstein. Neutrino oscillations in matter. *Physical Review D*, 17 (9):2369, 1978.

[25] SP Mikheev and A Yu Smirnov. Resonance amplification of oscillations in matter and spectroscopy of solar neutrinos. *Yadernaya Fizika*, 42(6):1441–1448, 1985.

[26] Takaaki Kajita. Atmospheric neutrinos. *New Journal of Physics*, 6(1):194, 2004.

[27] Kohji S Hirata, Takaaki Kajita, T Kifune, K Kihara, Masayuki Nakahata, K Nakamura, S Ohara, Y Oyama, N Sato, M Takita, et al. Observation of b 8 solar neutrinos in the kamiokande-ii detector. *Physical Review Letters*, 63 (1):16, 1989.

[28] P Anselmann, W Hampel, G Heusser, J Kiko, T Kirsten, E Pernicka, R Plaga, U Rönn, M Sann, C Schlosser, et al. Solar neutrinos observed by gallex at gran sasso. *Physics Letters B*, 285(4):376–389, 1992.

[29] Y Fukuda, T Hayakawa, K Inoue, K Ishihara, Hirokazu Ishino, S Joukou, T Kajita, S Kasuga, Yusuke Koshio, T Kumita, et al. Solar neutrino data covering solar cycle 22. *Physical Review Letters*, 77(9):1683, 1996.

[30] Q Retal Ahmad, RC Allen, TC Andersen, JD Anglin, JC Barton, EW Beier, M Bercovitch, J Bigu, SD Biller, RA Black, et al. Direct evidence for neutrino flavor transformation from neutral-current interactions in the sudbury neutrino observatory. *Physical review letters*, 89(1):011301, 2002.

[31] Gianpaolo Bellini, J Benziger, D Bick, S Bonetti, G Bonfini, D Bravo, M Buizza Avanzini, B Caccianiga, L Cadonati, F Calaprice, et al. First evidence of p e p solar neutrinos by direct detection in borexino. *Physical Review Letters*, 108(5):051302, 2012.

[32] MH Ahn, E Aliu, S Andringa, S Aoki, Y Aoyama, J Argyriades, K Asakura, R Ashie, F Berghaus, HG Berns, et al. Measurement of neutrino oscillation by the k2k experiment. *Physical Review D*, 74(7):072003, 2006.

[33] P Adamson, C Andreopoulos, KE Arms, R Armstrong, DJ Auty, DS Ayres, B Baller, PD Barnes Jr, G Barr, WL Barrett, et al. Measurement of neutrino oscillations with the minos detectors in the numi beam. *Physical Review Letters*, 101(13):131802, 2008.

[34] K Abe, N Abgrall, Y Ajima, H Aihara, JB Albert, C Andreopoulos, B Andrieu, S Aoki, O Araoka, J Argyriades, et al. Indication of electron neutrino appearance from an accelerator-produced off-axis muon neutrino beam. *Physical Review Letters*, 107(4):041801, 2011.

[35] P Adamson, DJ Auty, DS Ayres, C Backhouse, G Barr, M Betancourt, M Bishai, A Blake, GJ Bock, DJ Boehnlein, et al. Improved search for muon-neutrino to electron-neutrino oscillations in minos. *Physical Review Letters*, 107(18):181802, 2011.

[36] Y Abe, Christoph Aberle, T Akiri, JC Dos Anjos, F Ardellier, AF Barbosa, A Baxter, M Bergevin, A Bernstein, TJC Bezerra, et al. Indication of reactor ν e disappearance in the double chooz experiment. *Physical Review Letters*, 108(13):131801, 2012.

[37] FP An, JZ Bai, AB Balantekin, HR Band, D Beavis, W Beriguete, M Bishai, S Blyth, K Boddy, RL Brown, et al. Observation of electron-antineutrino disappearance at daya bay. *Physical Review Letters*, 108(17):171803, 2012.

[38] Jung Keun Ahn, S Chebotaryov, JH Choi, S Choi, W Choi, Y Choi, HI Jang, JS Jang, EJ Jeon, IS Jeong, et al. Observation of reactor electron antineutrinos disappearance in the reno experiment. *Physical Review Letters*, 108(19): 191802, 2012.

[39] K Abe, J Amey, C Andreopoulos, M Antonova, S Aoki, A Ariga, D Autiero, S Ban, M Barbi, GJ Barker, et al. Combined analysis of neutrino and antineutrino oscillations at t2k. *Physical review letters*, 118(15):151801, 2017.

[40] P Adamson, L Aliaga, D Ambrose, Nikolay Anfimov, A Antoshkin, E Arrieta-Diaz, K Augsten, A Aurisano, C Backhouse, M Baird, et al. Constraints on oscillation parameters from ν e appearance and ν μ disappearance in nova. *Physical Review Letters*, 118(23):231801, 2017.

[41] M Tanabashi, K Hagiwara, K Hikasa, K Nakamura, Y Sumino, F Takahashi, J Tanaka, K Agashe, G Aielli, C Amsler, et al. Review of particle physics: particle data groups. 2018.

[42] Joseph A Formaggio and GP Zeller. From ev to eev: Neutrino cross sections across energy scales. *Reviews of Modern Physics*, 84(3):1307, 2012.

[43] R Acciarri, MA Acero, M Adamowski, C Adams, P Adamson, S Adhikari, Z Ahmad, CH Albright, T Alion, E Amador, et al. Long-baseline neutrino facility (lbnf) and deep underground neutrino experiment (dune) conceptual design report volume 2: the physics program for dune at lbnf. *arXiv preprint arXiv:1512.06148*, 2015.

[44] Costas Andreopoulos, A Bell, D Bhattacharya, F Cavanna, J Dobson, S Dytman, H Gallagher, P Guzowski, R Hatcher, P Kehayias, et al. The genie neutrino monte carlo generator. *Nuclear Instruments and Methods in Physics Research Section A: Accelerators, Spectrometers, Detectors and Associated Equipment*, 614(1):87–104, 2010.

[45] Lanl facility description. URL `http://lansce.lanl.gov/facilities/index.php`.

[46] CE Taylor, B Bhandari, J Bian, K Bilton, C Callahan, J Chaves, H Chen, D Cline, RL Cooper, DL Danielson, et al. The mini-captain liquid argon time projection chamber. *arXiv preprint arXiv:2008.11422*, 2020.

[47] George Bakale, Ulrich Sowada, and Werner F Schmidt. Effect of an electric field on electron attachment to sulfur hexafluoride, nitrous oxide, and molecular oxygen in liquid argon and xenon. *The Journal of Physical Chemistry*, 80(23):2556–2559, 1976.

[48] Criotec impianti s.p.a. URL `https://www.criotec.com/en`.

[49] Hucheng Chen, K Chen, G De Geronimo, F Lanni, D Lissauer, D Makowiecki, V Radeka, S Rescia, C Thorn, and B Yu. Readout electronics for the microboone lar tpc, with cmos front end at 89k. *Journal of Instrumentation*, 7 (12):C12004, 2012.

[50] G. K. at al. G. Cheng. Tpc electronics and readout prototype i. i. test results. *Nevis Laboratory Technical Report*, 2012.

[51] Suzanne F Nowicki, Stephen A Wender, and Michael Mocko. The los alamos neutron science center spallation neutron sources. *Physics Procedia*, 90:374–380, 2017.

[52] Richard O Duda and Peter E Hart. Use of the hough transformation to detect lines and curves in pictures. *Communications of the ACM*, 15(1):11–15, 1972.

[53] S. Agostinelli et al. GEANT4: A Simulation toolkit. *Nucl. Instrum. Meth.*, A506:250–303, 2003. doi: 10.1016/S0168-9002(03)01368-8.

[54] M Szydagis, N Barry, K Kazkaz, J Mock, D Stolp, M Sweany, M Tripathi, S Uvarov, N Walsh, and M Woods. NEST: a comprehensive model for scintillation yield in liquid xenon. *Journal of Instrumentation*, 6(10):P10002–P10002, oct 2011. doi: 10.1088/1748-0221/6/10/p10002.

[55] A. Izenman. Review papers: Recent developments in nonparametric density estimation. 86:205–224, 03 1991.

[56] A. Ferrari, P. R. Sala, A. Fasso, and Johannes Ranft. FLUKA: A multi-particle transport code (Program version 2005). 2005.

[57] John A Nelder and Roger Mead. A simplex method for function minimization. *The computer journal*, 7(4):308–313, 1965.

[58] William Templeton Eadie, Daniel Drijard, and Frederick E James. Statistical methods in experimental physics. *smep*, 1971.